Study on Development of Cobalt Oxide-Based Redox System for Thermochemical Energy Storage

Department of Chemical Systems Engineering,
Graduate School of Engineering, Nagoya University

Rongjun WU

Contents

Chapter 1. Introduction

This thesis focuses on the experimental investigation of cobalt oxide-based redox systems for thermochemical energy storage. The research includes the development of efficient cobalt oxide-based materials for use in energy storage and the exploration of porous cobalt oxide for application in reactor concepts. The effects of CuO doping on the redox behavior and repeatability performance of cobalt oxide were studied. A feasible method to enhance the repeatability performance of Cu-doped cobalt oxide materials was developed. $LiCoO_2$-doped cobalt oxide composites were initially proposed and investigated for thermochemical energy storage applications. The redox behavior and repeatability performance of the $LiCoO_2$-doped cobalt oxide composite and its redox process were investigated. Finally, valuable insights into cobalt oxide foams for use in efficient and reliable thermochemical energy storage systems were provided. Cobalt oxide foams were fabricated by a foam replica method using inexpensive polyurethane (PU) foams as the templates. The effects of various preparation conditions on the foam-like structure and redox performant of cobalt oxide were analyzed. The structural evolutions of cobalt oxide foams after undergoing several reduction-oxidation cycles were observed. A consecutive immersion approach was introduced to enhance the structure and increase the bulk density of the cobalt oxide foam.

In the following sections of this chapter, background information regarding energy and environmental issues, as well as thermal energy storage is briefly introduced. The motivations of study on cobalt oxide-based redox system for thermochemical energy storage are then summarized. Finally, the objectives of the study and the outline of this thesis are presented.

1.1 Background

1.1.1 Global energy situation and development trends

Global energy consumption has continued to increase at an accelerating rate since the industrial revolution, as the industrialization and urbanization around the world have progressed rapidly. Figure 1-1 shows global primary energy consumption by fuel. The global energy consumption has been increasing at an average rate of around 1.9% per year over the past two decades. Fossil fuels have always played a dominant role in the

world's energy mix due to their relatively low cost, high energy density, and established infrastructure for extraction, transportation, and distribution. According to data from the BP Statistical Review of World Energy (June 2022), the fossil fuels including oil, natural gas, and coal accounted for around 80% of the total consumption in the world in 2021.

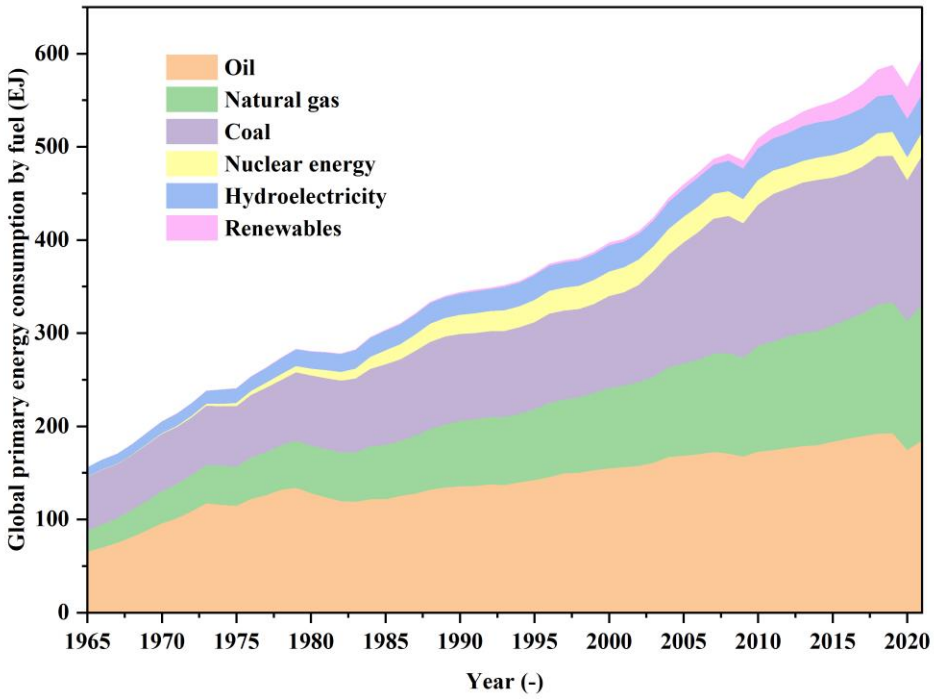

Figure 1-1. Global primary energy consumption by fuel (sourced from the BP Statistical Review of World Energy (June 2022)).

On the other hand, the combustion of fossil fuels can release large amounts of greenhouse gases, such as carbon dioxide (CO_2), and other air pollutants, such as sulfur dioxide and nitrogen oxides [2]. Thus, the significant consumption of fossil fuels has led to various environmental issues like air and water pollution, climate change, and environmental degradation. Figure 1-2 shows global CO_2 emissions from energy use, it can be observed that the CO_2 emissions dramatically increased over years. There was a decrease in global CO_2 emissions from energy use in 2020 due to the reduced economic activity and travel restrictions caused by the COVID-19 pandemic, which led to a drop in global primary energy consumption in 2020, as shown in Figure1-1. However, the CO_2 emission from energy use rebounded in 2021 and reached approximately the same level as 2019. The main reason is the recovery of the global economy and the subsequent increase in energy

demand.

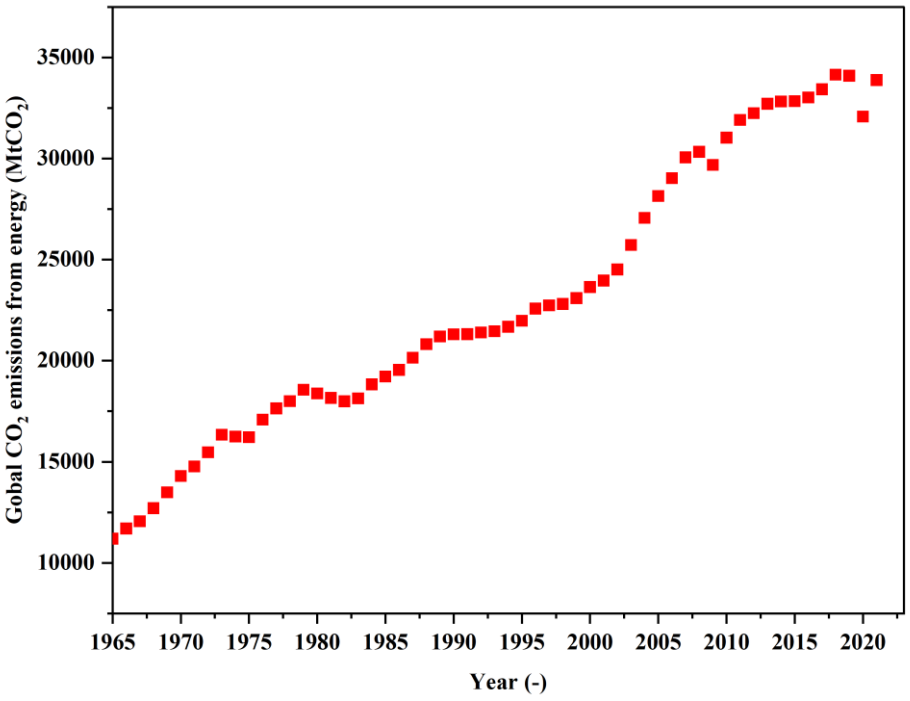

Figure 1-2. Global CO_2 emissions from energy use (sourced from the BP Statistical Review of World Energy (June 2022)).

To reduce the reliance on fossil fuels and mitigate these environmental issues, there is a growing global consensus on the need to transition towards a more sustainable and low-carbon energy system. The concept of sustainable development has been widely accepted as a guiding principle for human production and development. As more and more countries, companies, and organizations have become increasingly aware of the urgency of addressing climate change, the idea of achieving carbon net zero, which refers to the concept of achieving a balance between the amount of carbon emissions produced and the amount of carbon removed from the atmosphere, has gained significant momentum in recent years. All of these agreements require a range of measures, including improving energy efficiency, the share of renewable energy in the energy mix, and the development of new technologies to capture and store carbon. There is an increasing progress in the transition to renewable energy. As shown in Figure 1-3, global renewable primary energy consumption increased over the years. Additionally, solar and wind power showed an evident growth over the last decade, sharing approximately 24.4% and 43.9% in the

renewable primary consumption excluding hydroelectricity in 2021.

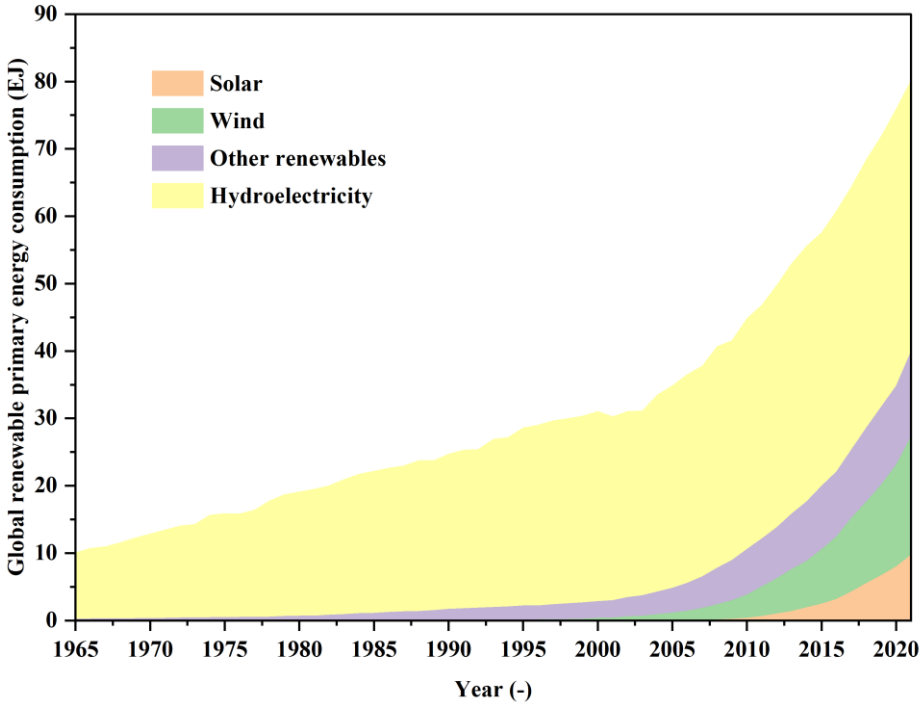

Figure 1-3. Global renewable primary energy consumption (sourced from the BP Statistical Review of World Energy (June 2022)).

According to data from the BP Statistical Review of World Energy (June 2022), the renewable primary energy consumption accounted for around 13.5% of global primary energy consumption in 2021. While progress has been made, there is still significant room for improvement. Low-carbon technologies with a wide range of solutions, such as energy storage system, electric vehicles, carbon capture and storage, play vital role on transforming the global energy system.

1.1.2 Thermal energy storage technology

Thermal energy storage (TES) technology is a technology that allows thermal energy to be stored and released when needed. TES technology plays a vital role in creating a more sustainable and efficient energy system. This technology is beneficial for improving energy efficiency in buildings, industrial processes, and power plants by storing excess thermal energy. Also, this technology can be employed in renewable utilizations, such as storing solar thermal energy and geothermal energy. For instance, TES technology has

been integrated into some solar power plants to store solar thermal energy during the day or when the demand is low. The stored energy can be used to generate electricity during the periods of low sunlight or at night or during the periods of high demand. By this way, solar power plants with TES systems can provide a more consistent and reliable source of electricity, even the sun is not shining [3-5]. There are several types of TES systems, and they can generally be classified into three categories based on the type of thermal energy form: sensible heat storage, latent heat storage, and thermochemical energy storage systems.

1.1.2.1 Sensible heat storage

Sensible heat storage is a type of TES system in which thermal energy can be stored and released by changing the temperature of a storage medium, without changing its phase. The storage amount of the thermal energy can be calculated by the following equation:

$$Q = m \times C_p \times \Delta T \quad (1\text{-}1)$$

where Q is the stored thermal energy, m is the weight of the storage medium, C_p is the specific heat capacity of the material and ΔT is the temperature change. In this regard, a suitable storage medium used in a sensible heat storage system should has a high specific heat capacity, which means that it can store a large amount of thermal energy in a certain temperature change [6].

A variety of materials (commonly are liquid and solid phases), including water, oils, molten salt, rocks, and concrete are available for sensible heat storage systems. Water is a common choice due to its high specific heat capacity (4.18 J/g·°C), availability and relatively inexpensiveness, while its working temperature is limited to below 100 °C, which means that it may not be suitable for high-working temperature applications [7, 8]. Oils and molten salts have higher working temperatures than water, making them suitable for moderate and high-temperature applications. Normally, oils (including mineral, synthetic, silicone, and several vegetable oils) can be used in sensible heat storage at a temperature below 400 °C [9-12]. Molten salt is another commonly used material for sensible heat storage systems, particularly for applications at a very high working temperature up to 600 °C. Typically, molten salt is made by melting a mixture of different salts, such as mixture of different nitrates, mixture of different chlorides [13-19]. Several types of molten salts, such as $NaNO_3$-KNO_3 (commonly known as Solar salt) [20], have been commercially used in concentrated solar power (CSP) plants. Such as the Andasol

Solar Power Station and the Gemasolar solar thermal power plant in Spain, and the Noor Complex Solar Power Plant in Morocco. Generally, a CSP plant mainly consists of solar power receivers, which collects solar power by using mirrors or lenses to focus sunlight, thermal storage systems used to store the solar thermal energy for later use, heat exchangers, in which the working fluid (typically water) can be heated to generate steam, steam turbines, generators [21].

Rocks and concrete are also commonly used as mediums for solar thermal power plants. In this configuration, rocks and concrete filled in a thermal energy storage tank are heated by circulated hot fluid, usually a heat transfer fluid such as molten salts [22-24]. Compared to molten salt, one advantage of using rocks and concrete for sensible heat storage systems is their durability. Rocks and concrete can withstand high temperatures and do not degrade over time, which allows them to store heat for extended periods of time. In contrast, molten salt may corrode equipment and lose its effectiveness over time. While rocks and concrete have lower thermal conductivity, which can limit the charging and discharging rates.

In summary, sensible heat storage has become a mature technology using in solar thermal power plants commercially for several decades. Generally, it offers the advantage of low cost and simplicity. However, there are also some limitations and challenges associated with sensible heat storage. Sensible heat storage system usually has a low energy storage density, which requires a large storage volume. Also, sensible heat storage system is typically limited to temperatures below 600 °C, which limit its applications in higher working temperatures. In addition, the system should be well-insulated to prevent heat losses.

1.1.2.2 Latent heat storage

Latent heat storage is a type of TES system in which thermal energy can be stored and released by changing the phase of a storage medium such as melting and solidification, without any change in temperature. The storage amount of the thermal energy can be calculated by the following equation:

$$Q = m \times \Delta h \quad (1\text{-}2)$$

where Q is the stored thermal energy, m is the weight of the storage medium, Δh is the enthalpy change during the phase change. In this regard, a suitable storage medium used in a latent heat storage system should has a high enthalpy change during the phase change,

which means that it can store a large amount of thermal energy by changing phase [25, 26].

The storage medium used in latent heat storage systems usually are called as phase change materials (PCMs). Theoretically, PCMs can be classified into different categories based on phase changing forms, such as solid-gas, liquid-gas, solid-liquid, and solid-solid PCMs. However, the phase changing process between a gas and a liquid or solid phase will experience a significant change in volume, which can impact the design and operation of the latent heat storage systems [27, 28]. Solid-solid PCMs generally have a relatively small enthalpy change during the phase change compared to other types of PCMs. Additionally, solid-solid PCMs may exhibit plastic crystal phenomena which can lead to variations in the phase changing temperatures, making it difficult to control the performances of PCMs. Despite these limitations, solid-solid PCMs still show the potential applications in a variety of fields. For instance, they can be used as thermal energy storage mediums in buildings to regulate indoor temperatures and reduce energy consumption. Several researches focused on solid-solid PCMs were proceeded to improve their enthalpies and stabilities [29].

Solid-liquid PCMs are the most commonly studied and used for latent heat storage applications due to their relatively high enthalpy changes during the phase change and small changes in volume during phase changes compared to other types of PCMs. Several organic materials including paraffin waxes, esters, fatty acids are commonly studied and used for latent heat storage systems in working temperatures below 260 °C due to their low melting points and relatively low cost [27, 30-32]. Many inorganic materials including salts [33-38], metals [39], and alloys [40] are also popular choices for latent heat storage systems in a wide range of temperatures (from 100 to 1000 °C or higher).

Latent heat storage systems using molten salts have been widely studied and implemented in concentrated solar power plants, in conjunction with sensible heat storage systems [35, 36, 41]. These systems operate by melting and solidifying the salts, taking advantage of their relatively high energy storage density compared to sensible heat storage. The ability of the latent heat storage system to store large amounts of thermal energy with a minimal temperature change allows it to maintain a relatively constant temperature when absorbing or releasing thermal energy. As a result, it possible to store thermal energy over longer periods of time without significant losses or degradation. Additionally, latent heat

storage systems are widely used in other applications such as ice storage air conditioning, building application, refrigeration [25].

To date, latent heat storage systems have been studied in depth by researchers and have shown promising progress in commercialization. The ongoing research and development of the latent heat storage system is focused on developing new PCMs and improving the performance and efficiency of PCMs for latent heat storage applications [26]. Some PCMs can degrade over time or undergo chemical changes that can affect their thermal properties, such as hydrated salts, which can undergo phase separation and may corrode the metal container [42].

1.1.2.3 Thermochemical energy storage

Thermochemical energy storage (TCS) is a type of thermal energy storage system in which thermal energy can be stored and released by reversible chemical reactions. During the charging process, thermal energy is absorbed by a material, which triggers a chemical reaction that converts the material into a high-energy state. The material with a high-energy state can be maintained for long periods of time at ambient temperature until the energy is needed. During the discharging process, the stored thermal energy will be released by triggering the reversing chemical reaction of the material.

TCS has several prominent advantages over other types of thermal energy storage systems. It can provide high energy storage density. Meanwhile, due to its ability to store energy in a chemical form, it is possible to store thermal energy in a long-term storage period and transport the stored thermal energy over long distances. Additionally, TCS systems can be flexibly operated at a wide range of temperatures based on a series of chemical reactions [43-45]. There are several types of thermochemical energy storage systems based on different chemical reactions and materials, which can have different properties and performance characteristics. General criteria for selecting suitable materials for thermochemical energy storage were proposed [45, 46]: (1) Large reaction enthalpy to maximize energy storage capacity and minimize storage volume. (2) Stable repeatability for long periods of time. (3) Fast reaction rates. (4) Low degradation of the reactants in both storage and reaction periods. (5) low toxicity and environmental impact, low cost and abundance of the materials. Overall, the selection of suitable materials for TCS systems depends on a balance of these criteria. The main types of TCS systems include:

Hydration/dehydration system in which a hydroxide material or a salt hydrate material

is dehydrated by an endothermic process to produce a metal oxide or a salt and water vapor and then the metal oxide or salt can be rehydrated to release the stored thermal energy when it is needed. The partial pressure of water vapor and the temperature of the system are key factors that affect the hydration and dehydration processes. These factors determine the amount of water that can be absorbed during the hydration process and released during the dehydration process [47-49]. This system can provide high energy storage density (exceed 1000 kJ/kg) and is typically used for low-moderate temperature TCS applications [45, 50]. The most studied materials for this system include $CaCl_2/CaCl_2{\cdot}nH_2O$ [49, 51, 52], $LiOH/LiOH{\cdot}H_2O$ [53, 54], $CaO/Ca(OH)_2$ [55, 56] and $MgO/Mg(OH)_2$ [57, 58]. Generally, the salt hydrate systems are worked at relatively low temperatures (below 200 °C) than the hydroxide systems, which can be operated at higher temperatures (e.g., $CaO/Ca(OH)_2$ can be worked at 400-750 °C [45, 55, 56]).

Carbonation/decarbonation system, also known as a carbonate looping system, in which a metal carbonate is heated to a high temperature to release CO_2 and produce a metal oxide. This reaction absorbs thermal energy, which is stored in the metal oxide. When the stored thermal energy is needed, the metal oxide then can be re-carbonated with CO_2 to release the stored thermal energy. The efficiency of this system is highly dependent on the partial pressure of CO_2 and the temperature of the system [59-61]. By controlling the temperature and pressure conditions, the reactions can be reversed to store or release thermal energy as needed. This system can also provide high energy storage density (exceed 1000 kJ/kg) and is typically used for high-temperature TCS applications [45, 59]. The most commonly studied carbonation/decarbonation systems include $MgO/MgCO_3$ system in which the working temperature is typically in the range of 400-600 °C [62, 63], $CaO/CaCO_3$ system in which the working temperature can range from 600 to 1000 °C [62, 64-66], and $SrO/SrCO_3$ system that operates at a temperature over 1000 °C, typically in the range of 1000-1200 °C [62, 67-69].

Metal hydride synthesis/dehydrogenation system in which a metal hydride is dehydrogenated to produce a solid metal and gaseous hydrogen during an endothermic process and then the metal hydride can be re-formed by the metal and hydrogen to release the stored thermal energy when it is needed. Similarly, this system is significantly affected by the temperature and the pressure. In general, in order to absorb and release hydrogen gas, high temperatures and pressures are required to achieve optimal absorption and

desorption rates [70-72]. However, the high pressure also affects the safety of the system. In view of this, higher standards to prevent leakage of the system is needed. This system has an outstanding energy storage density which can exceed 2000 kJ/kg, and it has a wide working temperature range, typically ranging from around 250 to over 1000 °C [45, 73, 74]. Magnesium, titanium, calcium, as well as many alloys have shown potential for use in metal hydride-based systems for thermal energy storage [73, 74].

Reduction/oxidation system, also named as metal oxide-based redox TCS system, in which a metal oxide is reduced in an endothermic process along with the release of oxygen and then the reduced metal oxide can be re-oxidized with oxygen to release the stored thermal energy. In this system, air can be used as oxygen source as well as heat transfer medium. That is to say, this system can be theoretically performed in an open-loop system in which there are no technical requirements for gas storage units. This fact is different from other types of TCS systems mentioned above, in which the gas storage units are basically required such as water vapor storage in hydration/dehydration systems, CO_2 storage in carbonation/decarbonation systems, and hydrogen storage in metal hydride-based systems. This system is commonly proposed for high-temperature TCS applications [45, 75, 76]. The most studied conventional metal oxide-based systems include BaO/Ba_2O [77, 78], Mn_2O_3/Mn_3O_4 [79], Co_3O_4/CoO [80], and CuO/Cu_2O [81], in which the working temperatures range from around 700 to 1200 °C. Additionally, novel materials like perovskite oxides [82-84] and many multi-metal oxides like iron-doped manganese oxides [85], lithium-manganese oxides [86, 87], copper-manganese oxides [87] were also proposed as promising candidates for redox-based TCS applications. This system can generally achieve a relatively high energy storage density, varying in the range of around 200-900 kJ/kg [76].

In addition, several organic systems, such as synthesis/decomposition of ammonia [88, 89] and methane reforming [90, 91] were also proposed as potential candidates for TCS applications. In the synthesis/decomposition of ammonia, ammonia is synthesized from nitrogen and hydrogen along with an endothermic process and then the ammonia can be decomposed to release the stored thermal energy and produce nitrogen and hydrogen. In the case of methane reforming system, the excess heat source is absorbed to convert methane into hydrogen and carbon monoxide and then the hydrogen and carbon monoxide can be used for a variety of purposes, including power generation and fuel

production.

Overall, TCS has the potential to store and release energy with high efficiency, making it a promising option for large-scale renewable energy systems and waste heat recovery systems. However, TCS technology is still in the early stage of development. Compared to sensible heat storage and latent heat storage technologies, it is more complex and requires additional components such as reactors and heat exchangers and needs careful control and management of the reactants and products. In addition, TCS systems require relatively higher demands of operating equipment owing to the higher working temperatures. Despite these challenges, TCS technology continues to be an active area of research and development. Most of the research in this area is still at the lab-scale. Ongoing research is focused on improving the efficiency and durability of the existing TCS materials and systems, as well as developing new materials for use in TCS.

1.2 Motivation

Thermochemical energy storage is playing a vital role on renewable energy utilization and improving the energy efficiency. In recent years, metal oxide-based redox TCS system, which is based on reduction and oxidation of metal oxides, has attracted increasing attention as a means of storing and utilizing thermal energy, particularly in concentrated solar power plants due to its high working temperature and convenient operation with air. In a typical process, high temperature air heated by solar radiation is used to trigger the reduction of metal oxides, simultaneously partial thermal energy can be stored in the reduced metal oxides. In the off-sun period, the thermal energy can be released by oxidizing the metal oxides with air. Air is utilized as oxygen source and heat transfer fluid.

The metal oxide-based redox TCS system is at an early stage of development. To date, the development of suitable metal oxide-based TCS materials is an active area of research, with a focus on improving the performance, stability, and scalability of these materials for practical applications [77-87]. At the same time, gram-scale [92, 93] and kilogram-scale [94, 95] experiments for the systems are growing faster with the advances on materials, including designing efficient reactors, scaling up TCS systems, and optimizing the operating conditions, as well as exploring ways to integrate the systems with some renewable energy sources. Several metal oxides have shown the potential for use in TCS

applications. However, there are many challenges existed, such as BaO in BaO_2/BaO system can easily react with CO_2 and moisture in air, which needs higher technical requirements for use in applications; Mn_2O_3/Mn_3O_4 exhibits a low re-oxidation kinetics, which affects the efficiency and repeatability; CuO/Cu_2O reacts at a high temperature that close to the melting point of Cu_2O, which may affect the stability [45, 87]. Improving the efficiency and durability of existing systems and developing new materials are crucial for using metal oxide-based redox systems in TCS applications.

Cobalt oxide (i.e. Co_3O_4/CoO) was considered as the most attractive candidate for metal oxide-based TCS application owing to its remarkable reaction repeatability and high energy storage density (844 kJ/kg) [76, 80, 96]. The relevant redox reaction equation is shown below:

$$2Co_3O_4(s) \rightleftharpoons 6CoO(s) + O_2(g) \quad (1\text{-}3)$$

where the right side in equation (1-3), Co_3O_4 reduction, is an endothermic step corresponding to thermal energy storage, and the left side, CoO oxidation, is an exothermic step corresponding to thermal energy release.

Significant research and efforts have been involved in the development of cobalt oxide-based redox TCS systems. The high reaction temperature of cobalt oxide, especially the reduction temperature is over 900 °C, limits the possible applications not only in concentrated solar power plants but also in other areas such as industrial waste heat recovery. According to data from a report on an actual waste heat survey in the industrial sector in Japan [97], the electric power industry, steel industry, and chemical industry in Japan emit the highest amounts of exhaust gas heat, constituting 35%, 14%, and 14% of the total domestic exhaust heat, respectively. As shown in Figure 1-4, in the steel industry, exhaust gas heat released at temperature over 500 °C accounts for 17%, highlighting a particularly promising area for waste heat recovery. Doping with foreign metal components (e.g., Fe, Mn, Ni, Cu, Zn, and Mg) have been proved to be an alternative method to change the chemical parameters as well as the operating temperatures of the cobalt oxide-based systems [80, 98-102]. For instance, appropriate amount of Fe was found to be beneficial for the microstructural stability [98]. Ni-doping [102] and Cu-doping [80, 100] can decrease the working temperatures, which make it possible to use cobalt oxide-based TCS systems at relatively low temperatures. This doping approach opens up more possibilities for the use of cobalt oxide-based TCS systems.

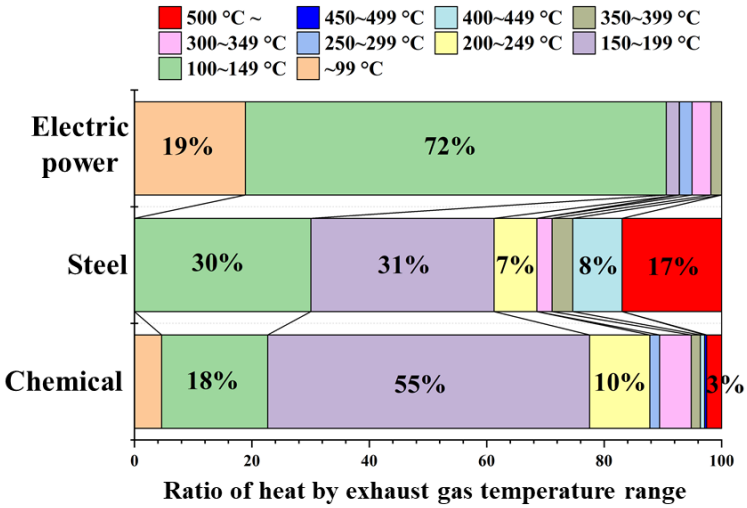

Figure 1-4. Temperature distribution of exhaust gas heat for three industries in Japan (Estimated value) [97].

Meanwhile, it should be pointed out that metal oxides in TCS systems commonly undergo sintering behaviors during redox cycling due to the high working temperature ranges, which are close to their melting temperatures or their Tammann temperatures [103]. In this way, morphologies of metal oxides may be affected by the sintering, ultimately impacting the oxygen diffusion during the re-oxidation process [76]. Block et al. [100] reported that the cobalt-rich cobalt oxide/copper oxide compositions with $0.1 \leq y \leq 0.33$ (y was the molar ratio of Cu/(Cu+Co)) showed fast kinetics. While Agrafiotis et al. [80] proposed that $CuCo_2O_4$ in which the molar ratio of Cu/(Cu+Co) was 0.33 showed a slow re-oxidation rate in the first cycle. The different repeatability behaviors of Cu-doped cobalt oxide systems in literatures appeared to need a deeper investigation, particularly regarding their sintering behaviors.

Additionally, as reported in literatures, a sol-gel method is a commonly used approach for preparing multi-metal oxides [83-85, 87, 98, 100-102]. However, when it comes to scalability and practical applications, more suitable preparation methods are needed.

At the same time, due to its excellent performance, there is a growing progress in the scale-up investigation of cobalt oxide. Significantly, cobalt oxide system has been tested at pilot-plant scale (90 kg) in Solar Tower Julich (Germany) [94]. However, with the increasing amount of metal oxide powders used in the reaction and the increasing size of the reactor in which the reaction takes place, several issues regarding the efficiency and stability of metal oxide-based TCS systems may occur, especially when the reactor is a

packed bed reactor which is commonly used, simple and able to store a large amount of materials. The dense packing of metal oxide particles limits heat transfer between the particles and the heating medium (i.e., air) as well as limits efficient contact between the particles and oxygen, resulting in slow reaction rates and low conversion ratios [104]. Accordingly, metal oxides with foam-likes structures were proposed for use in TCS systems [105, 106]. However, the lack of the insight into the structural stability and preparation enhancement of the metal oxide foams limits their utilization in TCS. Further investigation concerning the detail of the structural stability and durability of metal oxide foams for TCS applications is needed.

1.3 Objective

The focus of this research is summarized in the following key objectives:

(1) To deep understand the behavior of Cu-doped cobalt oxide-based redox system for TCS and improve its repeatability performance, CuO-doped cobalt oxide composites were proposed and investigated. The effects of CuO doping on the redox behavior and repeatability performance of cobalt oxide were explored.

(2) To develop suitable materials for TCS applications and increase more applicability of cobalt oxide-based TCS systems, a Li-doping strategy was proposed to tune the chemical properties of cobalt oxide. The potential of $LiCoO_2$-doped cobalt oxide composites for use in TCS was studied.

(3) To effectively employ cobalt oxide-based materials for TCS applications, cobalt oxide foams were fabricated by a polyurethane (PU) foam replica method. Valuable insights into the preparation and utilization of cobalt oxide foams for TCS applications were provided. A consecutive immersion approach was introduced as a means to enhance the cobalt oxide foams.

1.4 Outline

This thesis includes five chapters. The background information and literature review relevant to cobalt oxide-based TCS, as well as the focus of this research are summarized in Chapter 1, as aforementioned.

Chapter 2 presents the details of the experimental study on the effects of CuO doping on the redox behavior and repeatability performance of cobalt oxide for use in TCS

applications. A mechanical mixing approach, which is conducive to scalability, was employed to prepare the CuO-doped cobalt oxide composites. The effects of the doping amount and particle size of CuO were highlighted. And then, a feasible approach to improve the repeatability performance of Cu-doped cobalt oxide materials was proposed.
Chapter 3 presents the details of the exploration on the potential of $LiCoO_2$-doped cobalt oxide composites for use in TCS applications. A mechanical mixing approach was also employed to prepare $LiCoO_2$-doped cobalt oxide composites. The redox behavior of the composites was experimentally investigated, especially the onset reaction temperatures and the reaction rates. The effect of $LiCoO_2$ doping amount on cobalt oxide was discussed. The reduction/re-oxidation process of the composite was studied and discussed. Additionally, the repeatability performance of the composite was tested.
In chapter 4, cobalt oxide foams were prepared by means of a foam replica method using inexpensive PU foams as the templates. The effects of several factors, including the solid loading of cobalt oxide slurry, sintering temperature, and sintering duration, on the preparation of cobalt oxide foams were explored and discussed. Valuable insights were also provided into the structural evolutions of cobalt oxide foams after several reduction-oxidation cycles. Additionally, a consecutive immersion approach was introduced to improve the structure and increase the bulk density of the cobalt oxide foam.
Chapter 5 presents major conclusions of this study and provides the suggestions for the future work in the metal oxide-based redox TCS systems.

Chapter 2. CuO-doped cobalt oxide composites for thermochemical energy storage

2.1 Introduction

Cu doping has been proved to be a promising method for lowering the operating temperature of cobalt oxide-based redox thermochemical energy storage (TCS) systems. However, more investigation regarding the effect of Cu components on this system is needed. Specifically, as reported in literatures, the repeatability performance of Cu-doped cobalt oxide system required a deeper investigation. From the work of Block et al. [100], the cobalt-rich cobalt oxide/copper oxide compositions with $0.1 \leq y \leq 0.33$ (y was the molar ratio of Cu/(Cu+Co)) showed fast kinetics. While Agrafiotis et al. [80] proposed that $CuCo_2O_4$ in which the molar ratio of Cu/(Cu+Co) was 0.33 showed a very slow re-oxidation rate in the first cycle. It has been found that the morphological changes of metal oxides might affect the oxygen mass transfer in re-oxidation process [76]. Also, Carrillo et al. [79] have reported that the morphological change influenced the repeatability of Mn_2O_3/Mn_3O_4 pairs. They concluded that different sintering mechanisms, which depended on the particle size of the material in that work, induced different morphological evolutions. Hence, the investigation of the effect of morphological evolution on the repeatability performance of Cu-doped cobalt oxide is of great interest. Additionally, it should be pointed out that Cu components were commonly used as sintering aids to enhance densification of materials [107, 108], which might be related to the deterioration of repeatability performance of Cu-doped cobalt oxide materials.

In this study, we proposed a composite of CuO-doped cobalt oxide, prepared by mechanically mixing CuO and Co_3O_4 powders at room temperature, for use in TCS applications. An in-depth investigation on the effects of CuO doping on the redox behavior and repeatability performance of a cobalt oxide-based TCS system was conducted. Significantly, the effects of the doping amount and particle size of CuO were highlighted. It is worth noting that sol-gel method is commonly used to prepare multi-metal oxides, but it may not be a suitable approach for large-scale production. In contrast, the mechanical mixing method used in this study not only has the advantage of scalability but also provides the possibility of adjusting the particle size of CuO.

2.2 Experimental section

2.2.1 Materials preparation

2.2.1.1 Preparation of CuO powder

In view of the results reported in literatures, different particle sizes of metal oxides (e.g., Mn_2O_3 and ZrO_2) were prepared by precipitation method with different precursor concentrations [79, 109]. Precipitation method could also be utilized as a facile way to obtain CuO nanoparticles [110]. Thereby, precipitation method using different copper nitrate concentrations was employed in the present study to synthesize CuO powder with different particle sizes [110]. Precursor solutions of $Cu(NO_3)_2 \cdot 2H_2O$ (99.9%, Kanto Chemical CO., INC.) were prepared with deionized water. The concentrations of the copper nitrate solution were varied in the range between 0.025 and 0.5M. After stirring at room temperature for 30 min, 1M sodium hydroxide (97.0%, Kanto Chemical CO., INC.) was added drop-wise with constant stirring. The addition of sodium hydroxide was finished when the solution was in excess to a pH of 11 ± 1. The resulting precipitate was aged and stirred for 24 h. Then, the obtained precipitate was filtered and washed with deionized water seven times and dried at 80 °C overnight. Afterwards, the solid was calcined at 700 °C for 4 h with a heating rate of 2 °C/min. The obtained CuO samples prepared with copper nitrate concentration of 0.025M, 0.05M, 0.1M and 0.5M were labeled as CuO (0.025M), CuO (0.05M), CuO (0.1M) and CuO (0.5M), respectively.

2.2.1.2 Preparation of CuO-doped cobalt oxide composites

Co_3O_4 powder (99.99%, Kanto Chemical CO., INC.) was used as received. Certain amount of Co_3O_4 and CuO powder were weighed and put in a mortar. To avoid the deviation generated in the milling process, the total weight of each sample was weighed in ~1000 mg. Materials were carefully mixed by hand, grinding with a speed of ~2 laps per second for 20 min. In the present work, composites doped with different CuO contents were prepared. The CuO content, *x*, is defined as,

$$x = \frac{m_{CuO}/\mathrm{M_{CuO}}}{m_{CuO}/\mathrm{M_{CuO}} + m_{Co3O4}/\mathrm{M_{Co3O4}}} \quad (2\text{-}1)$$

where m_{CuO} is the weight of CuO, $\mathrm{M_{CuO}}$ is the molar mass of CuO, m_{Co3O4} is the weight of Co_3O_4, and $\mathrm{M_{Co3O4}}$ is the molar mass of Co_3O_4.

2.2.2 Characterization

An X-ray diffraction (XRD; Rigaku Ultima IV) with Cu Kα radiation (40 kV/ 30 mA) was employed to identify the crystal phases of samples. The cell parameters of CoO phases of samples were derived from (111) (200) (220) facets, basing on Bragg's law.

To appreciate the morphologies of samples, a scanning electron microscope (SEM; JEOL JSM-7500FA) was exploited. ImageJ software was used in this study to obtain the particle size distributions of samples by statistical analysis of SEM image. More than 300 particles were analyzed for each sample.

To obtain the specific surface area (S_{BET}) values of CuO samples, a surface area and pore size distribution analyzer (BELSORP MAX II) with the multi-point BET method was utilized.

2.2.3 Redox investigation of materials

The reduction/re-oxidation process of sample was performed by a thermogravimetric analyzer (TGA; HITACHI STA7300), with each sample weight of around 10 mg. Typically, the temperature program for one reduction-oxidation cycle consisted of a heating step from 700 °C to 1000 °C with a dwell time of 5 min and a cooling step from 1000 °C to 700 °C with a dwell time of 5 min. Each sample was tested at a heating/cooling rate of 10 °C/min under an air atmosphere with a constant flow of 200 mL/min. During the reduction process, oxygen released, leading to a weight loss for the sample. During the re-oxidation process, oxygen uptake occurred, leading to a weight gain for the sample. The weight change, α (%), is defined as,

$$\alpha = \frac{m_i - m_t}{m_i} \times 100 \quad (2\text{-}2)$$

where m_i is the initial weight of sample, and m_t is the weight at time t. Due to the possible impurities existed in samples, initial weight of the second cycle was determined as the initial weight for each sample.

Moreover, the conversion ratio of reduction/re-oxidation, β, is defined as,

$$\beta = \left| \frac{m_0 - m_t}{m_i - m_f} \right| \quad (2\text{-}3)$$

where m_0 is the weight of sample at the beginning of the reduction/re-oxidation process, m_t is the weight at time t, and m_f is the final weight of sample after the reduction in the second cycle.

The charging-discharging heat values of samples during the reduction-oxidation processes were collected by a simultaneous TGA-DSC thermal analysis system (TGA/DSC; METTLER TOLEDO TGA/DSC 3+). Samples were tested under an air atmosphere with a constant flow of 100 mL/min. The temperature procedure for one reduction-oxidation cycle consisted of a heating step from 700 °C to 950 °C with following holding for 5 min and then a cooling step from 950 °C to 700 °C with following holding for 5 min. The heating and cooling steps were proceeded under the ramping rates of ±10 °C/min.

Additionally, an in-situ X-ray diffraction (in-situ XRD; Rigaku SmartLab 3 kW) with Cu Kα radiation (40 kV/ 40 mA) was operated to detect the structural transformations of samples during the reduction/re-oxidation steps. Samples were detected in a heating-cooling cycle between 30 °C and 950 °C under an air atmosphere.

2.3 Results and discussion

2.3.1 Characterization of materials

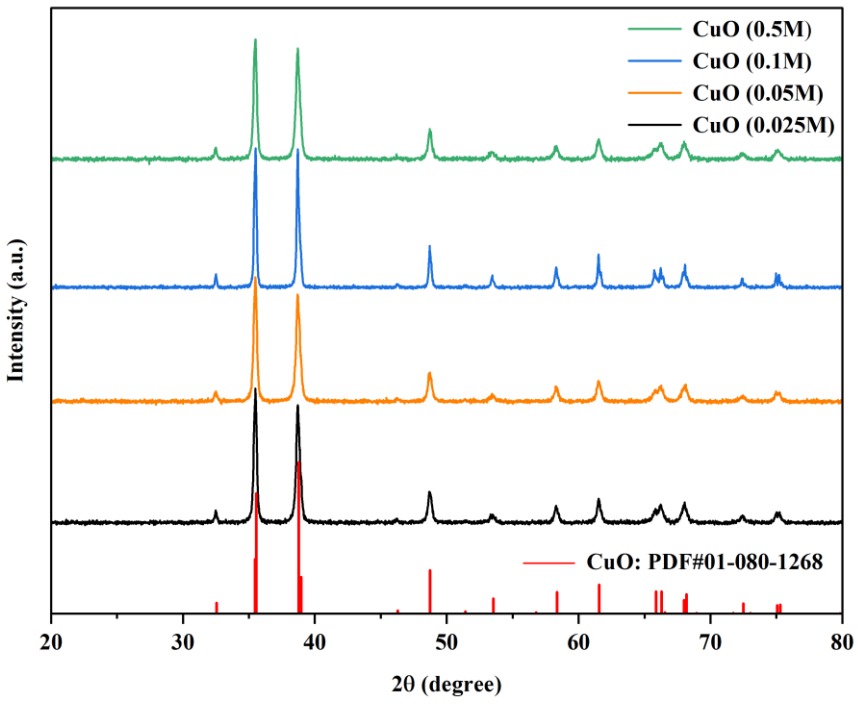

Figure 2-1. XRD patterns of CuO samples prepared with different copper nitrate concentrations.

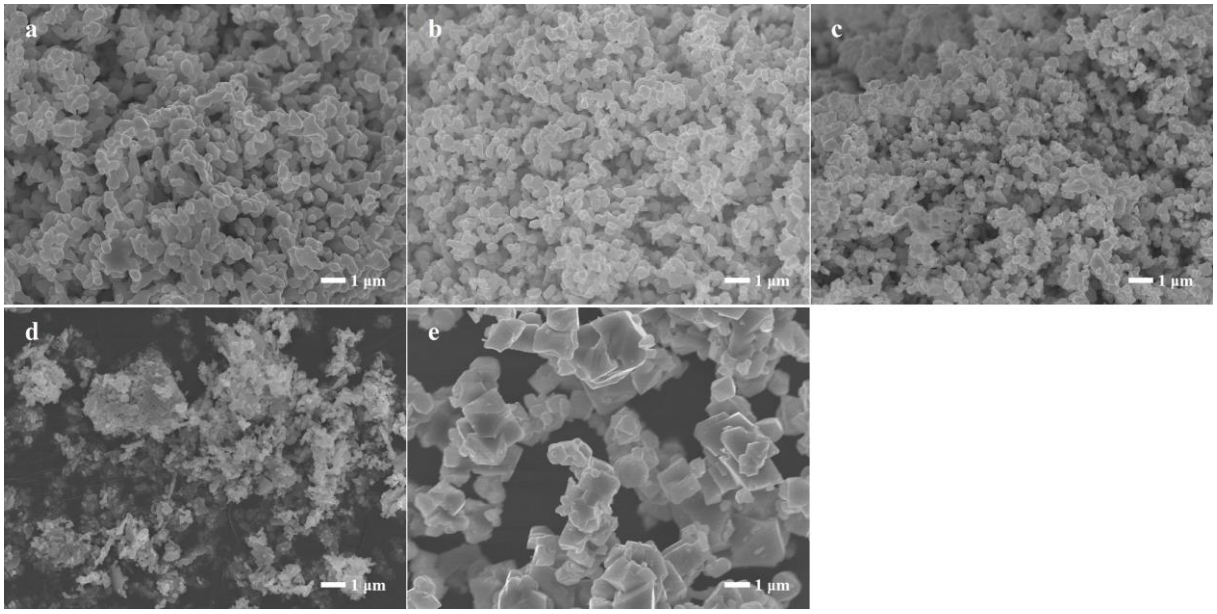

Figure 2-2. SEM images of samples: (a) CuO (0.5M), (b) CuO (0.1M), (c) CuO (0.05M), (d) CuO (0.025M), and (e) pure Co_3O_4.

The XRD result shown in Figure 2-1 illustrates that all the CuO samples prepared by precipitation method presented the characteristic reflections of CuO phase (PDF#01-080-1268). Figure 2-2(a-d) show the SEM images of the CuO samples prepared with different copper nitrate concentrations. As we can observe, all the CuO samples presented agglomerate morphologies which were formed by similar irregular shape particles. Meanwhile, it is possible to appreciate that the CuO samples prepared with different copper nitrate concentrations exhibited different particle sizes. The CuO sample prepared with a lower concentration presented a relatively small particle size. This fact can be observed more clearly by the particle size distributions shown in Figure 2-3. By lowering the copper nitrate concentration, the particle size distribution of the as-prepared CuO sample narrowed and shifted toward smaller diameter. Moreover, the S_{BET} values (Table 2-1) of the CuO samples increased from 2.01 m^2/g to 6.08 m^2/g when the copper nitrate concentrations decreased from 0.5M to 0.025M. In short, the results indicate that the concentration of copper nitrate solution affected the particle size of as-prepared CuO powder. In addition, the morphology and the particle size distribution of pure Co_3O_4 were displayed in the Figure 2-2e and Figure 2-3e, respectively. Pure Co_3O_4 also presented an

agglomerate morphology, which is the common characteristic of metal oxide powders. Moreover, pure Co_3O_4 exhibited a relatively large particle size distribution by comparing with the CuO samples.

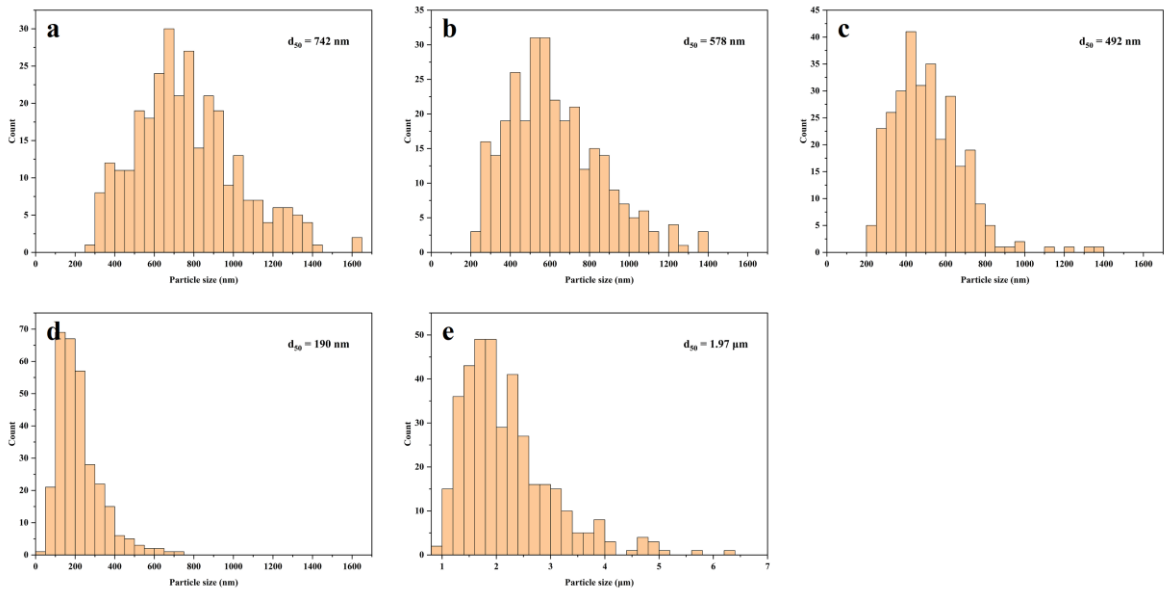

Figure 2-3. Particle size distribution histograms of samples: (a) CuO (0.5M), (b) CuO (0.1M), (c) CuO (0.05M), (d) CuO (0.025M) and (e) pure Co_3O_4.

Table 2-1 Specific surface area (S_{BET}) values of CuO samples prepared with different copper nitrate concentrations.

Sample name	Concentration (M)	S_{BET} (m^2/g)
CuO (0.5M)	0.5	2.01
CuO (0.1M)	0.1	2.58
CuO (0.05M)	0.05	2.71
CuO (0.025M)	0.025	6.08

Figure 2-4 displays the XRD patterns of pure Co_3O_4, pure CuO (0.5M), and CuO-doped cobalt oxide composites with different CuO (0.5M) contents (*x*). The result confirms that each composite exhibited Co_3O_4 phase (PDF#00-043-1003) and CuO phase (PDF#01-080-1268). Furthermore, the higher the CuO content doped in the composite was, the more intense the CuO diffractions presented.

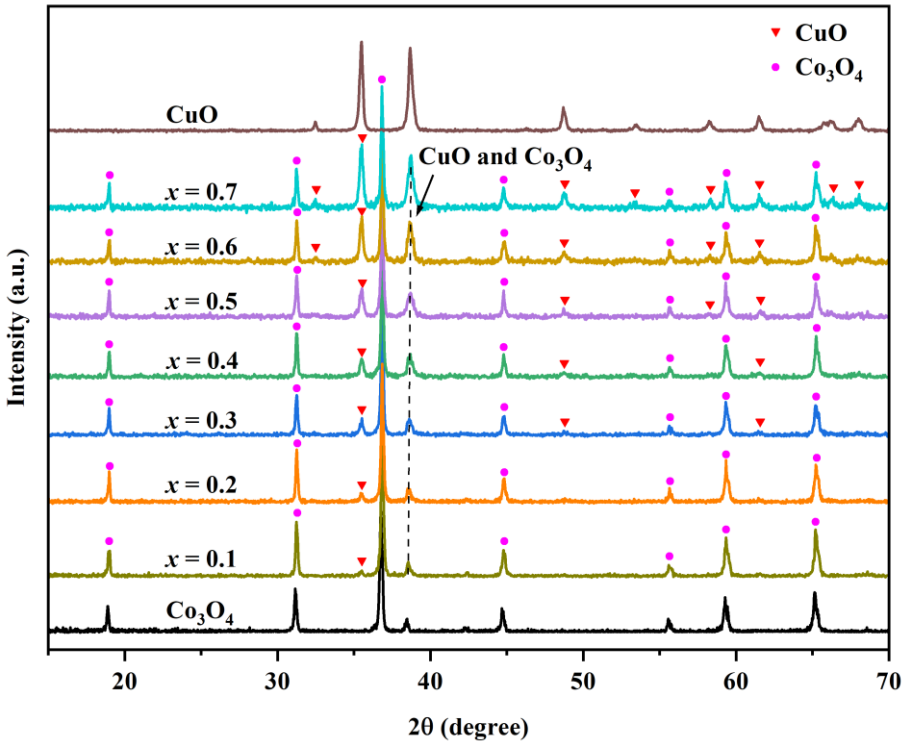

Figure 2-4. XRD patterns of pure Co_3O_4, pure CuO (0.5M) and composites doped with different CuO (0.5M) contents (*x*).

2.3.2 Redox behaviors of samples

The redox behaviors of samples were performed by TGA in two reduction-oxidation cycles between 700 °C and 1000 °C. CuO (0.5M) was used as the dopant to prepare the CuO-doped cobalt oxide composite. The effect of CuO doping on the redox behavior of cobalt oxide was explored. For comparison, pure Co_3O_4 and pure CuO (0.5M) were also tested under the same condition. As shown in Figure 2-5, there was a continuous weight loss in the first heating step for each sample, which may be attributed to two reasons: (1) the removal of some adsorbed compounds like water and CO_2 [79, 99]; (2) oxygen vacancies were generated in the crystal lattice of metal oxide at elevated temperature (with corresponding loss of oxygen), which caused by point defect [111, 112]. Afterwards, there was no sharp weight loss and weight gain occurred for pure CuO (0.5M) between 700 °C and 1000 °C. As described in the introduction, CuO/Cu_2O was also considered as a promising candidate for metal oxide-based TCS application. However, the onset reduction temperature of CuO to Cu_2O was higher than 1000 °C [81], which accounts for the result shown in Figure 2-5. Conversely, rapid weight loss in the heating step which

was attributed to the reduction process and rapid weight recovery in the subsequent cooling step which was attributed to the re-oxidation process can be observed for pure Co_3O_4 and the composites doped with CuO (0.5M). Additionally, with an increase in CuO (0.5M) content (x), there was a decrease in the weight change (Table 2-2). The reason is that the reactive component (i.e. cobalt oxide) content in the composite decreased as the CuO content increased, resulting in a decrease in the oxygen release/uptake amount during the reduction/oxidation process. It should be noted that this fact would affect the heat storage and release capacities of the composites [101]. The charging-discharging heat values during the reduction-oxidation processes for the samples were collected by DSC. As shown in Table 2-2, the charging/discharging heat decreased with the increasing content of CuO. Meanwhile, the discharging heat was lower than the corresponding charging heat, which might be due to the relatively slow re-oxidation rate as well as the heat loss caused by using the open alumina crucibles in DSC.

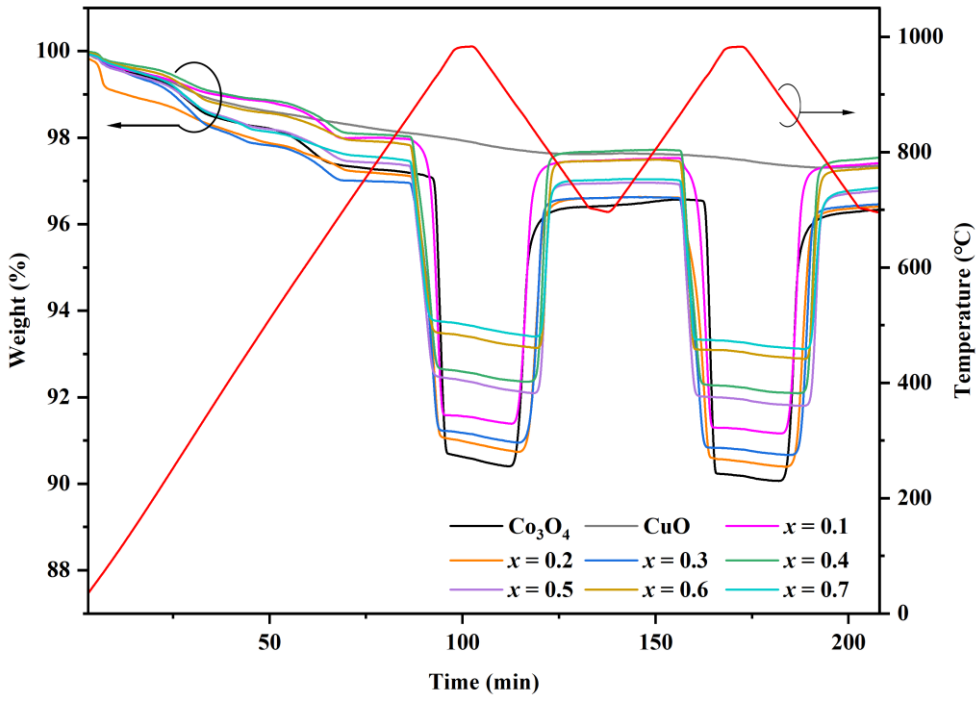

Figure 2-5. TGA curves of pure Co_3O_4, pure CuO (0.5M) and composites with different CuO (0.5M) contents (x).

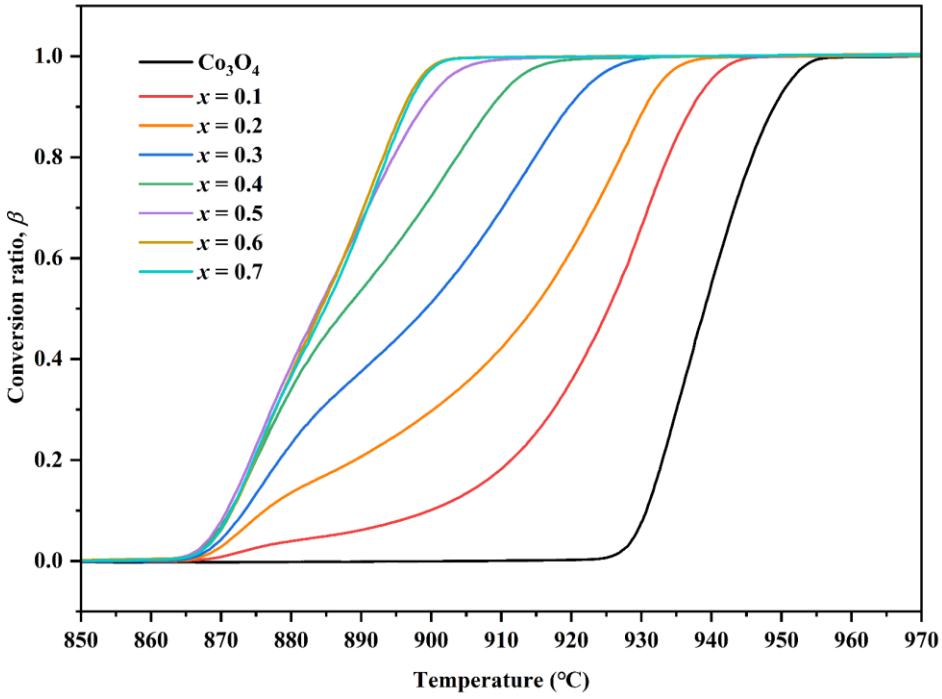

Figure 2-6. Evolutions of reduction conversion for Co_3O_4 and composites with different CuO (0.5M) contents (x).

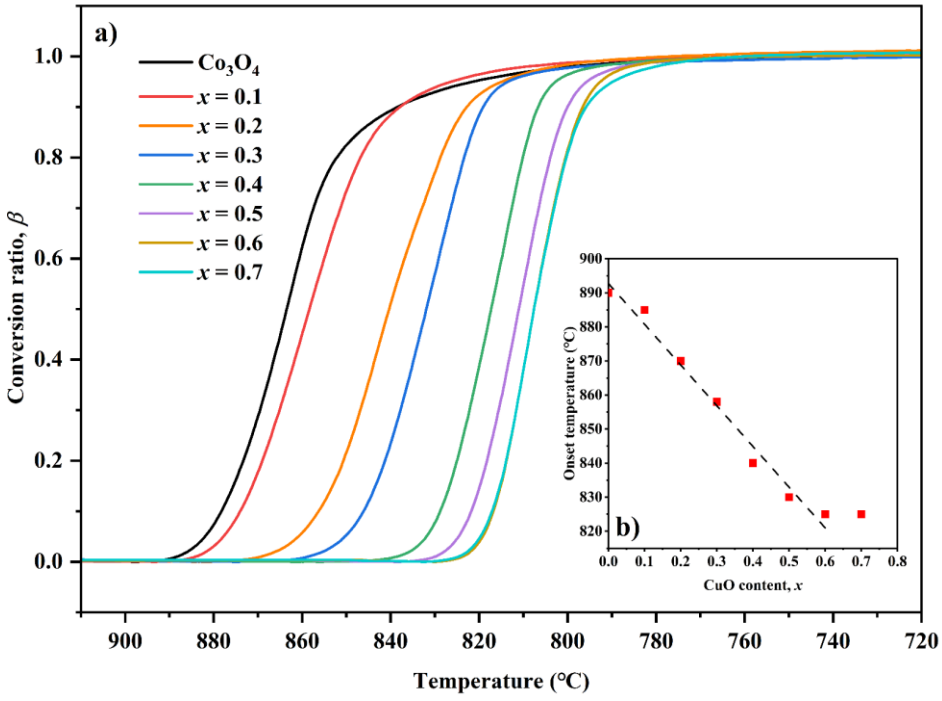

Figure 2-7. (a) Evolutions of re-oxidation conversion for cobalt oxide and composites

with different CuO (0.5M) contents (x) and (b) Evolution of the onset re-oxidation temperature as a function of CuO content (x).

Figure 2-6 displays the evolutions of reduction conversion in the second cycle for pure Co_3O_4 and the composites with different CuO (0.5M) contents (x). With the increasing of temperature, the conversion ratio of each sample increased. As we can see, doping with CuO shifted the onset reduction temperature from 925 °C for pure Co_3O_4 to 865 °C for the CuO-doped composites. All the composites exhibited the same onset reduction temperature while presented different reduction rates. As shown in Table 2-2, pure Co_3O_4 took ~3.3 min to complete the reduction, whereas the composite doped with CuO (0.5M) content of x = 0.1 finished the reduction in ~8.1 min. It can be observed that increasing the CuO (0.5M) content (x) from 0.1 to 0.6 improved the reduction rate gradually. Eventually, the curves for the composites doped with CuO (0.5M) content of $x \geq 0.6$ were nearly identical. It took ~3.4 min to obtain complete reduction.

Figure 2-7a describes the evolutions of re-oxidation conversion in the second cycle for pure cobalt oxide and the composites with different CuO (0.5M) contents (x). As shown in Figure 2-7a, doping with CuO lowered the re-oxidation temperature apparently. Furthermore, increasing CuO content linearly decreased the onset re-oxidation temperature from 890 °C for pure cobalt oxide to 825 °C for the composite doped with CuO (0.5M) content of x = 0.6 (Figure 2-7b). When the CuO (0.5M) content (x) exceeded 0.6, there was no significant shift for the onset temperature of re-oxidation. In addition, the composites doped with different CuO (0.5M) contents (x) exhibited an increase in the re-oxidation rate in the second cycle, as shown in Table 2-2. In a word, doping with CuO diminished the onset temperatures of reduction and re-oxidation of cobalt oxide. Moreover, it is possible to tune the onset re-oxidation temperature in the range from 825 °C to 890 °C by adjusting the CuO content in the composite.

2.3.3 Redox process exploration of CuO-doped cobalt oxide composites

To study the reduction/re-oxidation process of CuO-doped cobalt oxide composite, the structural transformation under a heating-cooling cycle for the composite doped with CuO (0.5M) content of x = 0.6 was detected by in-situ XRD. As shown in Figure 2-8A, the characteristic diffraction patterns of Co_3O_4 phase (PDF#00-043-1003) and CuO phase

(PDF#01-080-1268) can be observed for the composite at room temperature. As the temperature increased, there was a slight shift in the diffraction peaks toward smaller angle, which might be caused by the thermal expansion [113]. Meanwhile, the intensities of Co_3O_4 and CuO patterns decreased. Eventually, no Co_3O_4 phase and CuO phase were detected at 950 °C while a single phase of CoO (PDF#00-043-1004) presented, attributing to the reduction process. Afterwards, as shown in Figure 2-8B, Co_3O_4 phase and CuO phase reappeared while CoO phase disappeared as the temperature decreased to room temperature in the cooling step, attributing to the re-oxidation process. The result confirms the structural transformation of cobalt oxide during the reduction/re-oxidation process. Significantly, it was found that CuO was involved in the process. Cu species might dope into cobalt oxide structure during the reduction process and separate out during the re-oxidation process.

Moreover, Figure 2-9 displays the XRD patterns of reduced pure cobalt oxide and the composites with different CuO (0.5M) contents (x). These reduced samples were obtained by heating the samples to 1000 °C in air and then cooling the samples from 1000 °C to room temperature under a nitrogen atmosphere. The result confirms the presence of CoO (PDF#00-043-1004) in all the samples, which was produced by the reduction of Co_3O_4. It is worth noting that a secondary phase corresponding to CuO (PDF#01-080-1268) was detected for the composites with CuO (0.5M) content of $x \geq 0.6$. However, no CuO phase was detected for the composite with $x = 0.6$ at 950 °C (as shown in Figure 2-8). The cell parameters of these two CoO phases were calculated, basing on Bragg's law. The result shows that the cell parameter of CoO phase for the composite with $x = 0.6$ at 950 °C was 4.31 Å while the cell parameter of the CoO phase at room temperature was 4.26 Å. Thus, the expanded CoO crystal caused by thermal expansion at high temperature might allow more Cu species to dope into CoO crystal, leading to no CuO phase detected by XRD. In short, the result indicates that the doping amount of Cu species in CoO crystal was limited. This might explain the result illustrated in Figure 2-7 that the onset temperature of re-oxidation decreased gradually with the increasing amount of Cu species in CoO crystal. We presumed the Cu species doped in cobalt oxide was beneficial to decrease the temperature of redox process. However, a deeper investigation is necessary and needed in the future. Additionally, these XRD results were in accordance with the phase diagram of copper oxide/cobalt oxide in air [114], as shown in Figure 2-10. The CuO/Co_3O_4 binary

mixture can transform into a singer phase of CoO at a lower temperature, compared to pure Co_3O_4.

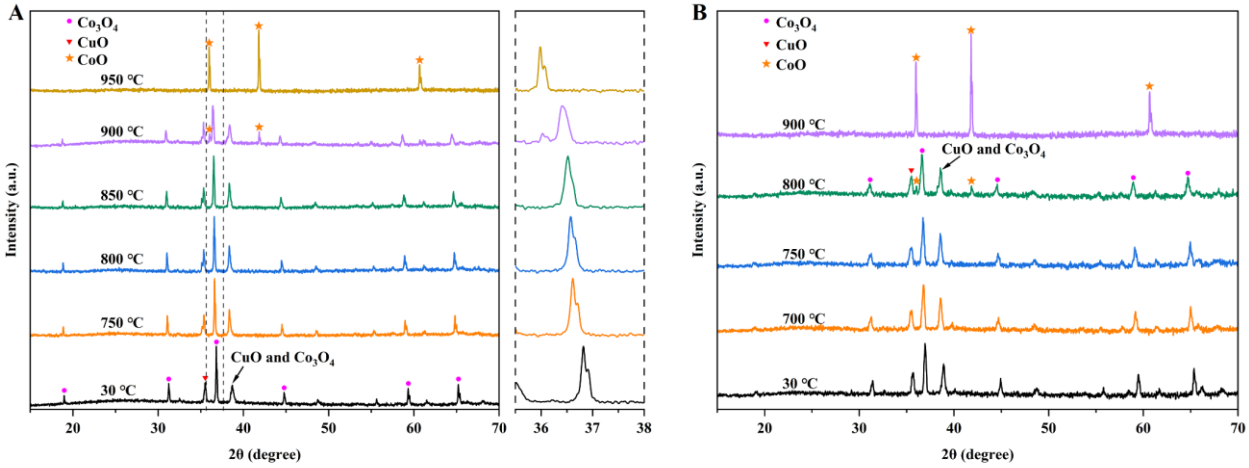

Figure 2-8. In-situ XRD patterns of composite with CuO (0.5M) content of x = 0.6: (A) In the heating step. The dashed-line zone was showed in the right panel. (B) In the cooling step.

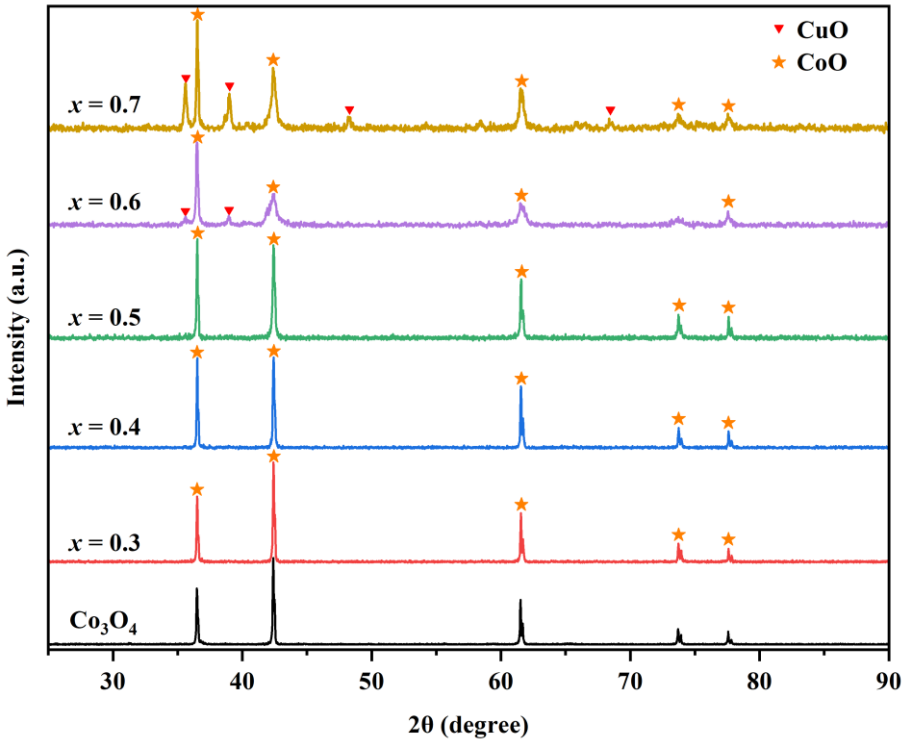

Figure 2-9. XRD patterns of reduced pure cobalt oxide and composites with different CuO (0.5M) contents (x).

Table 2-2 Onset temperature of reduction/re-oxidation, weight loss (α), reaction time and charging/discharging heat for pure cobalt oxide and composites doped with different CuO contents (x).

Sample	[a, b]$T_{onset\ red}$ (°C)	[a, b]$T_{onset\ oxi}$ (°C)	[a]Weight loss (%)	[a]Reduction time (min)	[a]Re-oxidation time (min)	[a]Charging heat (kJ/kg)	[a]Discharging heat (kJ/kg)
CuO (0.5M), x = 0	925	890	6.5	3.3	11.2	541	494
CuO (0.5M), x = 0.1	865	885	6.4	8.1	9.0	527	472
CuO (0.5M), x = 0.2	865	870	6.2	7.6	7.6	505	457
CuO (0.5M), x = 0.3	865	858	6.0	6.7	6.3	501	422
CuO (0.5M), x = 0.4	865	840	5.6	5.8	5.6	446	436
CuO (0.5M), x = 0.5	865	830	5.1	5.0	5.1	423	403
CuO (0.5M), x = 0.6	865	825	4.5	3.4	4.6	346	317
CuO (0.5M), x = 0.7	865	825	3.8	3.4	5.2	317	289
CuO (0.1M), x = 0.6	865	825	4.6	3.5	4.6	350	328
CuO (0.05M), x = 0.6	865	825	4.5	3.4	4.5	349	316
CuO (0.025M), x = 0.6	865	825	4.5	3.4	4.6	345	323

[a] The data was based on the second cycle.

[b] The onset temperature in this work corresponds to the start temperature of sharp weight change under the configured temperature program

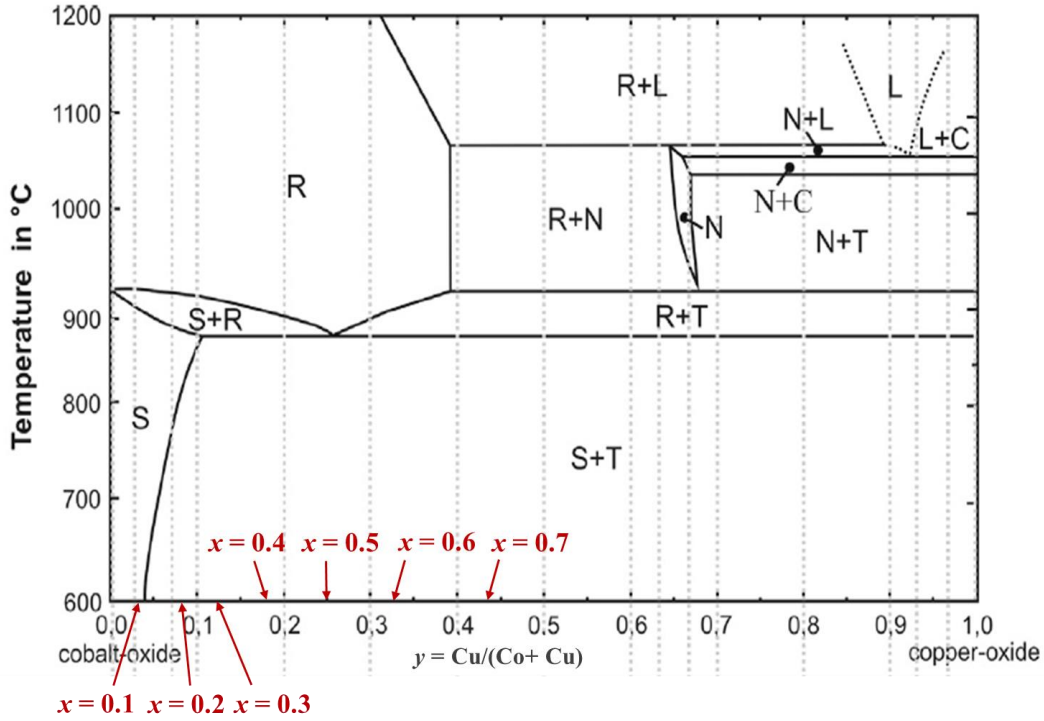

Figure 2-10. Phase diagram of copper oxide/cobalt oxide in air [100, 114].

(S: Cubic spinel phase (Co_3O_4), R: Cubic rock salt phase (CoO), T: Tenorite phase (CuO), C: Cuprite phase (Cu_2O), L: Liquid phase, N: New compound phase (Cu_2CoO_3)).

2.3.4 Repeatability performances of CuO-doped cobalt oxide composites

The repeatability and stability of energy storage materials are of particular importance for TCS applications. Hence, CuO (0.5M)-doped cobalt oxide composites and pure cobalt oxide were subjected to 30 reduction-oxidation cycles with a heating/cooling rate of 10 °C/min. Consistent with the results reported in literatures [76, 80, 96], pure cobalt oxide exhibited a stable repeatability behavior (Figure 2-11a and b). Figure 2-12 shows the TGA curves and the evolutions of re-oxidation conversion in 30 cycles for the composites doped with different CuO (0.5M) contents (x). As we can see clearly, when the CuO (0.5M) content was $x = 0.3$ and 0.4, the composites presented stable repeatability performances in 30 reduction-oxidation cycles, reaching a complete re-oxidation conversion in each cycle. In addition, as the reduction-oxidation cycle proceeded, the re-oxidation rate improved slightly. However, in the case of the composites with $x \geq 0.5$, the weight change decreased gradually during the cycles. Apparently, the composite with

CuO (0.5M) content of $x \geq 0.5$ suffered a decline of re-oxidation rate in the 30 cycles, resulting in an insufficient re-oxidation time. The weight loss for the composite with x = 0.5 did not recover completely in the cooling step from the 12th cycle. Ultimately, β = 0.89 of re-oxidation conversion obtained after the temperature decreased from 950 °C to 700 °C in the 30th cycle. Likewise, incomplete re-oxidation in the cooling step took place from the 10th cycle for the composite with CuO (0.5M) content of x = 0.6, resulting in a re-oxidation conversion of β = 0.75 after the cooling step of the 30th cycle. These results clarify that the CuO content was associated with the repeatability performance of the CuO-doped cobalt oxide system.

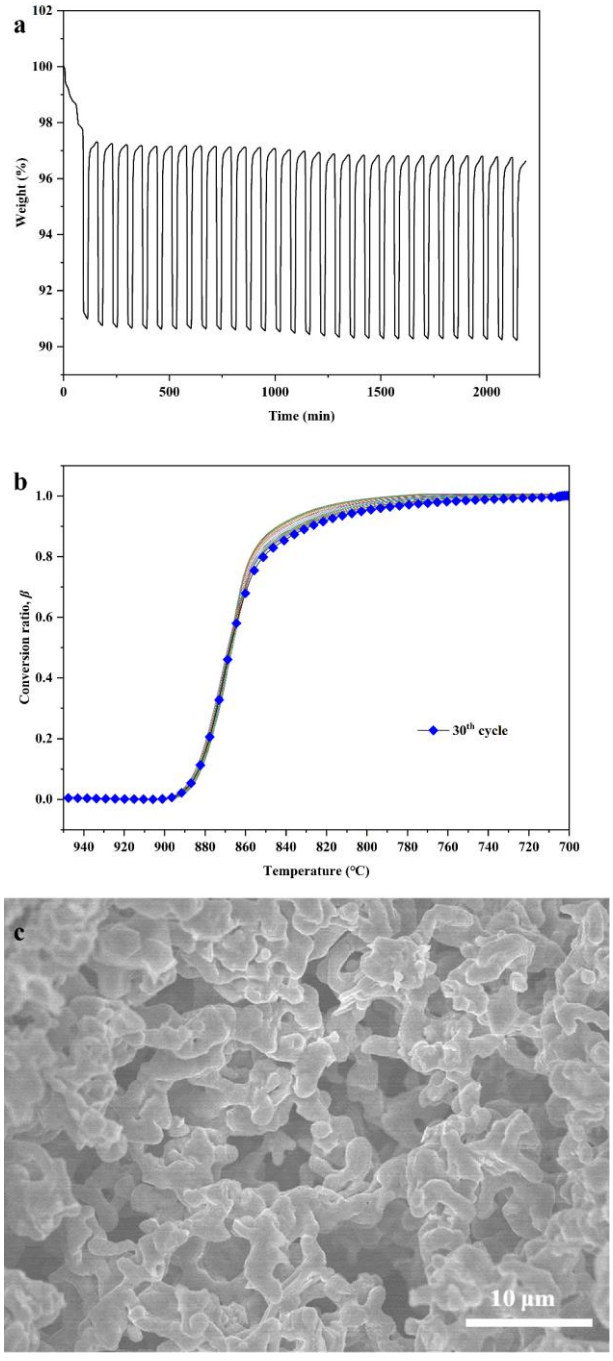

Figure 2-11. (a) TGA curves and (b) evolutions of re-oxidation conversion in 30 reduction-oxidation cycles and (c) SEM image taken after 30 cycles for pure cobalt oxide.

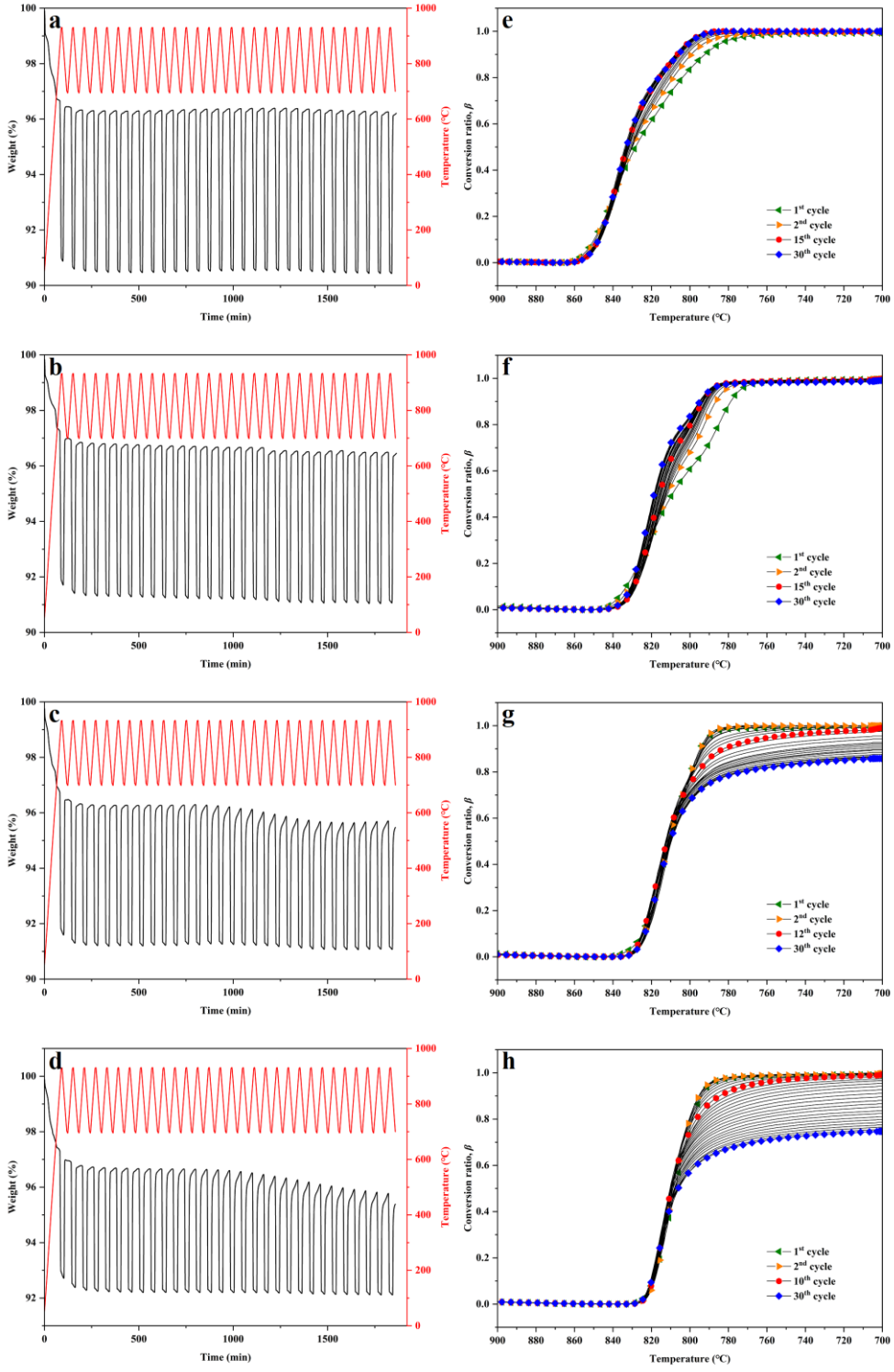

Figure 2-12. TGA curves and evolutions of re-oxidation conversion in 30 reduction-oxidation cycles for composites doped with different CuO (0.5M) contents (x): (a and e) x = 0.3, (b and f) x = 0.4, (c and g) x = 0.5, and (d and h) x = 0.6.

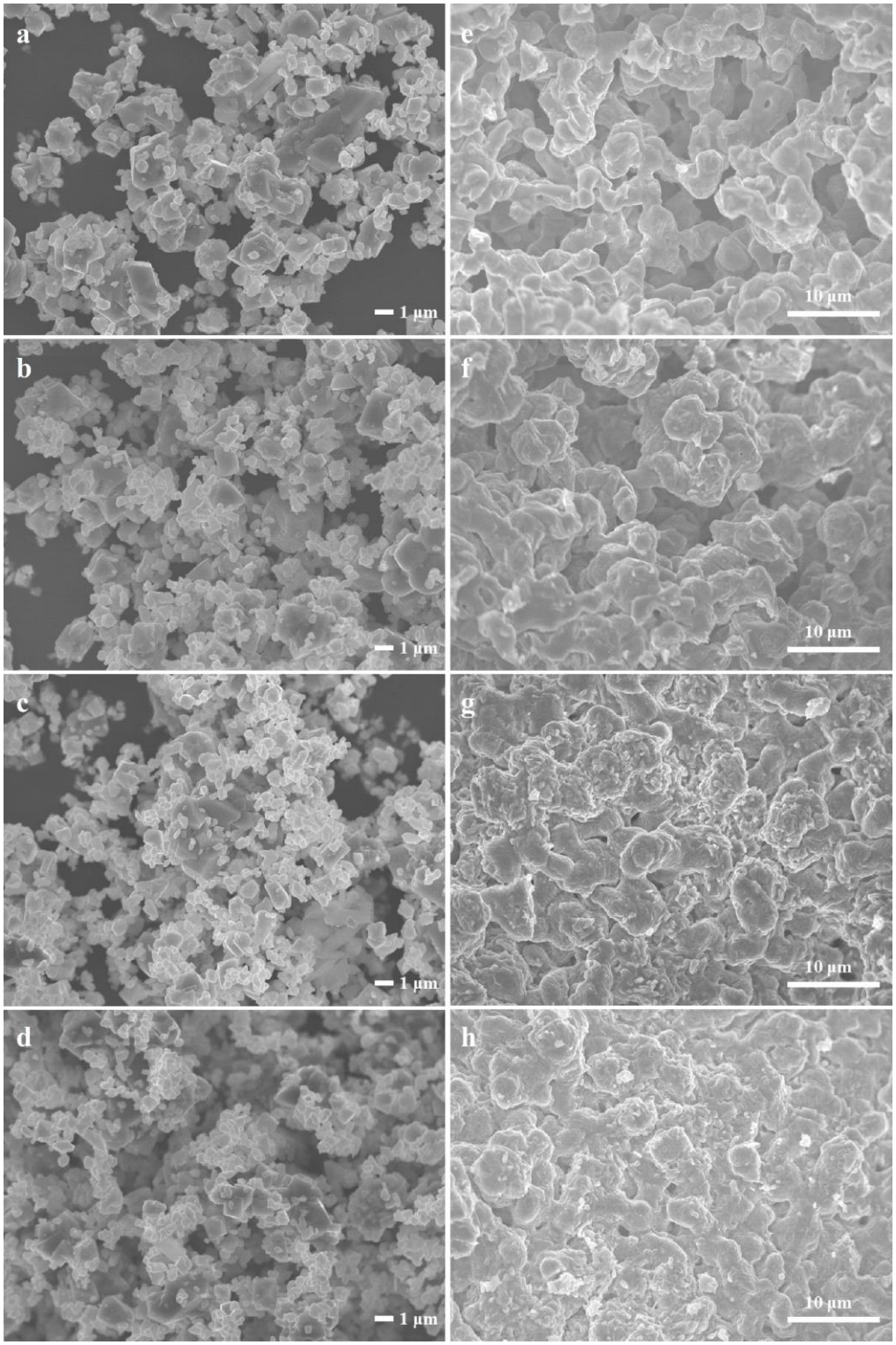

Figure 2-13. SEM images taken before and after 30 cycles for composites doped with different CuO (0.5M) contents (*x*): (a and e) *x* = 0.3, (b and f) *x* = 0.4, (c and g) *x* = 0.5, and (d and h) *x* = 0.6.

Figure 2-13 shows the SEM images taken before and after the 30 cycles for the composites doped with different CuO (0.5M) contents (x). The particle size of the employed Co_3O_4 was relatively large compared to the CuO particles in this work. Thus, it is possible to observe from the SEM images of the fresh composites that CuO particles dispersed on the surface of Co_3O_4 particles. Also, agglomerate morphologies could be appreciated for all the fresh composites. While the morphologies changed dramatically after the 30 cycles owing to a sintering process. Typical necks formed between inter-particles for all the composites after the 30 cycles. It can be appreciated that the composites with CuO (0.5M) content of x = 0.3 and 0.4 presented coral-like array morphologies with large open pores among the bulks, which were similar to the morphology of pure cobalt oxide after the 30 cycles (Figure 2-11c). Furthermore, no CuO particles could be distinguished from the bulk. For the composites with CuO (0.5M) content of $x \geq 0.5$, non-uniform morphologies with less voids were exhibited. Meanwhile, several particles still could be appreciated on the surface of the bulk after the 30 cycles. B. Wong et al. have pointed out that the decreasing of re-oxidation conversion over cycling might relate to the morphological changes which affected the oxygen mass transfer [76]. Thereby, the different morphologies of the composites shown in Figure 2-13 might explain the different repeatability performances of the composites. The large pores in the composites with CuO (0.5M) content of x = 0.3 and 0.4 were beneficial for the oxygen diffusion, leading to the stable re-oxidation rate and the excellent repeatability. Whereas the relatively dense morphologies presented in the composites with CuO (0.5M) content of $x \geq 0.5$ hindered the oxygen diffusion, leading to the low re-oxidation rate and the deterioration in repeatability. It is reasonable to infer that CuO doping somehow affected the sintering process of cobalt oxide which caused different morphological changes, leading to different reduction-oxidation repeatability behaviors.

It is generally well known that solid state sintering is accompanied by coarsening and densification phenomena (Figure 2-14). These two phenomena are usually in competition. When the sintering process is dominated by densification, the voids among contacting particles become smaller and disappear and the material shrinks, whereas when the sintering process is dominated by coarsening, the particles grow by consuming the neighboring particles and the voids among particles become larger [115-117]. As shown in Figure 2-13, the necks within the composites were wider than those presented in pure

cobalt oxide (Figure 2-11c). It might be due to the coarsening of cobalt oxide by consuming the neighboring CuO particles. The individual particles presented in the composites with x = 0.5 and x = 0.6 might be associated with an inadequate coarsening. The high doping amount of CuO might lead to a sintering process dominated by densification process.

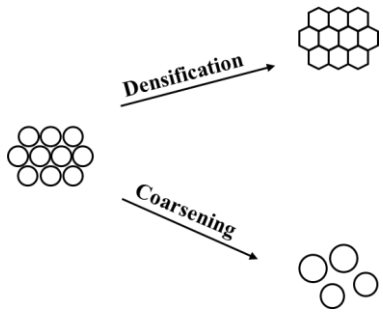

Figure 2-14. Schematic of two possible phenomena during solid state sintering process [79].

To further investigate the effect of CuO doping on the morphology evolution and the repeatability behavior of cobalt oxide-based system. CuO powders with different particle sizes (i.e. CuO (0.01M), CuO (0.05M), and CuO (0.025M)) were utilized to prepare CuO-doped cobalt oxide composites. The CuO content doped in the composite was determined as x = 0.6. It is possible to appreciate the different particle sizes of the CuO particles from the SEM images of the fresh composites (Figure 2-16 (a-c)). In addition, the values corresponding to the redox behaviors of these composites were summarized in Table 2-2. The composites were tested in 30 reduction-oxidation cycles by TGA with a heating/cooling rate of 10 °C/min. Figure 2-15 displays the TGA curves and the evolutions of re-oxidation conversion in 30 cycles for the composites. It can be observed that doping with smaller particle sizes of CuO improved the repeatability by comparing with the performance of the composite doped with CuO (0.5M) shown in Figure 2-12 (d and h). The composites doped with CuO (0.1M) and CuO (0.05M) suffered a decrease in the re-oxidation rate, leading to an incomplete re-oxidation in the cooling step from the 14^{th} cycle for the composite doped with CuO (0.1M) and from the 17^{th} cycle for the composite doped with CuO (0.05M). Ultimately, β = 0.85 and β = 0.91 were obtained after the cooling step of the 30^{th} cycle for the composites doped with CuO (0.1M) and

CuO (0.05M), respectively. In contrast, the composite doped with CuO (0.025M) which presented the relatively small particle size of CuO exhibited a stable repeatability performance, reaching a complete re-oxidation in each cooling step. Moreover, the composite with CuO (0.025M) content of $x = 0.6$ was subjected to a more extreme cycling experiment. As shown in Figure 2-17, the composite still presented an excellent repeatability behavior in 50 cycles.

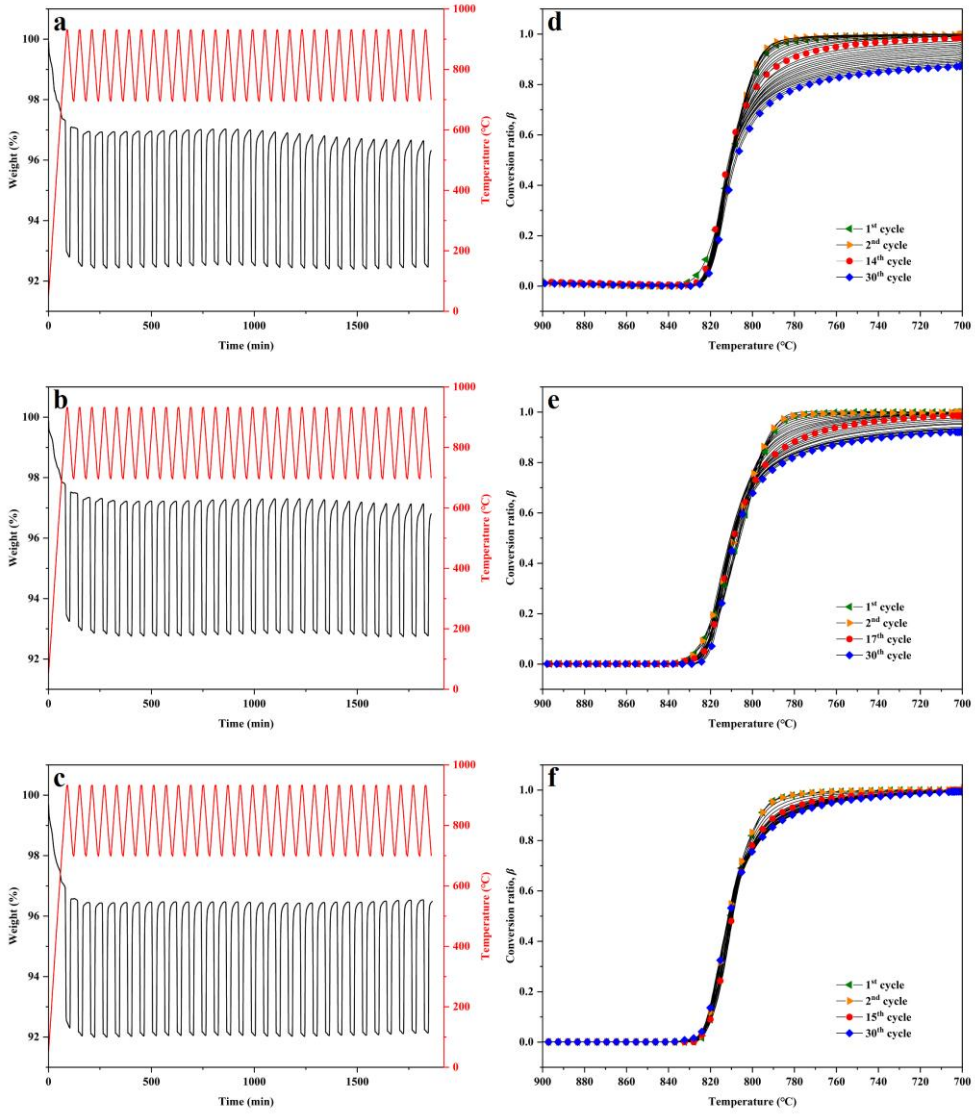

Figure 2-15. TGA curves and evolutions of re-oxidation conversion in 30 reduction-oxidation cycles for composites doped with CuO content of $x = 0.6$: (a and d) CuO (0.1M)-doped composite, (b and e) CuO (0.05M)-doped composite and (c and f) CuO (0.025M)-doped composite.

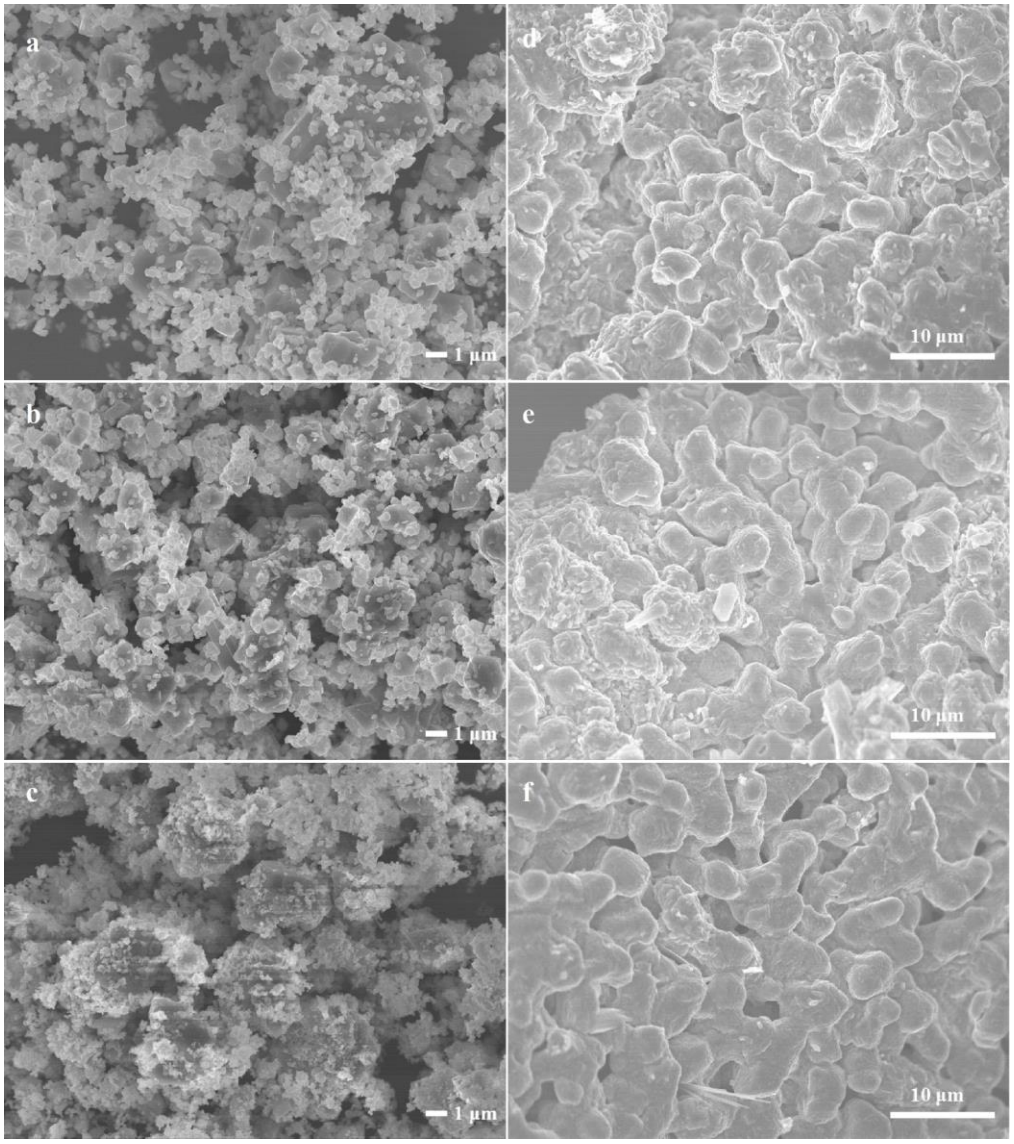

Figure 2-16. SEM images taken before and after 30 cycles for composites doped with CuO content of x = 0.6: (a and d) CuO (0.1M)-doped composite, (b and e) CuO (0.05M)-doped composite and (c and f) CuO (0.025M)-doped composite.

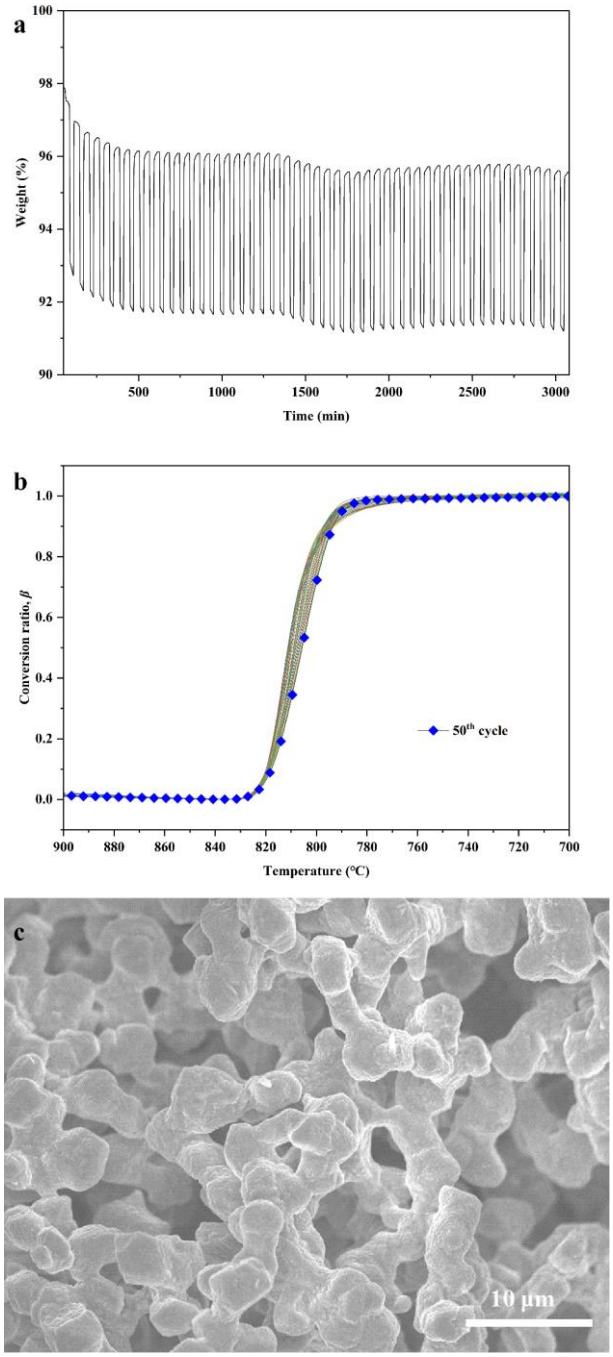

Figure 2-17. (a) TGA curves and (b) evolutions of re-oxidation conversion in 50 reduction-oxidation cycles and (c) SEM image taken after 50 cycles for composite doped with CuO (0.025M) content of x = 0.6.

The SEM images taken after 30 reduction-oxidation cycles for the composites doped with different particle sizes of CuO are shown in Figure 2-16. By comparing, the composites

with CuO (0.1M) and CuO (0.05M) exhibited relatively high densification after the 30 cycles that there were less pores presented, whereas the composite doped with CuO (0.025M) exhibited more pores after the 30 cycles. Moreover, the composite still presented several open pores after 50 reduction-oxidation cycles (Figure 2-17c). Particles could be observed hardly from the surface of the bulk for the composite doped with CuO (0.025M), which might be due to the high degree of coarsening. The result indicates that doping with CuO that presented relatively small particle size might be conducive to following a coarsening-favorable sintering process, leading to a positive effect on the repeatability performance for CuO-doped cobalt oxide composite.

2.4 Summary

In this study, the effects of CuO doping on the redox behavior and repeatability performance of cobalt oxide for TCS applications were experimentally investigated. The major conclusions can be summarized below:

(1) Doping with CuO significantly decreased the onset temperature of reduction by 60 °C compared to pure cobalt oxide. Meanwhile, the result verifies that the onset temperature of re-oxidation could be tuned in the range from 825 °C to 890 °C by altering the doping amount of CuO.

(2) The structural transformation of CuO-doped cobalt oxide composite during reduction/re-oxidation process was confirmed by in-situ XRD. It was found that CuO was involved in the reduction/re-oxidation process of cobalt oxide. Cu species doped in the cobalt oxide structure during the reduction process and separated out during the re-oxidation process.

(3) The repeatability performance of CuO-doped cobalt oxide composites was highly affected by the doping amount of CuO. Deterioration in the repeatability performance was observed with the increase of CuO doping amount. However, CuO with relatively small particle size exhibited a positive effect on improving the repeatability of CuO-doped cobalt oxide composites.

(4) Doping CuO in cobalt oxide by a mechanical mixing process was proved to be a feasible approach to prepare Cu-doped cobalt oxide materials for TCS applications.

Chapter 3. $LiCoO_2$-doped cobalt oxide composites for thermochemical energy storage

3.1 Introduction

Cobalt oxide was considered as the most attractive candidate for metal oxide-based redox thermochemical energy storage (TCS) applications owing to its remarkable reaction repeatability performance and high energy storage density. However, the high operating temperature, especially the reduction temperature is over 900 °C, limits the possible applications not only in concentrated solar power plants but also in other areas such as industrial waste heat recovery. Currently, doping with foreign metal components in cobalt oxide has been proved to be an alternative approach to change the chemical properties of metal oxides. Hence, in this study, doping approach was used to lower the operating temperature and open up more possibilities for the use of cobalt oxide-based TCS systems. It is worthy to mention that lithium compounds were frequently used as an adjuvant or enhancer in several TCS systems [118]. Addition with lithium compounds was found to be beneficial to lower the dehydration temperature, improve the heat output density and enhance the reactivity of reaction process in dehydration/hydration system (i.e. $CaO/Ca(OH)_2$ system and $MgO/Mg(OH)_2$ system) [119-127]. Addition with lithium compounds also was found to promote the carbonation of $MgO/MgCO_3$ system [128]. To the best of our knowledge, there have been few studies reporting the effects of doping lithium compounds on metal oxide-based TCS systems. In this study, lithium cobalt oxide ($LiCoO_2$) was employed as a dopant to prepare cobalt oxide-based composites. $LiCoO_2$ has been widely used for lithium-ion batteries. The basic reaction of $LiCoO_2$ in a lithium-ion battery is well known to be lithium ions extraction from or insertion into a layered cobalt dioxide matrix by varying the interlayer distance [129]. Accordingly, $LiCoO_2$ was exploited as the support of Pt catalyst to control the lattice strain of Pt catalyst and thus to tune the catalytic activity in the oxygen reduction reaction [130].

In this study, we proposed a composite of $LiCoO_2$-doped cobalt oxide, prepared by a mechanical mixing process, for use in TCS applications. The redox behavior of the composites was investigated, especially the onset reaction temperatures and the reaction

rates. The optimum doping amount of $LiCoO_2$ was determined. The reduction/re-oxidation process of the composite was explored and discussed. Additionally, the repeatability performance of the composite was tested.

3.2 Experimental section

3.2.1 Materials preparation

Co_3O_4 powder (99.99%, Kanto Chemical CO., INC.) and $LiCoO_2$ powder (99.988%, Toshima Manufacturing CO., Ltd.) were used as received. Certain amount of Co_3O_4 and $LiCoO_2$ powder were weighed and put in a mortar. To avoid the deviation generated in the milling process, the total weight of each sample was weighed in around 1000 mg. Materials were carefully mixed by hand, grinding with a speed of ~2 laps per second for 20 min. In this work, samples with different doping amounts of $LiCoO_2$ were prepared. The molar ratio, *x*, is defined as,

$$x = \frac{m_{LiCoO2}/\mathrm{M_{LiCoO2}}}{m_{LiCoO2}/\mathrm{M_{LiCoO2}} + m_{Co3O4}/\mathrm{M_{Co3O4}}} \quad (3\text{-}1)$$

where m_{LiCoO2} is the weight of $LiCoO_2$, and M_{LiCoO2} is the molar mass of $LiCoO_2$. m_{Co3O4} is the weight of Co_3O_4, and M_{Co3O4} is the molar mass of Co_3O_4.

3.2.2 Characterization

The crystal structures of samples were identified by an X-ray diffraction (XRD; Rigaku Ultima IV) with Cu Kα radiation (40 kV/ 30 mA). The cell parameters of CoO phases of samples were derived from (111) (200) (220) facets, basing on Bragg's law.

The morphologies of samples were collected by a scanning electronic microscope (SEM; JEOL JSM-7500FA).

3.2.3 Redox investigation of materials

The reduction/re-oxidation process of the sample was performed by a thermogravimetric analyzer (TGA; HITACHI STA7300). In general, reduction and re-oxidation steps were performed in an air atmosphere under a constant flow of 200 mL/min. Typically, the temperature program for one reduction-oxidation cycle consisted of a heating step from 700 °C to 1000 °C with following holding for 5 min and then a cooling step from 1000 °C to 700 °C with following holding for 5 min. Heating/cooling steps were performed with

ramping rates of ±10 °C/min. Also, the repeatability performance of the composite was performed by TGA with appropriate temperature procedures. Each sample was weighed in approximately 10 mg. During the reduction process, oxygen released leading to a weight loss of sample. During re-oxidation process, oxygen uptake occurred leading to a weight gain of sample. The weight change, α (%), is defined as,

$$\alpha = \frac{m_i - m_t}{m_i} \times 100 \quad (3\text{-}2)$$

where m_i is the initial weight of sample, and m_t is the weight at time t. Due to the possible impurities existed in samples, initial weight of the second cycle was used as the initial weight for each sample.

Moreover, the conversion ratio of reduction/re-oxidation, β (%), is defined as,

$$\beta = \frac{m_0 - m_t}{m_0 - m_f} \times 100 \quad (3\text{-}3)$$

where m_0 is the initial weight of sample before the reduction/re-oxidation process, m_t is the weight at time t, and m_f is the final weight of sample after the reduction/re-oxidation process.

The apparent activation energy of reduction and oxidation for samples were calculated by isoconversional Friedman method [86, 131, 132], which is represented by the following equation:

$$\ln\left[i \cdot \left(\frac{\mathrm{d}\beta}{\mathrm{d}T}\right)\right] = \ln[Af(\beta)] - \frac{E}{\mathrm{R}T} \quad (3\text{-}4)$$

where i is the heating rate (K/min), β is the conversion ratio, A is the pre-exponential factor, $f(\beta)$ is the reaction model, E is the apparent activation energy (J/mol), R is the gas constant (8.314 J/K/mol), T is the temperature (K) at which the extent of conversion β is reached under the heat rate i. For each given β, the apparent activation energy E is determined from the slope of the plot of $\ln[i\cdot(\mathrm{d}\beta/\mathrm{d}T)]$ against $1/T$. The apparent activation energy of reduction was calculated based on the heating rate of 5, 10, 15 and 20 K/min. The apparent activation energy of oxidation was calculated by reduced samples based on the heating rate of 1, 3, 5 and 10 K/min. To obtained reduced samples, the as-prepared samples were heated to 1000 °C in air, and then cooled down to room temperature in nitrogen.

To study the heat charging and discharging during reduction and re-oxidation process, a simultaneous thermogravimetry-differential scanning calorimetry (TG-DSC, NETZSCH

STA449F3) was carried out. The temperature procedure consisted of a heating step from 30 °C to 1020 °C with following holding for 30 min and then a cooling step from 1020 °C to 100 °C with following holding for 5 min. Both heating and cooling steps were performed in an air atmosphere under a constant flow of 100 mL/min with certain ramping rates.

In addition, the reduction/re-oxidation process was analyzed by in-situ X-ray diffraction (in-situ XRD; Rigaku SmartLab 3 kW) with Cu Kα radiation (40 kV/ 40 mA). The powder patterns were recorded during a heating/cooling process between 30 °C and 1000 °C under an air atmosphere.

3.3 Results and discussion

3.3.1 Characterization of materials

Figure 3-1 shows the XRD patterns of these samples. All mixed samples presented the characteristic reflections of $LiCoO_2$ phase (PDF: 01-070-2685) and Co_3O_4 phase (PDF: 00-043-1003). No new diffraction peaks were detected after mixing process. Figure 3-2 shows the SEM images of these samples. Each sample shows an agglomerate morphology with terraced structure made of particles. Obviously, different particle sizes can be observed between Co_3O_4 ($\geq$ 1μm) and $LiCoO_2$ ($\leq$ 0.5μm). Therefore, it is possible to distinguish $LiCoO_2$ particles from Co_3O_4 particles. As we can see in the images taken from mixed samples, individual $LiCoO_2$ particles dispersed on the surface of Co_3O_4. What is more, different amounts of $LiCoO_2$ particles can be observed.

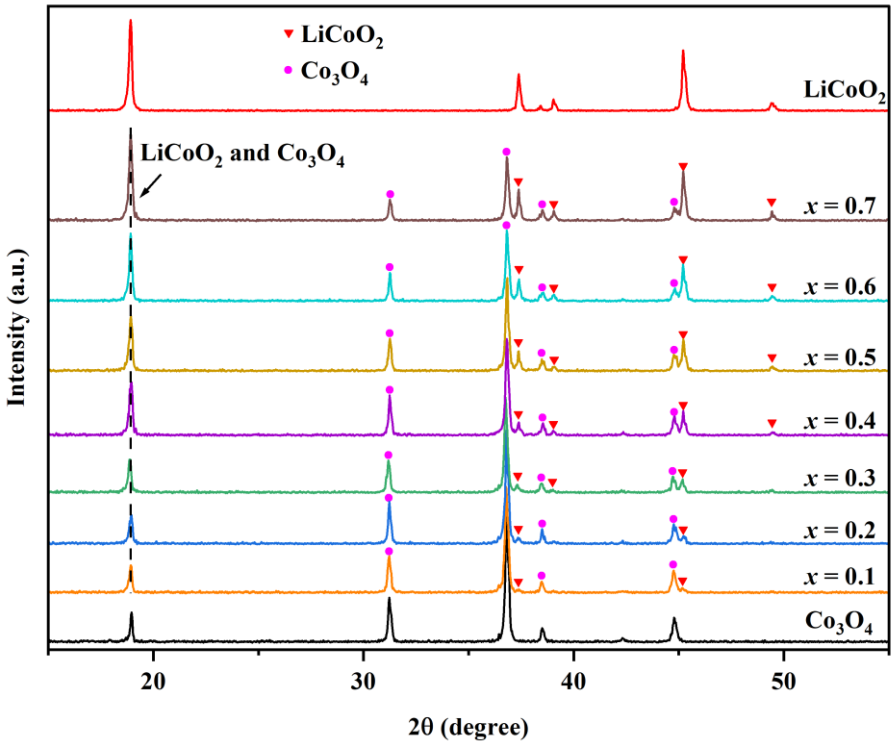

Figure 3-1. XRD patterns of Co_3O_4, $LiCoO_2$ and mixed samples with different molar ratios (x)

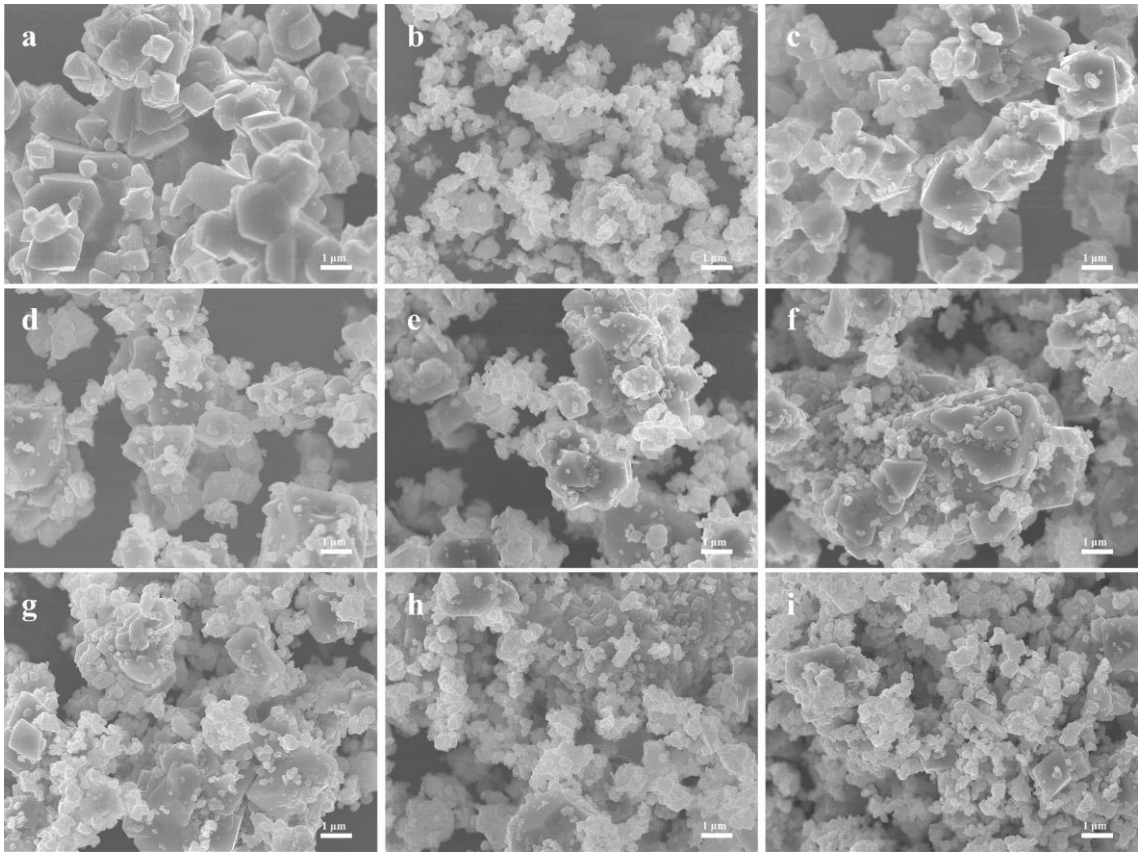

Figure 3-2. SEM images of (a) Co_3O_4, (b) $LiCoO_2$ and mixed samples with molar ratios of (c) x = 0.1, (d) x = 0.2, (e) x = 0.3, (f) x = 0.4, (g) x = 0.5, (h) x = 0.6, and (i) x = 0.7.

3.3.2 Redox behaviors of samples

The redox behaviors of samples with different molar ratios (x) were explored. Figure 3-3 shows the TGA results of samples with different molar ratios (x). The redox performances of pure $LiCoO_2$ and cobalt oxide were also tested. As shown in Figure 3-3, there was no reversible reaction occurred for pure $LiCoO_2$ under the configured temperature program. In terms of mixed samples and pure Co_3O_4, there was an initial weight loss before the rapid weight loss for each sample in the first heating step, which may be attributed to two reasons: (1) the absorbed compounds like water, CO_2, and O_2 were irreversibly eliminated [79, 99]; (2) oxygen vacancies were generated in the crystal lattice of metal oxide at elevated temperature (with corresponding loss of oxygen), which caused by point defect [111, 112]. And then, a rapid weight loss occurred with the increasing temperature from 700 °C to 1000 °C for each sample due to the oxygen release in reduction process. Subsequently, the weight of each sample increased with the decreasing temperature from 1000 °C to 700 °C due to the oxygen uptake in re-oxidation process. Apparently, different redox behaviors with respect to reduction/re-oxidation temperature and weight change can be observed among mixed samples and pure Co_3O_4. The reduction/re-oxidation temperature will be discussed in Figure 3-4 and Figure 3-5. The important matter about reduction/re-oxidation temperature illustrated in Figure 3-3 is that the mixed samples exhibited relatively low reduction/re-oxidation temperature in comparison with pure Co_3O_4.

In terms of the weight change, it is clearly visible that the weight change corresponding to the amount of oxygen release/uptake decreased with increasing doping amount of $LiCoO_2$ (i.e., with increasing molar ratios (x)). The weight loss upon reduction was nearly α = 6.5% and the main weight gain upon re-oxidation was nearly α = 6.3% for pure Co_3O_4. In the case of mixed samples, the rapid weight loss for the mixed samples with molar ratios of x = 0.1, 0.2, 0.3, 0.4, 0.5, 0.6, and 0.7 were nearly α = 6.4%, 5.9%, 5.5%, 5.2%, 4.6%, 4.0%, and 3.3%, respectively. Then, in the subsequent re-oxidation process, the main weight gain for the mixed samples with molar ratios of x = 0.1, 0.2, 0.3, 0.4, 0.5, 0.6, and 0.7 were nearly α = 6.2%, 5.7%, 5.3%, 5.1%, 4.5%, 4.0%, and 3.3%, respectively.

A slight deviation of weight change between reduction and re-oxidation steps occurred for the samples with molar ratios (x) ≤ 0.5. When the molar ratios (x) > 0.5, the weight recovered completely. As we can observe in Figure 3-3, the re-oxidation rate of the samples with molar ratios (x) ≤ 0.5 became relatively low in the concluding part of re-oxidation process, leading to partial weight gained slowly.

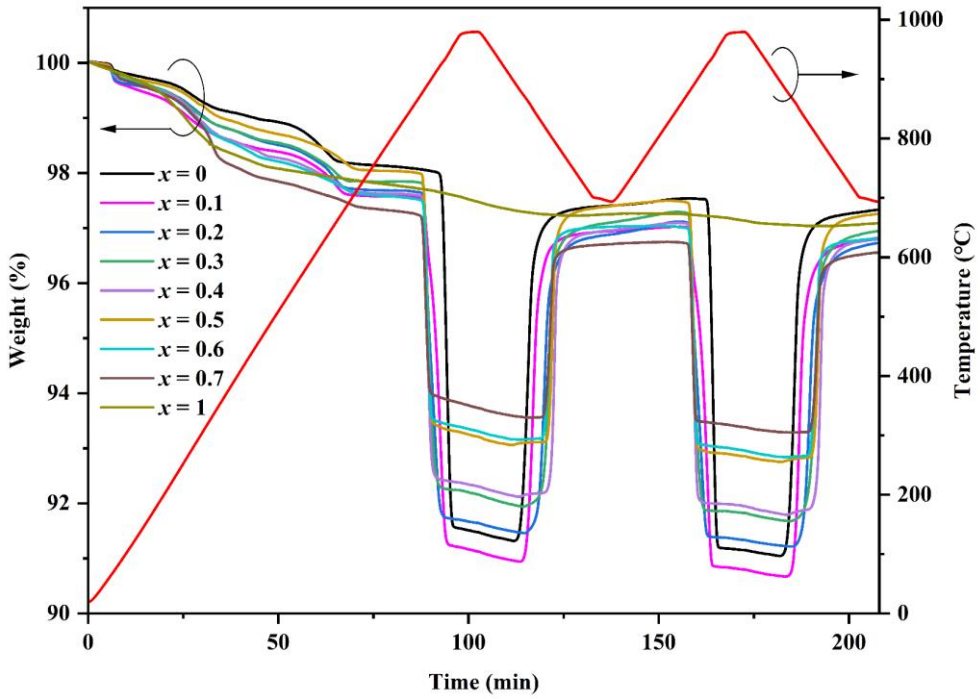

Figure 3-3. Thermogravimetric curves of samples with different molar ratios (x)

Table 3-1 The onset temperature of reduction/re-oxidation and weight change of samples with different molar ratios (x)

Sample	[a]$T_{onset\ red}$ (°C)	[a]$T_{onset\ oxi}$ (°C)	[b]Weight loss (%)	[b]Weight gain (%)
x = 0	925	890	6.5	6.3
x = 0.1	875	870	6.4	6.2
x = 0.2	875	855	5.9	5.7
x = 0.3	875	845	5.5	5.3

x = 0.4	875	825	5.2	5.1
x = 0.5	875	825	4.6	4.5
x = 0.6	875	825	4.0	4.0
x = 0.7	875	825	3.3	3.3

[a] The onset temperature in this work corresponds to the start temperature of sharp weight change under the configured temperature program.

[b] The data of weight loss obtained from the second cycle.

Conversion ratio of reduction and re-oxidation were calculated by eq. (3-3) from the weight change of each sample in reduction and re-oxidation steps performed by TGA with ramping rates of ±10 °C/min. Figure 3-4 shows the conversion ratio of reduction as a function of temperature during the second cycle for samples with different molar ratios (x). As seen in Figure 3-4, the conversion ratio of reduction for each sample increased gradually with increasing temperature. The reduction process of pure Co_3O_4 took place between 925 °C and 955 °C and completed in 3 min. In terms of mixed samples, the reduction process of each mixed sample started at approximately 875 °C, which was lower than that of pure Co_3O_4. When the molar ratio was x = 0.1, the reduction process of the sample took 6.5 minutes and finished at around 940 °C. With the increasing molar ratios from x = 0.1 to 0.4, the reduction rate became faster. When the molar ratio was x = 0.4, the reduction process took 3 min and finished at around 905 °C. Then, as we can observe from Figure 3-4, similar reduction profiles were exhibited for the mixed samples with molar ratios of x = 0.4, 0.5, 0.6, and 0.7. Thus, the mixed sample exhibited an optimum reduction rate when the molar ratio (x) was higher than 0.4. The results reveal that doping with $LiCoO_2$ contributed to lowering the onset temperature of reduction for pure Co_3O_4. Much more interesting, doping amount of $LiCoO_2$ was not related to the onset temperature of reduction but impacted on the reduction rate.

Figure 3-5a shows the conversion ratio of re-oxidation as a function of temperature during the second cycle for samples with different molar ratios (x). As shown in Figure 3-5a, the re-oxidation process of each mixed sample started at a lower temperature in comparison with pure Co_3O_4. Also, it is worthy to note that the onset temperatures of re-oxidation for

mixed samples were obviously different, which differed from the reduction process illustrated in Figure 3-4. Furthermore, Figure 3-5b illustrates the evolution of the onset temperature of re-oxidation as a function of molar ratio (x). When the molar ratio increased from x = 0 to 0.4, the onset temperature of re-oxidation decreased linearly. The onset temperature of re-oxidation for samples with molar ratios of x = 0, 0.1, 0.2, 0.3, and 0.4 were approximately 890 °C, 870 °C, 855 °C, 845 °C and 825 °C, respectively. And then, the onset temperature was constant at 825 °C when the molar ratio increased from x = 0.4 to 0.7. As shown in Figure 3-5a, the conversion ratio of re-oxidation for each sample increased gradually with decreasing temperature. The conversion ratio of pure Co_3O_4 reached nearly β = 95% in 8.5 min when the temperature decreased from 890 °C to 805 °C. Afterwards, the concluding part of the re-oxidation took place slowly in a wide temperature range. When the molar ratio was x = 0.1, the conversion ratio for the mixed sample reached nearly β = 95% in 8.5 min with decreasing temperature from 870 °C to 785 °C. Similarly, the concluding part for the mixed sample also took place slowly. With increasing molar ratios from x = 0.1 to 0.7, the re-oxidation rate was improved gradually, as shown in Figure 3-5a. When the molar ratio was x = 0.4, the conversion ratio of the mixed sample reached nearly β = 95% in approximately 6 min with decreasing temperature from 825 °C to 768 °C. The results illustrated in Figure 3-5 indicate that doping with $LiCoO_2$ leaded to a decrease in the onset temperature of re-oxidation. Moreover, doping amount of $LiCoO_2$ impacted on the onset temperature of re-oxidation as well as the re-oxidation rate. The onset temperatures of reduction/re-oxidation for samples with different molar ratios (x) were also summarized in Table 3-1. Accordingly, the optimum molar ratio for the composite was determined as x = 0.4 with respective to the onset temperature of reduction/re-oxidation, weight change and reduction/re-oxidation rate.

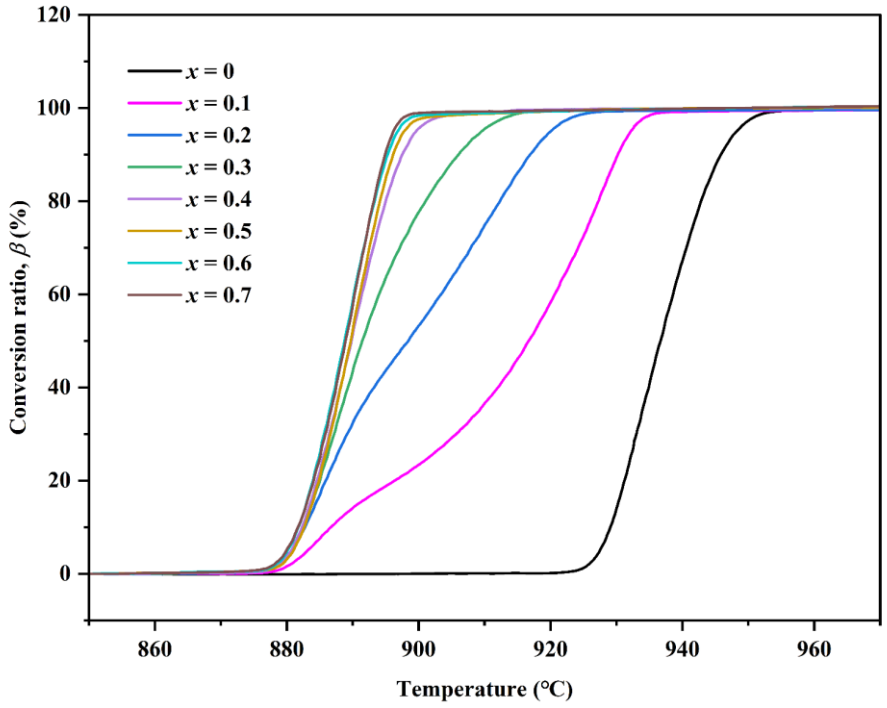

Figure 3-4. Reduction profiles for samples with different molar ratios (*x*)

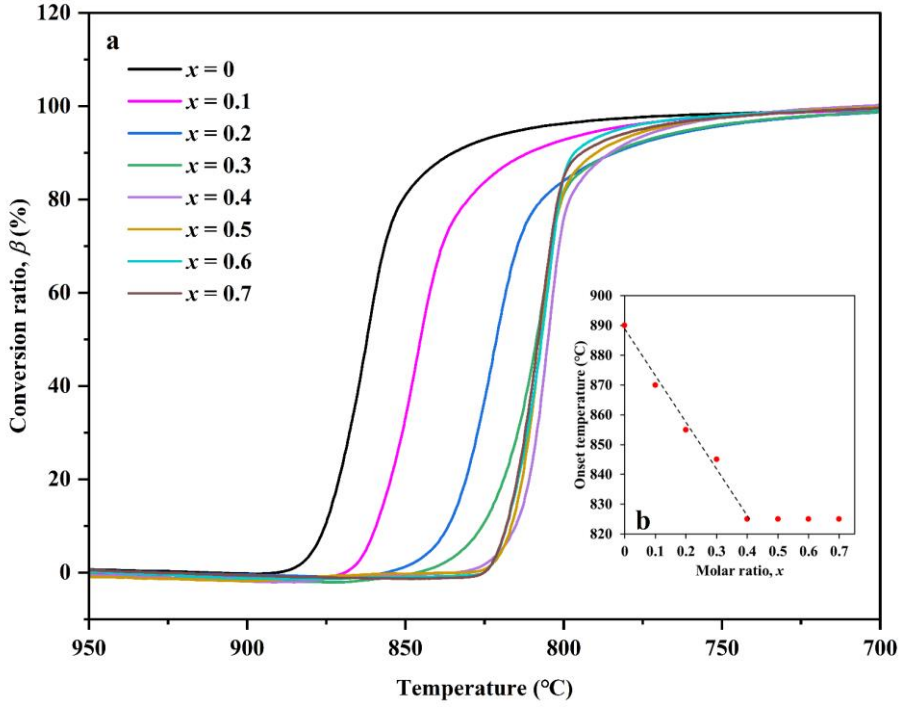

Figure 3-5. (a) Re-oxidation profiles for samples with different molar ratios (*x*) and (b)

Evolution of the onset re-oxidation temperature as a function of molar ratio (x)

The effect of $LiCoO_2$ doping on the redox rate of cobalt oxide was further investigated. Figure 3-6 displays the evolution of reduction/re-oxidation conversion ratio as a function of temperature for pure Co_3O_4 sample and the mixed sample with a molar ratio of x = 0.4 under different heating/cooling rates. As shown in Figure 3-6A, the curves of reduction step under different heating rates were nearly identical for the pure Co_3O_4 sample and the mixed sample. While in the case of re-oxidation step, it can be observed that the higher cooling rate exhibited opposite effect on the re-oxidation for pure Co_3O_4 sample and the mixed sample, leading to incomplete conversions for these two samples when the cooling rate was higher than 10 °C/min. Nonetheless, the mixed sample with a molar ratio of x = 0.4 presented a faster re-oxidation under the higher cooling rate by comparing with pure Co_3O_4 sample, resulting in the higher conversion ratio. As we can see, β = 45% conversion obtained for pure Co_3O_4 sample under the cooling rate of 20 °C/min, while β = 76% conversion obtained for the mixed sample under the same cooling rate. The result indicates that doping with appropriate amount of $LiCoO_2$ contributed to improving the re-oxidation rate of cobalt oxide-based system under a high cooling rate, which might extend the applicability of the composite in terms of operation conditions. The heat-charging/discharging result under a heating/cooling rate of 20 °C/min was measured by DSC with alumina open crucibles. As shown in Figure 3-7, pure Co_3O_4 exhibited a small exothermic peak corresponding to 289.8 kJ/kg, while the mixed sample exhibited a sharp exothermic corresponding to 423.8 kJ/kg. The ratio between charging and discharging heat for pure Co_3O_4 and the mixed sample were 0.46 and 0.74, respectively. This difference in the discharging heat for these two samples under the cooling rate of 20 °C/min may be owing to the different re-oxidation rates as shown in Figure 3-6B.

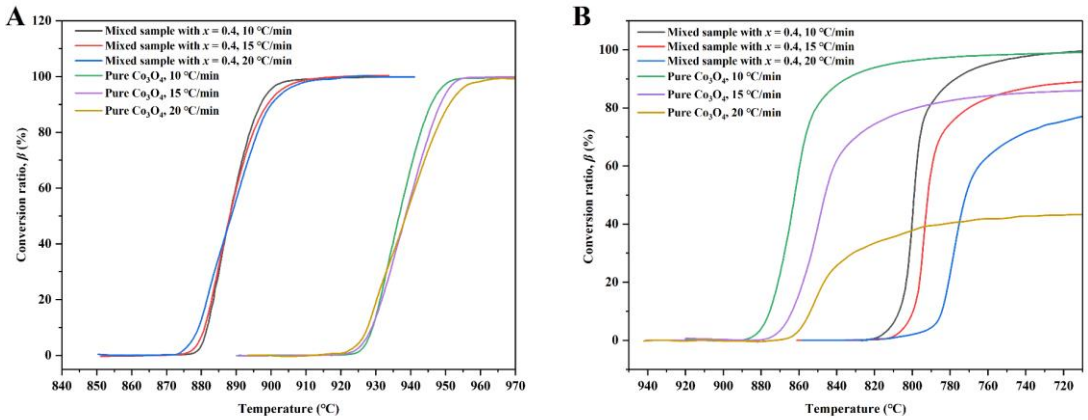

Figure 3-6. (A) Reduction and (B) Re-oxidation profiles for pure Co_3O_4 sample and the mixed sample with a molar ratio of x = 0.4 under different heating/cooling rates.

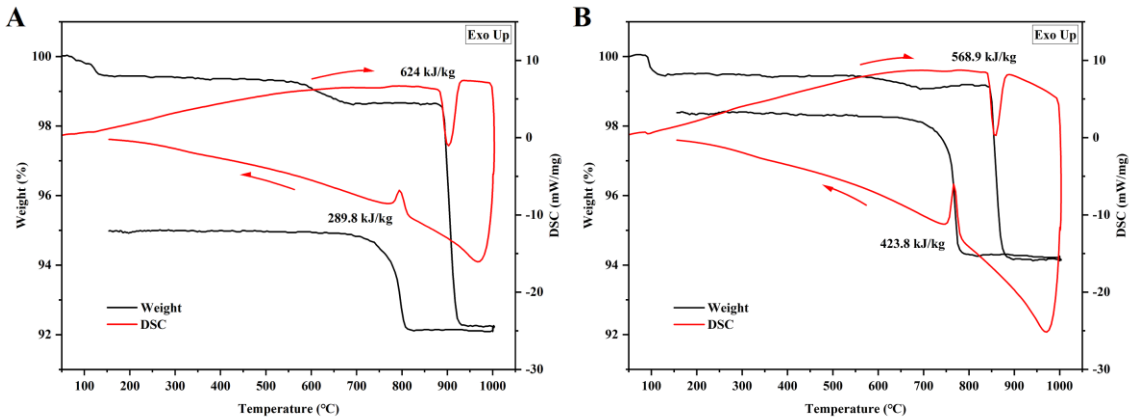

Figure 3-7. DSC curves of (A) pure Co_3O_4 and (B) mixed sample with a molar ratio of x = 0.4 under a heating/cooling rate of 20 °C/min.

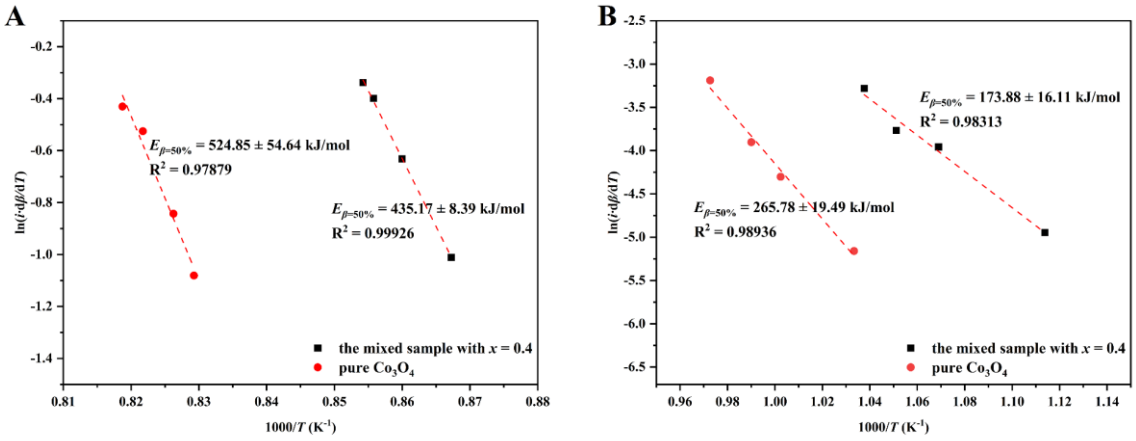

Figure 3-8. Isoconversional plots calculated by Friedman method for the (A) reduction

and (B) oxidation in air (β = 50%)

As reported in Figure 3-8, the apparent activation energy of reduction for the mixed sample with a molar ratio of x = 0.4 and pure Co_3O_4 are 435.17 ± 8.39 kJ/mol and 524.85 ± 54.64 kJ/mol, respectively. Meanwhile, the apparent activation energy of oxidation for the mixed sample with a molar ratio of x = 0.4 and pure Co_3O_4 are 173.88 ± 16.11 kJ/mol and 265.78 ± 19.49 kJ/mol, respectively. By doping with $LiCoO_2$, the apparent activation energy of reduction and oxidation were decreased. The result indicates that doping with $LiCoO_2$ can make reduction and oxidation of cobalt oxide occur more easily.

3.3.3 Redox process exploration of $LiCoO_2$-doped cobalt oxide composites

To understand deeply about the effect of $LiCoO_2$ on the reduction/re-oxidation process of cobalt oxide, in-situ XRD was utilized to explore the process. Figure 3-9 (A-D) shows the in-situ XRD patterns of the mixed sample with a molar ratio of x = 0.4. Figure 3-9A shows the XRD patterns in the heating step, as we can observe, the sample exhibited both $LiCoO_2$ phase (PDF: 01-070-2685) and Co_3O_4 phase (PDF: 00-043-1003) clearly at room temperature. When temperature was higher than 850 °C, the intensity of diffraction peaks decreased with the increasing temperature. Ultimately, the XRD patterns at 950 °C exhibited a single phase of CoO (PDF: 01-076-3829). This behavior demonstrates that both Co_3O_4 and $LiCoO_2$ were converted into CoO. It seemed that the Li species inserted into the CoO lattice and formed a CoO-based solid solution. The in-situ XRD patterns shown in Figure 3-9B illustrates the re-oxidation process in the cooling step. As we can observe, $LiCoO_2$ phase and Co_3O_4 phase reproduced while the CoO phase vanished with the decreasing temperature. It should be noted that the structure is detected by in-situ XRD only when the amount of the material is enough. Consequently, no CoO phase was tested by in-situ XRD when the temperature decreased to 800 °C, which differed from the result illustrated in Figure 3-5 obtained by TGA. The important matter verified by in-situ XRD is that $LiCoO_2$ was involved in the reduction/re-oxidation process.

Figure 3-9C shows the localized in-situ XRD patterns within the 2θ range from 17.5° to 20° in the heating step. The diffraction peak corresponding to the $LiCoO_2$ (003) facets shifted from 18.92° at 30 °C to 18.42° at 890 °C, corresponding to an increase in layer spacing of $LiCoO_2$ from 4.69 Å to 4.81 Å. Similarly, Figure 3-9D shows the localized in-

situ XRD patterns within the 2θ range from 30° to 33° in the heating step. The diffraction peak, corresponding to the Co_3O_4 (220) facets where present abundant of Co^{3+} [133, 134], shifted from 31.26° at 30 °C to 30.82° at 890 °C, corresponding to an increase in the relevant lattice spacing of Co_3O_4 from 2.86 Å to 2.90 Å. In addition, as we can observe from Figure 3-9A, other diffraction peaks of $LiCoO_2$ phase and Co_3O_4 phase also shifted toward the lower angle side. This behavior means that other facets of $LiCoO_2$ and Co_3O_4 crystals also expended in the heating step.

Figure 3-9E shows the in-situ XRD patterns of mixed samples with different molar ratios (x) at 950 °C and Table 3-2 shows the lattice parameter of the CoO phase at 950 °C for these samples. A single CoO phase (PDF: 01-076-3829) was detected for the mixed samples with molar ratios of x = 0.3 and 0.4. When the molar ratio was $x \geq 0.5$, a secondary phase corresponding to $LiCoO_2$ phase (PDF: 01-070-2685) can be observed. Meanwhile, the lattice parameter of CoO decreased from 4.28 Å to 4.24 Å when the molar ratio (x) increased from 0.3 to 0.6, which might be due to the insertion of Li species. Afterwards, the lattice parameter was constant when the molar ratio was $x \geq 0.6$. The result indicates that the amount of Li species in the CoO structure increased with the increasing of $LiCoO_2$ doping amount. Nonetheless, the amount of Li species in CoO structure was limited. This result might account for the different onset temperatures of re-oxidation for mixed samples with different molar ratios (x), as illustrated in Figure 3-5 of Sec. 3.3.2. With an increase in the doping amount of Li species in CoO lattice, the onset temperature of re-oxidation decreased gradually.

Table 3-2 Lattice parameters of CoO phase at 950 °C for mixed sample with different molar ratios (x)

Mixed sample	x = 0.3	x = 0.4	x = 0.5	x = 0.6	x = 0.7
[a]Lattice parameter (Å)	4.28	4.27	4.25	4.24	4.24

[a] Lattice parameter is derived from (111) (200) (220) facets based on in-situ XRD analysis

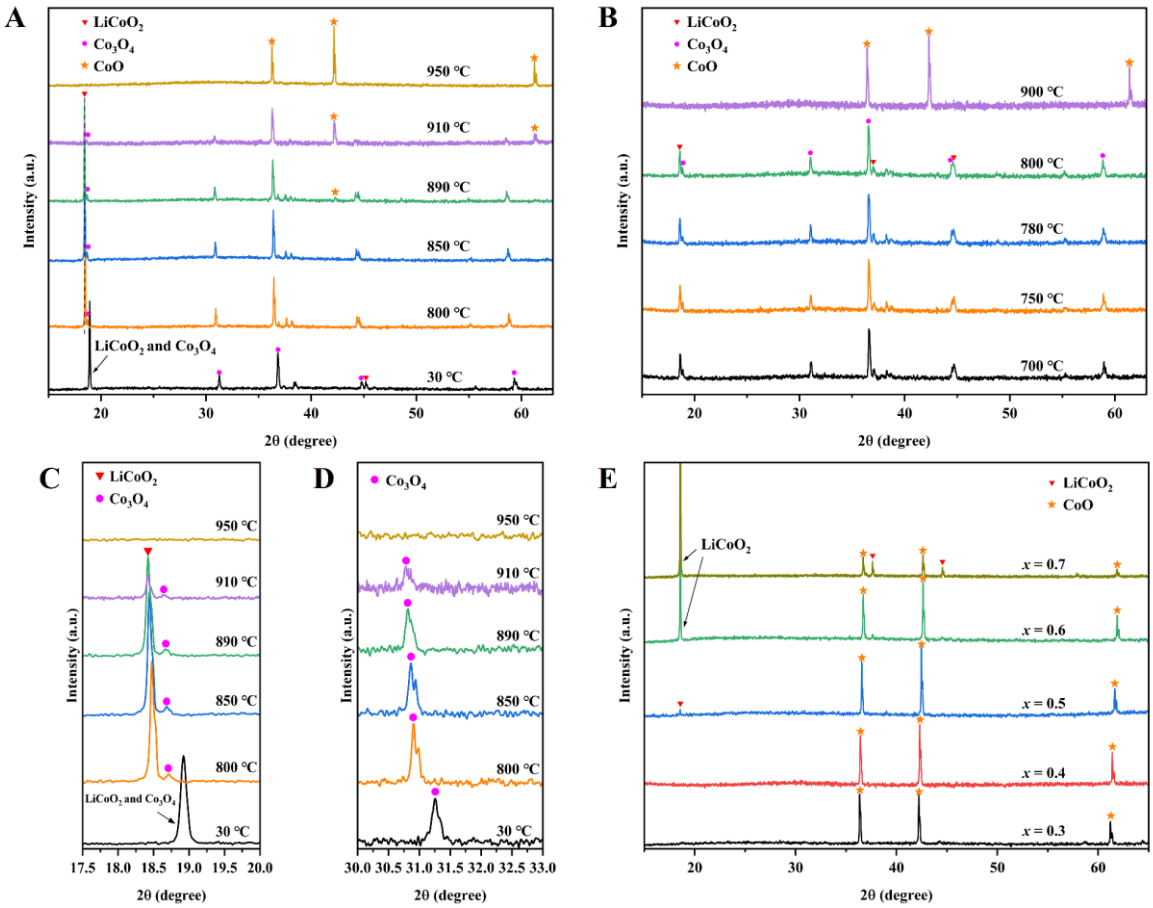

Figure 3-9. In-situ XRD patterns of the mixed sample with a molar ratio of x = 0.4: (A) In the heating step, (B) In the cooling step, (C) Localized XRD patterns within the 2θ range from 17.5° to 20° in the heating step, and (D) Localized XRD patterns within the 2θ range from 30° to 33° in the heating step. And (E) in-situ XRD patterns of mixed samples with different molar ratios (x) at 950 °C

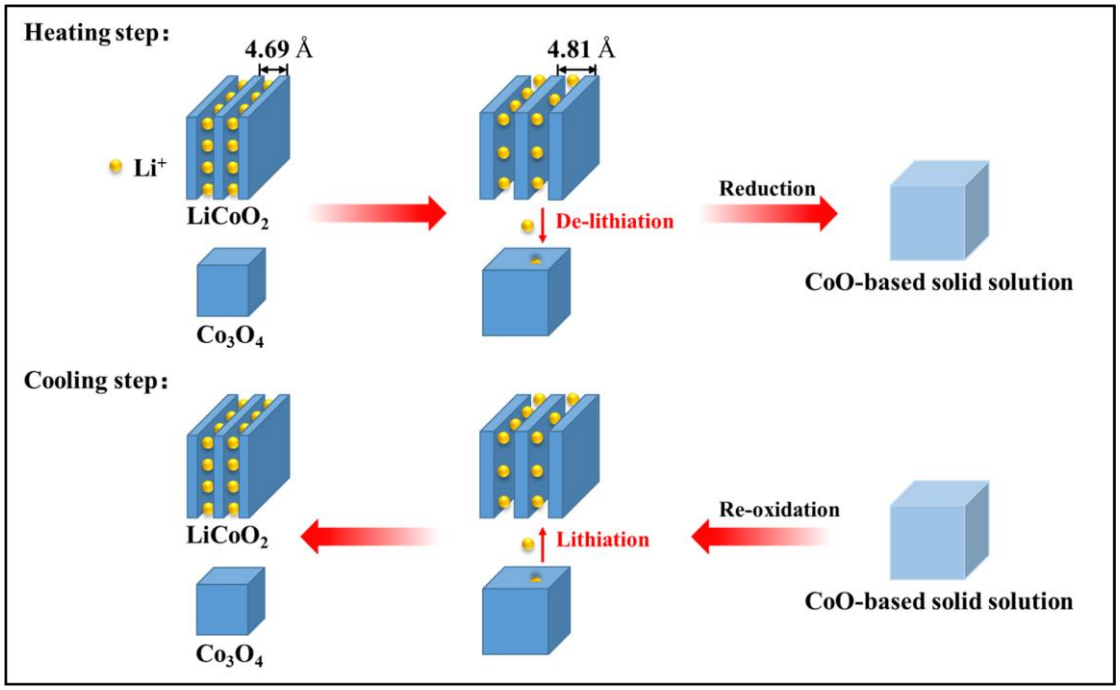

Figure 3-10. Plausible reduction/re-oxidation process of $LiCoO_2$-doped cobalt oxide composite

Combined the in-situ XRD results with the redox behaviors discussed in Sec. 3.3.2, a plausible reduction/re-oxidation process of the $LiCoO_2$-doped cobalt oxide composite was proposed, as shown in Figure 3-10. In heating step, the lattices of $LiCoO_2$ and Co_3O_4 slightly expanded with increasing temperature. It is known that lithium ions will extract from or insert into the layered cobalt dioxide matrix of $LiCoO_2$ by varying the interlayer distance [129, 130]. Thus, partial lithium ions extracted from the layered cobalt dioxide matrix when the interlayer distance of $LiCoO_2$ increased from 4.69 Å to 4.81 Å (De-lithiation process). Simultaneously, the extracted lithium ions inserted into Co_3O_4 lattice, which may render the Co_3O_4 crystal more fragile and stimulate the reduction of Co_3O_4 to start at lower temperature, as discussed in Figure 3-4 of Sec. 3.3.2. Ultimately, $LiCoO_2$ and Co_3O_4 converted into CoO-based solid solution. In cooling step, the reverse oxidation process occurred. The CoO-based solid solution converted to $LiCoO_2$ and Co_3O_4 in relatively low temperature, which may be owing to the doping lithium ions in CoO lattice. At the same time, the lithium ions inserted into the layered cobalt dioxide matrix of $LiCoO_2$ (Lithiation process). We assumed the insertion of lithium into Co_3O_4/CoO has a positive effect on the reduction/re-oxidation process. As a further issue, deeper

investigation is necessary and required.

3.3.4 Repeatability test

To examine the repeatability of the composite. The mixed sample with a molar ratio of x = 0.4, which exhibited an optimum redox behavior, was subjected to 50 runs of reduction/re-oxidation by TGA under an appropriate temperature range. Figure 3-11 shows the TGA result of the subjected sample with 50 runs of reduction/re-oxidation. α = 5.2% weight lost and α =5.1% weight recovered in the second cycle, and α = 5.2% weight lost and α = 5.2% weight recovered in the 50^{th} cycle. This result demonstrates the feasibility of this composite for TCS application as it can be reused for several cycles. Figure 3-12 displays the relevant SEM images of the mixed sample with a molar ratio of x = 0.4. It can be observed that remarkable changes occurred in the morphology of the sample during reduction/re-oxidation cycles. Differing from the as-prepared sample, the used samples presented coral-like morphologies caused by a thermal sintering. Moreover, $LiCoO_2$ particles could not be distinguished from the bulk. As we can observe from the image taken after 2 cycles, the necks with diameter of around 1μm formed between the neighboring particles. Meanwhile, open macro-pores presented among the necks. It is worth noting that the size of the large pores in the bulk increased from cycle to cycle, indicating that further sintering occurred during the subsequent reduction/re-oxidation cycles. The large pores within the coral-like structures maybe conducive to the diffusion of oxygen and facilitate the re-oxidation.

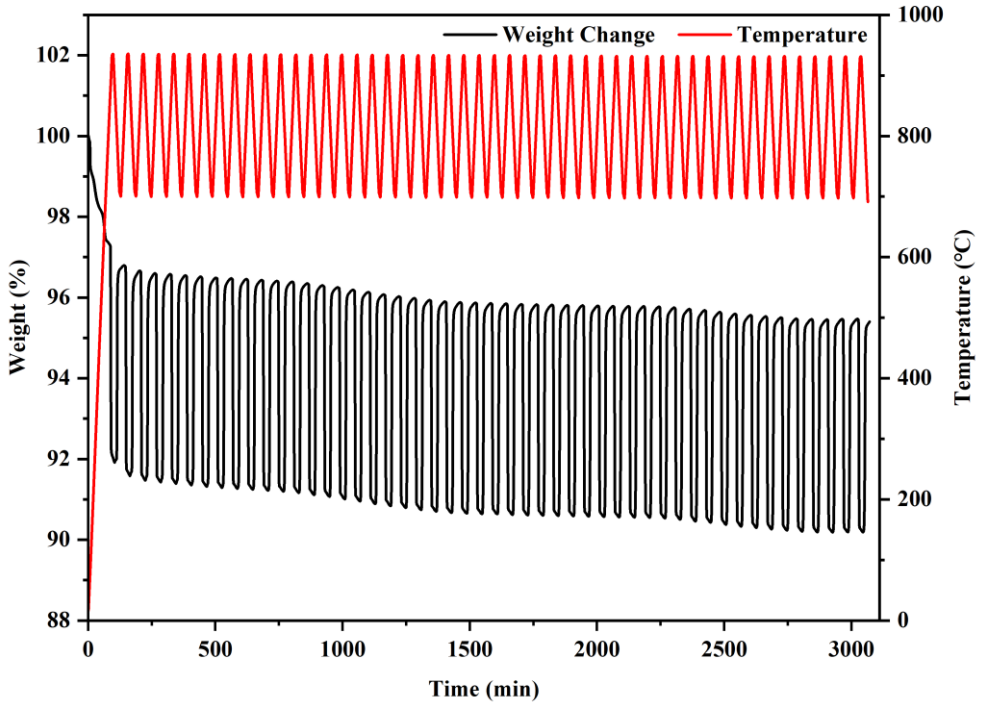

Figure 3-11. Thermogravimetric curve of the mixed sample with a molar ratio of x = 0.4 under 50 runs of reduction/re-oxidation

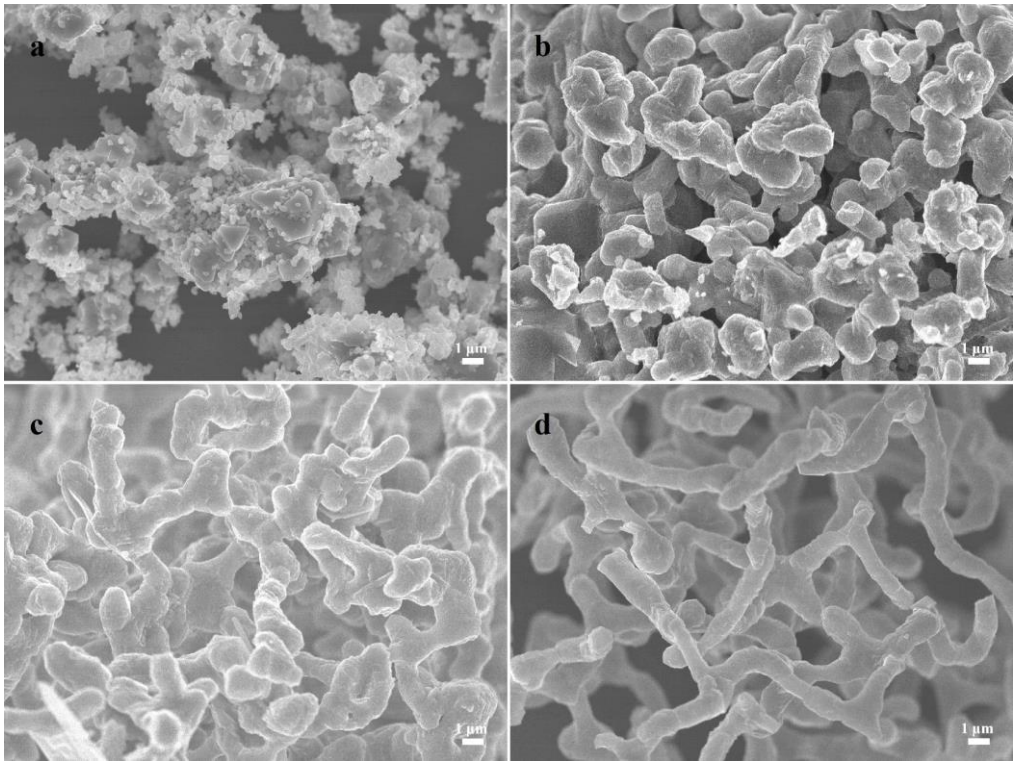

Figure 3-12. SEM images of the mixed sample with a molar ratio of x = 0.4: (a) as-prepared sample, (b) after 2 cycles, (c) after 30 cycles, and (d) after 50 cycles.

3.4 Summary

In summary, $LiCoO_2$-doped cobalt oxide composites were initially proposed and explored for TCS applications. The composites were facilely obtained by a mechanical mixing process, which is advantageous to scale-up research and practical applications. The major conclusions are summarized below.

(1) Doping with $LiCoO_2$ diminished the onset temperature of reduction and re-oxidation by 50 °C and 65 °C, respectively. Doping with an appropriate amount of $LiCoO_2$ contributed to improving the re-oxidation rate of cobalt oxide-based system under a high cooling rate, resulting in a significant increase in the discharging heat (423.8 kJ/kg) compared to pure cobalt oxide (289.8 kJ/kg) under a temperature cooling rate of 20 °C/min. Doping with $LiCoO_2$ was found to decrease the apparent activation energy of reduction and oxidation of cobalt oxide.

(2) In-situ XRD results confirmed that $LiCoO_2$ was involved in the reduction/re-oxidation process of cobalt oxide. The insertion amount of Li species on cobalt oxide appeared to relate to the onset temperature of re-oxidation.

(3) Excellent repeatability performance of this composite was attested in 50 cycles.

Chapter 4. Fabrication of cobalt oxide foams for thermochemical energy storage

4.1 Introduction

To date, several reactor concepts for metal oxide-based redox thermochemical energy storage (TCS) systems have been proposed. For instance, packed beds [93, 104, 135], moving-beds [136], and rotary kilns [92]. The advantages of a packed bed reactor such as simplicity, ease of operation, and ability to store a large amount of thermal energy per unit volume of the storage material make it a popular choice for metal oxide-based TCS systems [104]. While the dense packing of metal oxide particles in a packed bed reactor limits the heat transfer between the particles and heating medium (i.e., air) as well as limits the efficient contact between the particles and oxygen, resulting in low reaction rates and low conversion ratios [93]. In fact, the concept of porous structures, including honeycomb-like and foam-like structures, has been used in several metal oxide-based applications such as V_2O_5-WO_3/TiO_2 honeycomb catalysts for DeNO_x [137] and CeO_2 foams for thermochemical CO_2 splitting [138], which can provide a high surface area to volume ratios and high porosity, allowing for more contact between metal oxides and reactant gases. Porous structures made from metal oxides have also shown promising results in TCS applications [105, 106, 139]. However, further investigation for optimization and improvement are still needed. It should be noted that unlike ceramic foams, which are generally used as inert porous supports, metal oxide foams used in TCS systems are subjected to a high temperature range to undergo a phase change. During this process, reduction occurs, leading to the depletion of oxygen from the metal oxide foams, followed by oxidation, resulting in the insertion of oxygen back into the metal oxide foams. As demonstrated in the previous chapters as well as in literatures [76, 79], the micro-morphology of metal oxides can highly affect the oxidation kinetic. Furthermore, the morphology can undergo continuous changes during reduction-oxidation cycles, which may potentially influence the long-term stability of the porous structure of metal oxides. Therefore, the preparation of a metal oxide foam for TCS should take both of the reaction kinetic of metal oxide and the long-term stability of the porous structure into account. Meanwhile, understanding the morphological change of porous metal oxides

during the reduction-oxidation cycles is critical for optimizing their properties and performance for TCS applications. Hence, this study focuses on the detail of the structural stability and durability of metal oxide foams for TCS applications.

In this study, cobalt oxide foams were prepared using the widely used foam replica method, which is simple and commonly employed for fabricating ceramic foams [140]. Inexpensive polyurethane (PU) foams were used as the templates. The effect of the solid loading of cobalt oxide slurry, sintering temperature, and sintering duration, on preparation of cobalt oxide foams were explored and discussed. Valuable insights into the structural evolutions of cobalt oxide foams during their reduction-oxidation cycles were provided. Moreover, a consecutive immersion approach was used to improve the structure and increase the bulk density of the cobalt oxide foam.

4.2 Experimental section

4.2.1 Fabrication of cobalt oxide foams

The cobalt oxide foams were fabricated by means of a PU foam replica method [140]. PU foams with different pore densities (i.e., ~50 ppi, ~20 ppi, and ~13 ppi, the term "ppi" stands for "pores per inch", indicating the pore density of a foam) purchased from MonotaRO Co., Ltd. were used as templates. Figure 4-1 displays the morphologies of PU foams as captured by a stereomicroscope and shows the diameter distributions of the struts within the PU foams. Open cells with different pore sizes are visible for the PU foams with different pore densities. The PU foam with a higher pore density had a relatively large pore size and exhibited a relatively large diameter in the struts. Furthermore, the struts of the PU foams used in this study exhibited a cross-section in the shape of a triangle as illustrated in Figure 4-2. Co_3O_4 powder (99.99%, Kanto Chemical CO., INC.) with a median particle diameter of around 2 μm (Figure 2-3) was used as received. Polyacrylamide (PAM) was employed as a dispersant to stabilize cobalt oxide particles in the slurry.

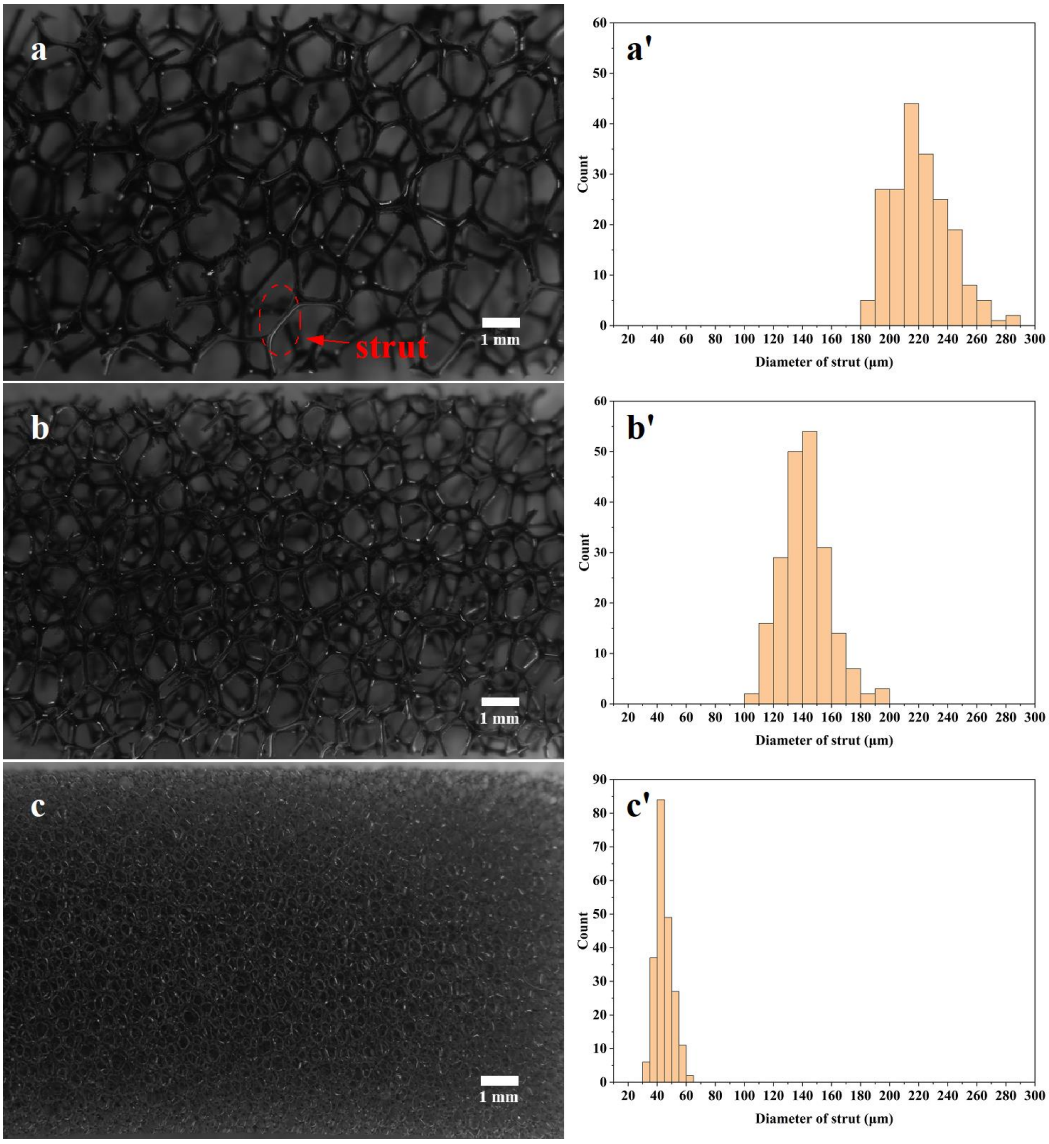

Figure 4-1. Morphologies and diameter distribution histograms of the struts for PU foams with different pore densities: (a) and (a') PU foam with 13 ppi; (b) and (b') PU foam with 20 ppi; (c) and (c') PU foam with 50 ppi.

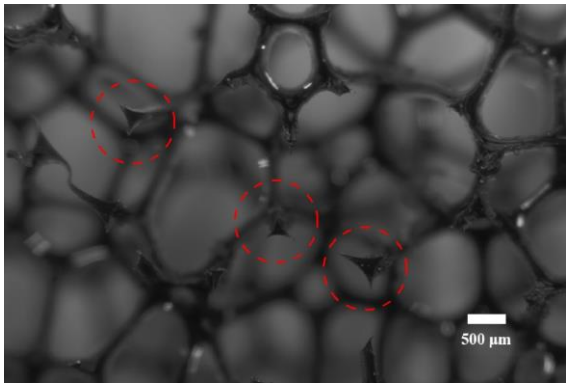

Figure 4-2. Image of the cross-section of a PU foam with 13 ppi.

Figure 4-3 displays the schematic diagram of the fabrication process. The slurries of cobalt oxide were prepared with distilled water, using a tornado stirrer (AS ONE SS-P1). The dispersant content was determined to be 0.2 wt.% of the solid loading of the slurry. The PU foams were immersed into the slurry at room temperature for 10 min. Afterwards, the loaded PU foams were squeezed to remove the excess slurry. Then the loaded PU foams were dried at 70 °C overnight. Finally, the green bodies were calcinated in an electric muffle furnace (ADVANTEC FUW232PB) under air atmosphere. The temperature progress consisted of three typical steps. A slow heating process was conducted from room temperature to 600 °C with a heating rate of 2 °C/min to remove the PU foam without damaging the framework of the solid coating. Then the temperature was increased to the given sintering temperature with a heating rate of 15 °C/min. Subsequently, the samples were calcinated at the given sintering temperature for several hours.

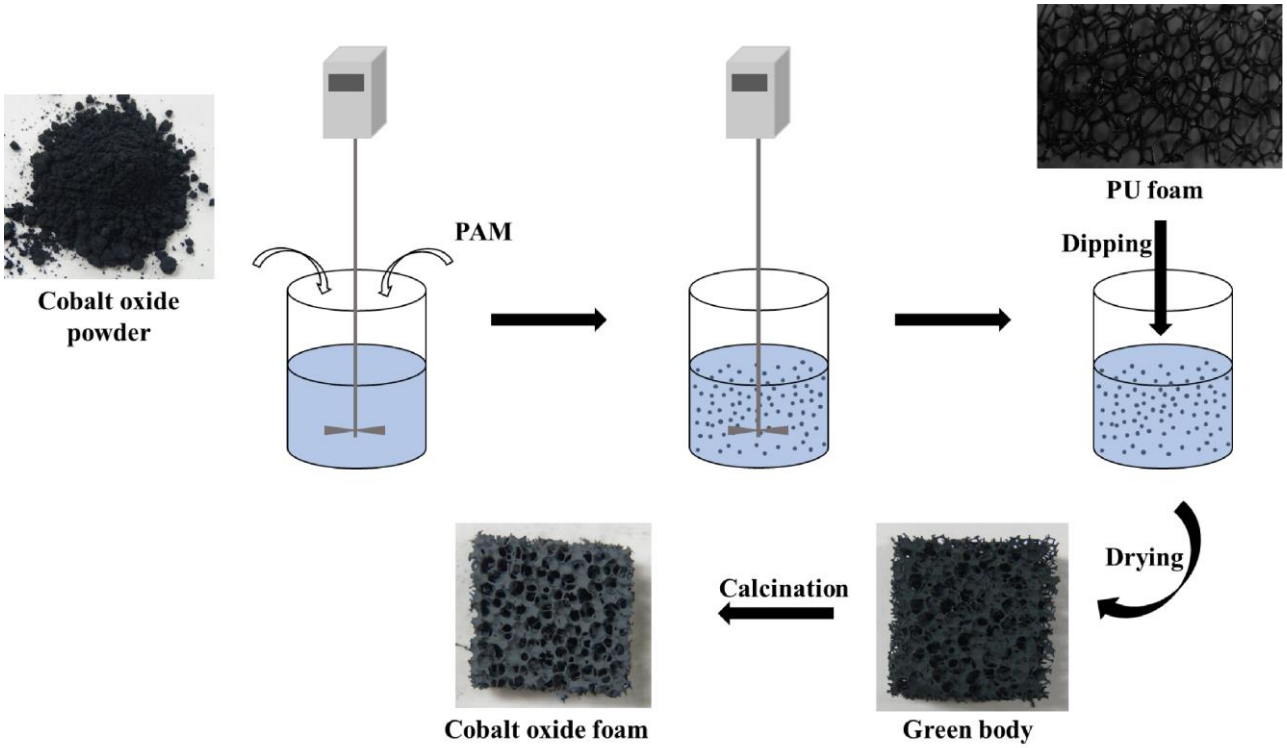

Figure 4-3. Fabrication process of cobalt oxide foams.

4.2.2 Characterization

The photographs of samples were taken using a digital camera (SONY HDR-PJ590V). A stereomicroscope (OLYMPUS SZX16), equipped with a microscope digital camera (OLYMPUS DP23) and a control unit (DP2-AOU), was used to appreciate the morphologies of the obtained foam-like structures. Additionally, the diameter of struts within the PU foams was measured using this setup. More than 200 struts were measured for each PU foam. A scanning electron microscope (SEM; JEOL JSM-7500FA) was utilized to observe the microscopic features of the cobalt oxide samples.

A vernier caliper was used to obtain the linear shrinkage of the foams caused by the thermal treatment process, by measuring the linear dimensions of the foams before and after the thermal treatment. The linear shrinkage, γ (%) is defined as,

$$\gamma = \left|\frac{D_f - D_i}{D_i}\right| \times 100 \quad (4\text{-}1)$$

where D_i is the initial linear measurement of the green body foam, and D_f is the finial linear measurement after the specified thermal treatment.

A thermogravimetric analyzer (TGA; HITACHI STA7300) was carried out to test the

reduction/re-oxidation repeatability behaviors of cobalt oxide. Typically, the temperature program for one reduction-oxidation cycle consisted of a heating step from 700 °C to 1000 °C with a dwell time of 5 min, followed by a cooling step from 1000 °C to 700 °C with a dwell time of 5 min. Each sample was tested at a heating/cooling rate of 10 °C/min under air atmosphere with a constant flow of 200 mL/min. In the reduction process, oxygen released, leading to a weight loss for the sample. In the re-oxidation process, oxygen uptake occurred, leading to a weight gain for the sample.

To observe the morphological evolutions of the larger-sized cobalt oxide foams after several reduction-oxidation cycles. An electric muffle furnace (ADVANTEC FUW232PB) under an air atmosphere was used. For the reduction process, the foams were heating from room temperature to 1000 °C at a rate of 10 °C/min and held at 1000 °C for 10 min. The subsequent re-oxidation process was performed through natural cooling. The bulk density, which is related to the thermal energy storage capacity of the cobalt oxide foam, can be calculated by the formula below:

$$\rho = \frac{weight\ of\ foam\ after\ calcination}{volume\ of\ foam\ after\ calcination} \quad (4\text{-}2)$$

Meanwhile, the porosity of the cobalt oxide foam can be calculated by the formula below:

$$P = 1 - \frac{weight\ of\ cobalt\ oxide\ /\ density\ of\ cobalt\ oxide}{volume\ of\ foam} \quad (4\text{-}3)$$

where the density of cobalt oxide is 6.11 g/cm^3 [141].

4.3 Results and discussion

4.3.1 Effect of the solid loading of cobalt oxide slurry

The solid loading of a slurry, which refers to the amount of solid in the slurry, can affect the effective coating of solid on PU foams. A high solid loading can increase the contact points between inter-particles for the green body. Meanwhile, a slurry with an appropriate viscosity can enhance the adhesion between particles and PU foams, while one with too high viscosity can affect the entering and filling processes of the slurry into PU foams, leading to non-uniform coating and even distorting the PU foams. In general, as the solid loading increases in a slurry, the viscosity also tends to increase [142]. Accordingly, to obtain a balance between the viscosity and effective coating, slurries with different solid loadings (ranging from 50 wt.% to 80 wt.%) were used to prepare cobalt oxide foams. It should be pointed out that the onset reduction temperature of the employed cobalt oxide

powder was ~ 925 °C. Thus, the sintering temperature of the green bodies was initially decided at 900 °C to avoid the phase change of cobalt oxide. All the green bodies were sintered at 900 °C for 5 hours. Additionally, each PU foam was cut into a dimension of 20 mm × 20 mm × 10 mm.

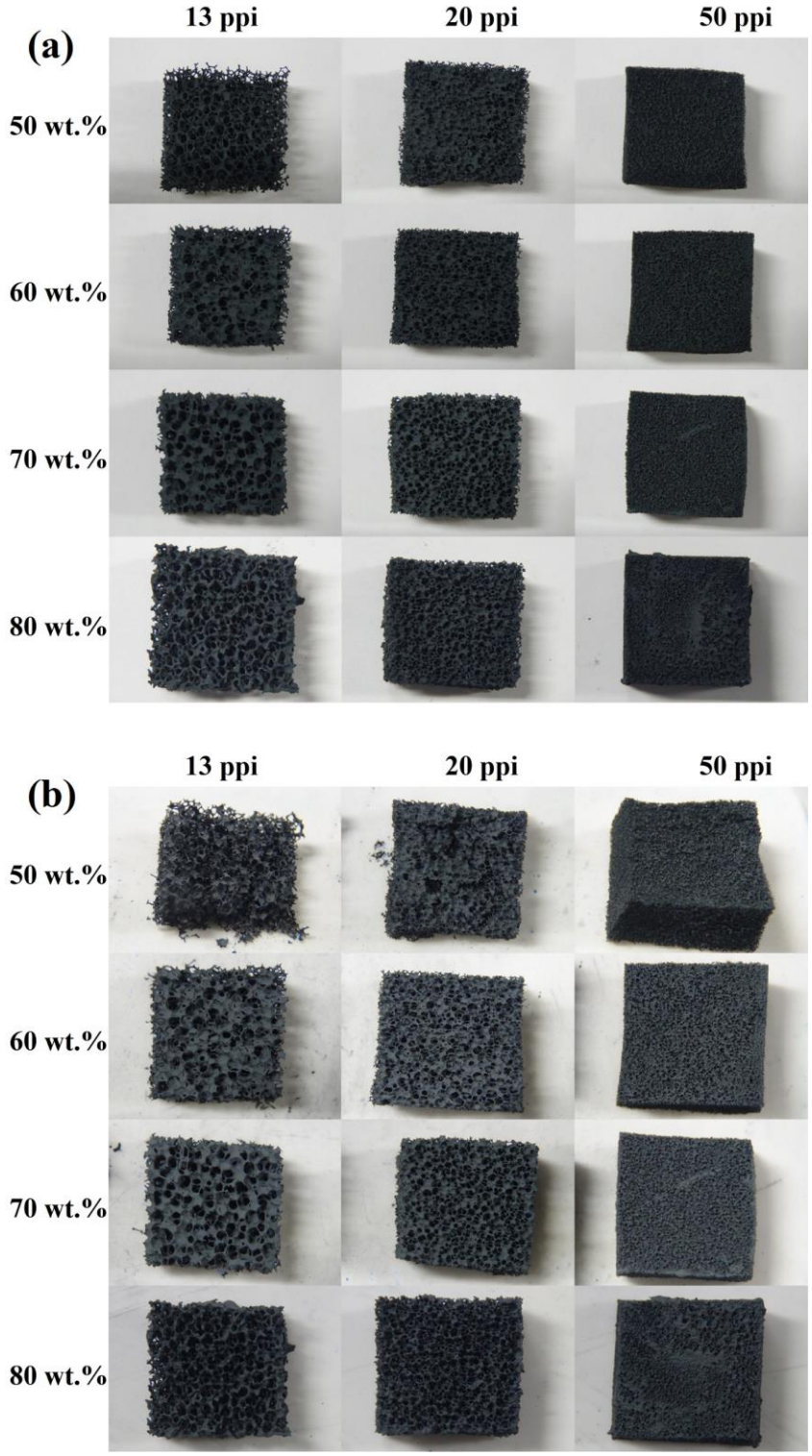

Figure 4-4. Photographs of (a) green bodies and (b) cobalt oxide foams fabricated with different solid loadings.

The photographs captured by a digital camera for the green bodies and the corresponding cobalt oxide foams fabricated with different solid loadings are shown in Figure 4-4. It is visible for all the green bodies that cobalt oxide particles were coated on the PU foams. However, for the green bodies prepared with a solid loading of 50 wt.%, the cobalt oxide foams fabricated using PU foams with different pore densities exhibited different degrees of collapse or subsidence after the given thermal treatment. Conversely, cobalt oxide powders were successfully shaped into form-like structures after the given thermal treatment for the samples using relatively high solid loadings.

More details can be observed from Figure 4-5 to Figure 4-8, taken by a stereomicroscope. It is evident that open cells with several closed faces existed within the green bodies. As shown in Figure 4-5, cobalt oxide solid did not spread evenly across the surfaces of PU foams for the green bodies prepared with the solid loading of 50 wt.%, resulting in the fracture of the struts that were supposed to interconnect the pores of the foams after the thermal treatment. For the foams prepared with a solid loading of 60 wt.%, cobalt oxide solid was evenly coated across the surface of the PU foams while the polygonal morphologies of the struts remained visible, as shown in Figure 4-6. This observation confirms that the solid coating has a small thickness. Consequently, when the employed PU foam possessed a relatively low pore density (i.e., 13 ppi), a considerable number of visible cracks and fractures can be observed in the struts from the obtained cobalt oxide foam. Whereas, the cobalt oxide foams using PU foams with 20 ppi and 50 ppi presented quite uniform morphologies after the thermal treatment. Upon increasing the solid loading to 70 wt.%, the green bodies prepared using PU foams with13 ppi and 20 ppi exhibited relatively thick coatings. After the thermal treatment, the resulting cobalt oxide foams presented smoother surfaces and textures. However, as shown in Figure 4-4b, the cobalt oxide foam prepared using a PU foam with a relatively high pore density (i.e., 50 ppi) showed a visibly uneven distribution of cobalt oxide, with cobalt oxide solid stacking within the foam. When the solid loading increased to 80 wt.%, non-uniform morphologies were observed in the green bodies. Some of the struts of the 13 ppi and 20 ppi PU foams were thickly coated by cobalt oxide solid, while other parts of the struts remained exposed.

After the thermal treatment, a significant number of visible cracks were observed in the struts of the cobalt oxide foams fabricated using PU foams with 13 ppi and 20 ppi. Additionally, as shown in Figure 4-4 and Figure 4-8, a large amount of cobalt oxide solid stacked within the foam using a 50 ppi PU foam.

In brief, the solid loading of cobalt oxide slurry can affect the coating uniformity and thickness within PU foams, which ultimately affects the formation of struts within cobalt oxide foams. Meanwhile, it is important to consider the pore density within a PU foam when selecting a suitable solid loading. In this case, 60 wt.% of solid loading was suitable for the evenly coating of cobalt oxide solid on a 50 ppi PU foam, while 70 wt.% of solid loading was beneficial for the preparation of cobalt oxide foams using PU foams with 20 ppi and 13 ppi.

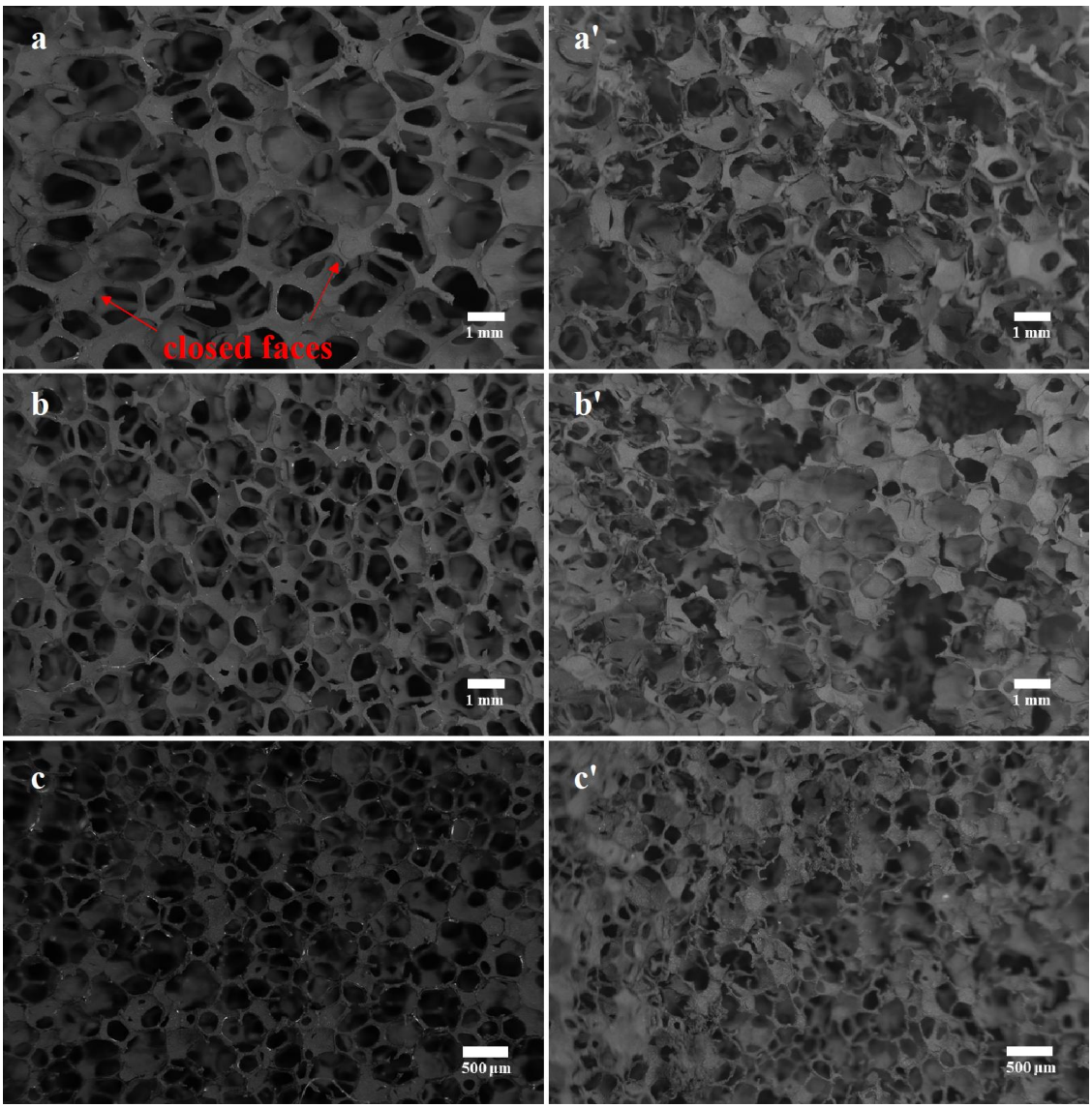

Figure 4-5. Images of foam structures prepared with a solid loading of 50 wt.%: (a) green body using a 13 ppi PU foam, (a') cobalt oxide foam fabricated with a 13 ppi PU foam, (b) green body using a 20 ppi PU foam, (b') cobalt oxide foam fabricated with a 20 ppi PU foam, (c) green body using a 50 ppi PU foam, and (c') cobalt oxide foam fabricated with a 50 ppi PU foam.

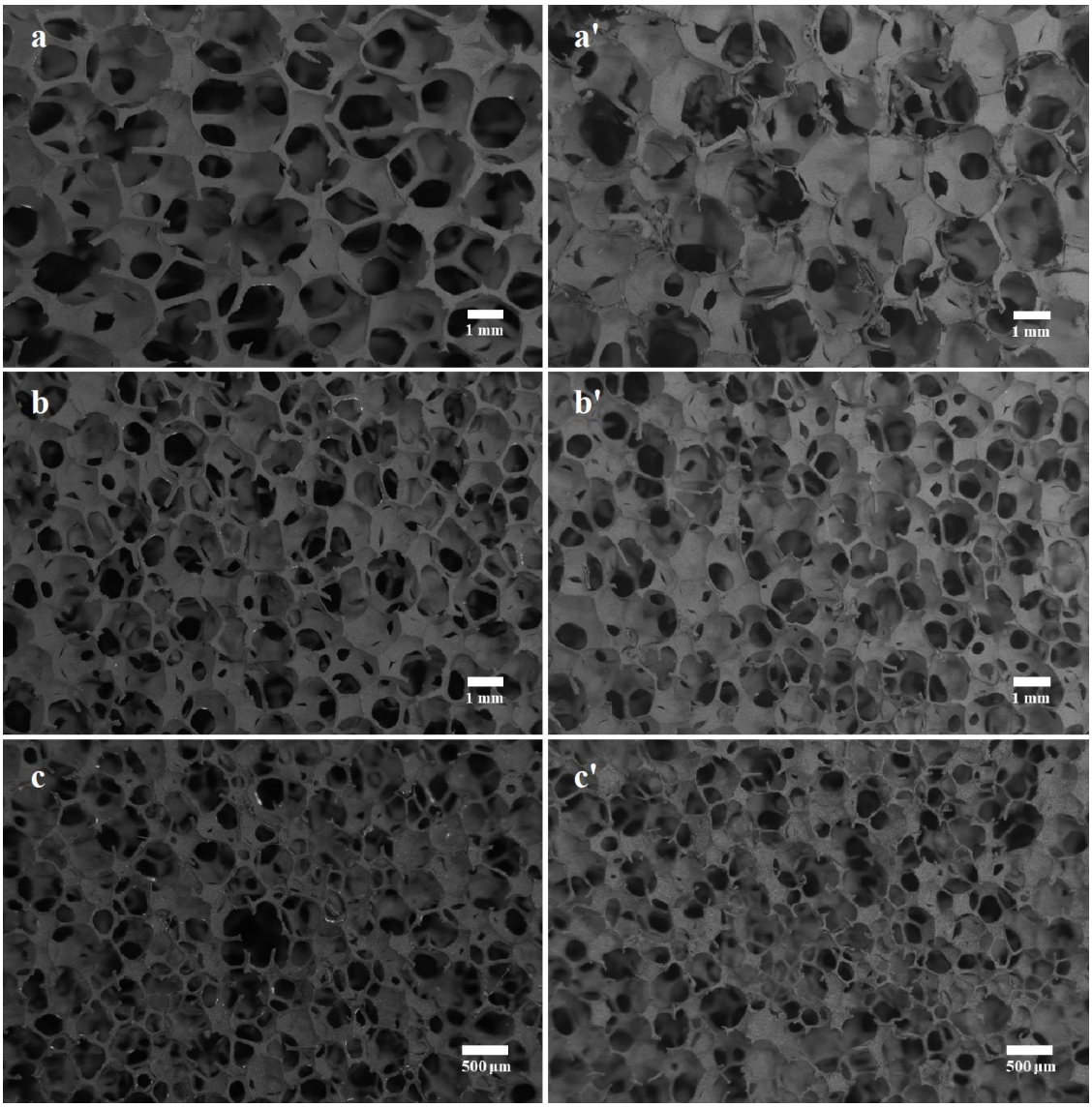

Figure 4-6. Images of foam structures prepared with a solid loading of 60 wt.%: (a) green body using a 13 ppi PU foam, (a') cobalt oxide foam fabricated with a 13 ppi PU foam, (b) green body using a 20 ppi PU foam, (b') cobalt oxide foam fabricated with a 20 ppi PU foam, (c) green body using a 50 ppi PU foam, and (c') cobalt oxide foam fabricated with a 50 ppi PU foam.

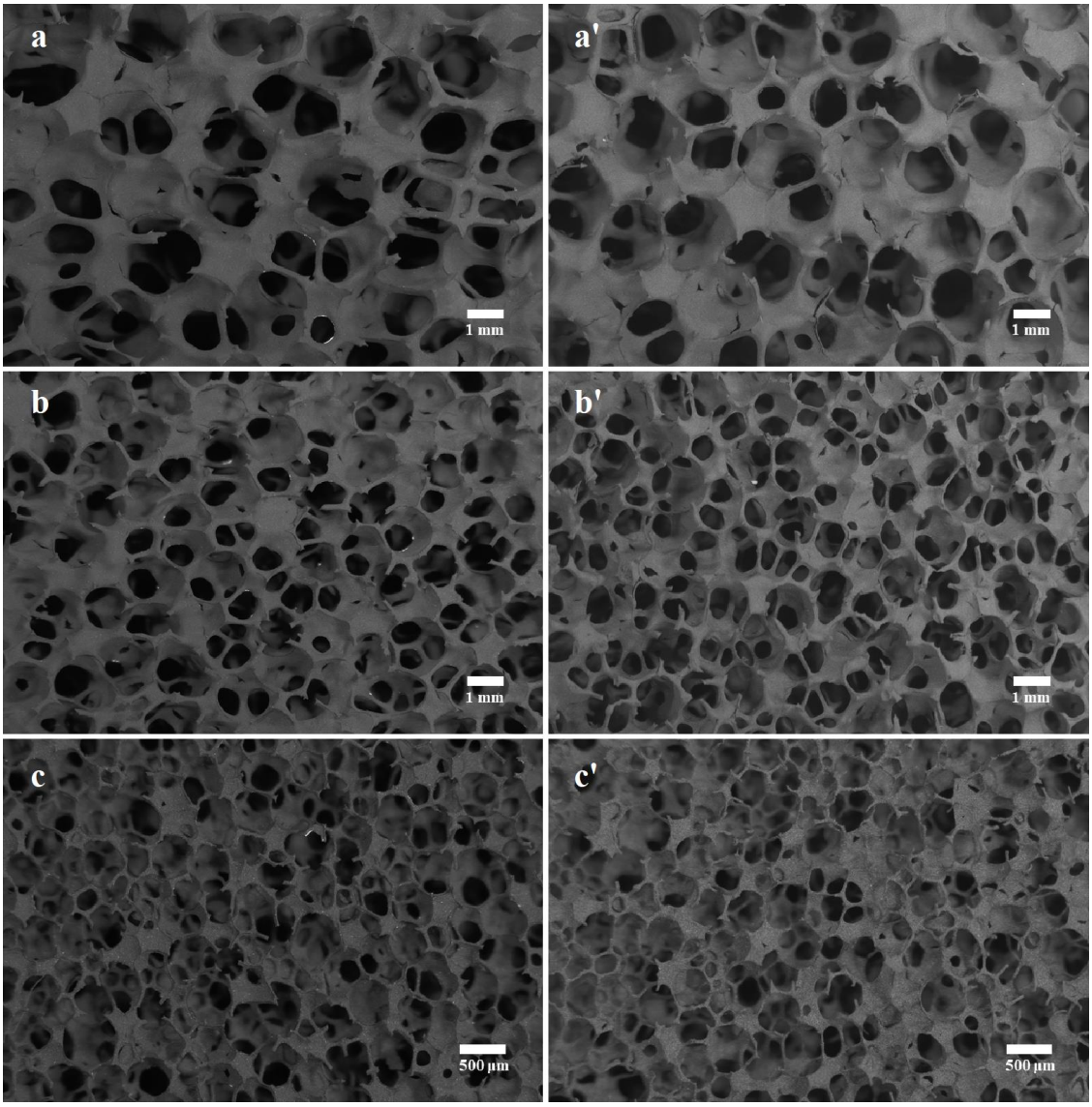

Figure 4-7. Images of foam structures prepared with a solid loading of 70 wt.%: (a) green body using a 13 ppi PU foam, (a') cobalt oxide foam fabricated with a 13 ppi PU foam, (b) green body using a 20 ppi PU foam, (b') cobalt oxide foam fabricated with a 20 ppi PU foam, (c) green body using a 50 ppi PU foam, and (c') cobalt oxide foam fabricated with a 50 ppi PU foam.

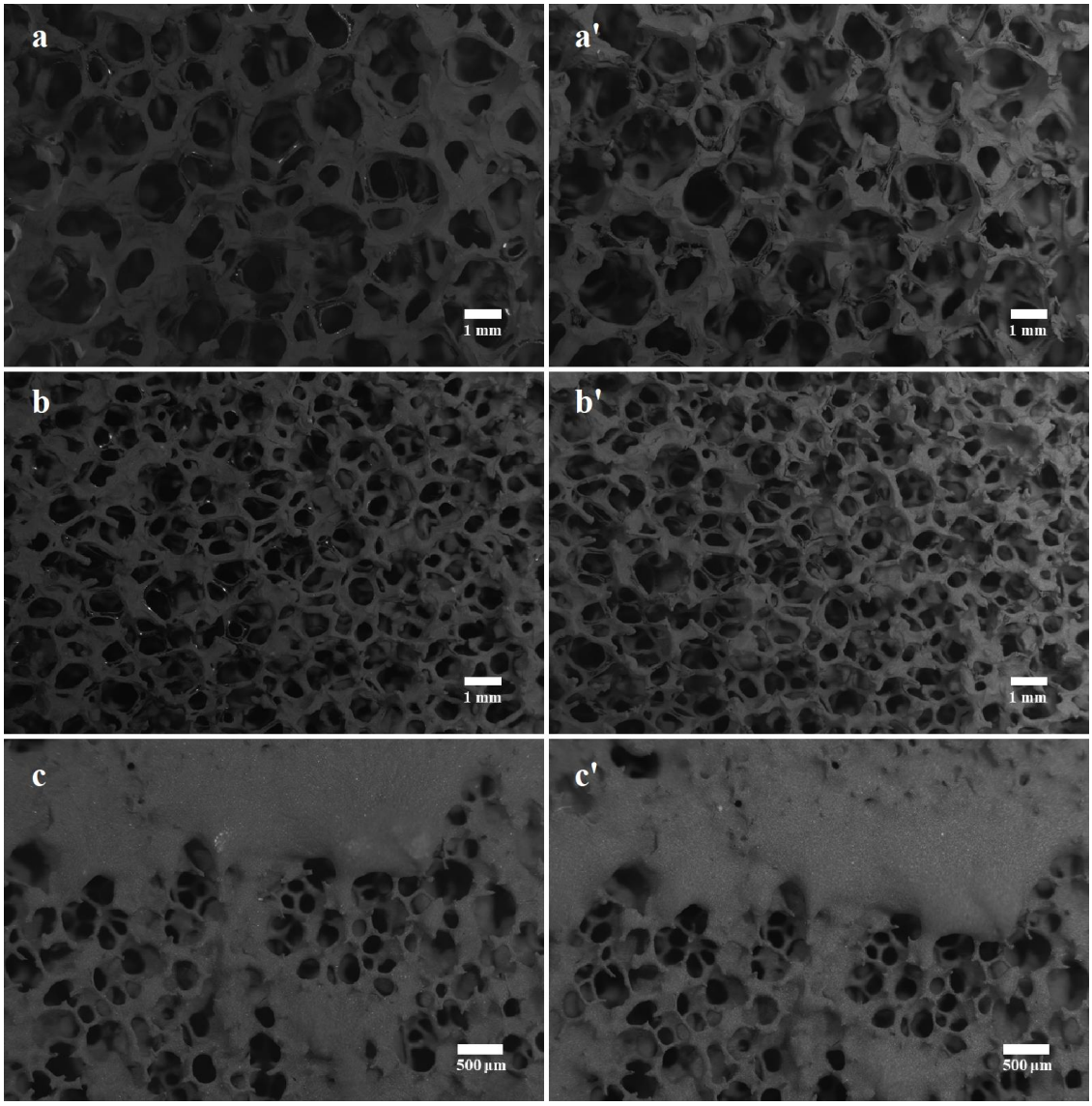

Figure 4-8. Images of foam structures prepared with a solid loading of 80 wt.%: (a) green body using a 13 ppi PU foam, (a') cobalt oxide foam fabricated with a 13 ppi PU foam, (b) green body using a 20 ppi PU foam, (b') cobalt oxide foam fabricated with a 20 ppi PU foam, (c) green body using a 50 ppi PU foam, and (c') cobalt oxide foam fabricated with a 50 ppi PU foam.

4.3.2 Effect of sintering temperature and sintering duration

As discussed in the previous chapters, cobalt oxide particles can undergo a sintering process in high temperature range, which may ultimately affect the properties of cobalt oxide foams. During the sintering process, the particles in the green body will diffuse and bond with the inter-particles along with densification and coarsening phenomena.

Therefore, a suitable sintering condition including sintering temperature and sintering duration should be determined for the preparation of the cobalt oxide foams. In this study, the sintering temperatures before and after the phase change of cobalt oxide were selected for investigating the effect of the sintering temperature on the formation of cobalt oxide foams. Each PU foam was cut into a dimension of 20 mm × 20 mm × 10 mm. The cobalt oxide slurry was prepared with a solid loading of 70 wt.%.

Figure 4-9 shows the photographs of cobalt oxide foams fabricated with different sintering temperatures. In addition, all the green bodies were sintered at the given temperature for 5 hours. Foam-like structures were obtained for all the samples after the specified thermal treatments. The linear shrinkage of the foams was calculated by eq. (4-1). As shown in Figure 4-10, all the samples presented similar degree of shrinkage when the sintering temperature was 800 °C. The cobalt oxide foams shrunk to a greater degree as the sintering temperature increased, indicating a higher degree of sintering. For instance, in the case of the cobalt oxide foams prepared with 20 ppi PU foams, around 2% of shrinkage occurred for the foam fabricated with the sintering temperature of 800 °C, while approximately 9.2% of shrinkage presented in the foam sintered at 1100 °C. The relevant SEM images for the foams were displayed in Figure 4-11. For the foam calcined at 800 °C, the individual cobalt oxide particles were still visible, indicating that the particles had not yet fused together completely. While when the sintering temperature was 900 °C, necks formed between inter-particles due to the sintering process. A coral-like structure with open pores among the bulk was observed, demonstrating that the cobalt oxide foam presented a dual-scale porosity. Similar morphologies with coral-like structures were observed in the foams that were sintered at 1000 °C and 1100 °C. Furthermore, as the sintering temperature increased, the necks became wider, and many neighboring particles fused together to form a relatively large bulk. This fusion also led to the elimination of voids among these particles, thereby contributing to a greater degree of shrinkage.

It is interesting to note that, in the case of the cobalt oxide foams fabricated with the sintering temperature of 1100 °C, the cobalt oxide foam using a PU foam with relatively thin struts presented a greater degree of shrinkage, which may correspond to a denser morphology within the foam. Approximately 8.7%, 9.2%, and 11.2% of shrinkage occurred in the foams fabricated using PU foams with13 ppi, 20 ppi, and 50 ppi,

respectively.

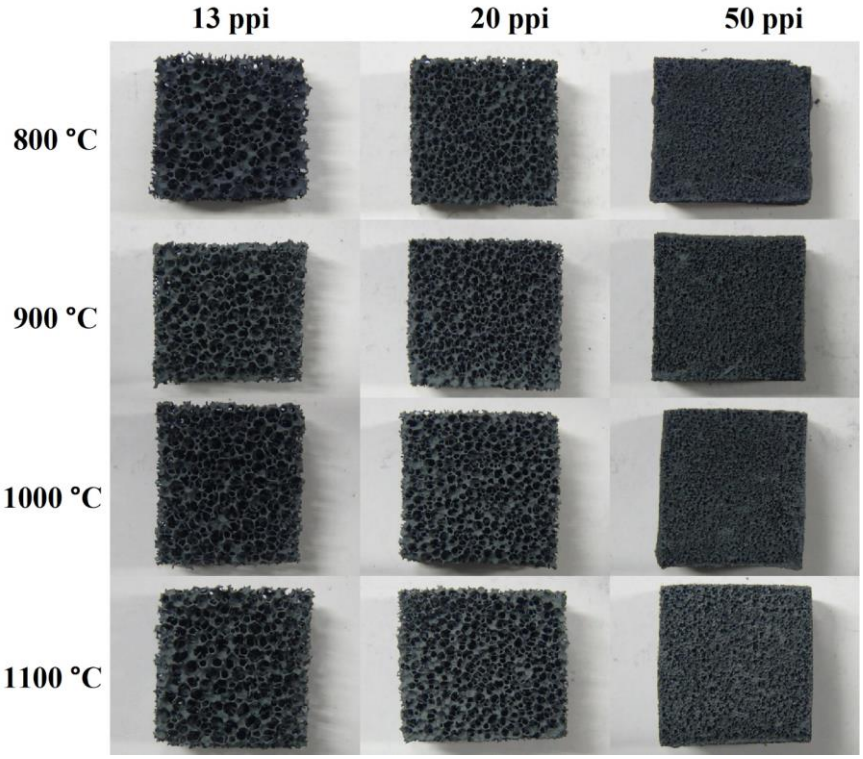

Figure 4-9. Photographs of cobalt oxide foams fabricated using different sintering temperatures.

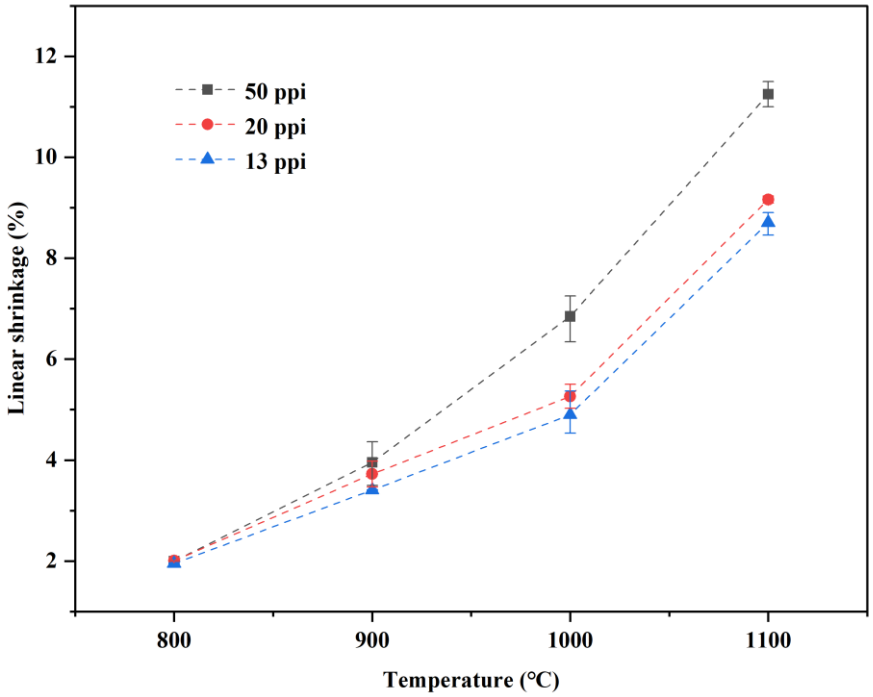

Figure 4-10. Linear shrinkage against sintering temperature for cobalt oxide foams fabricated using PU foams with different pore densities.

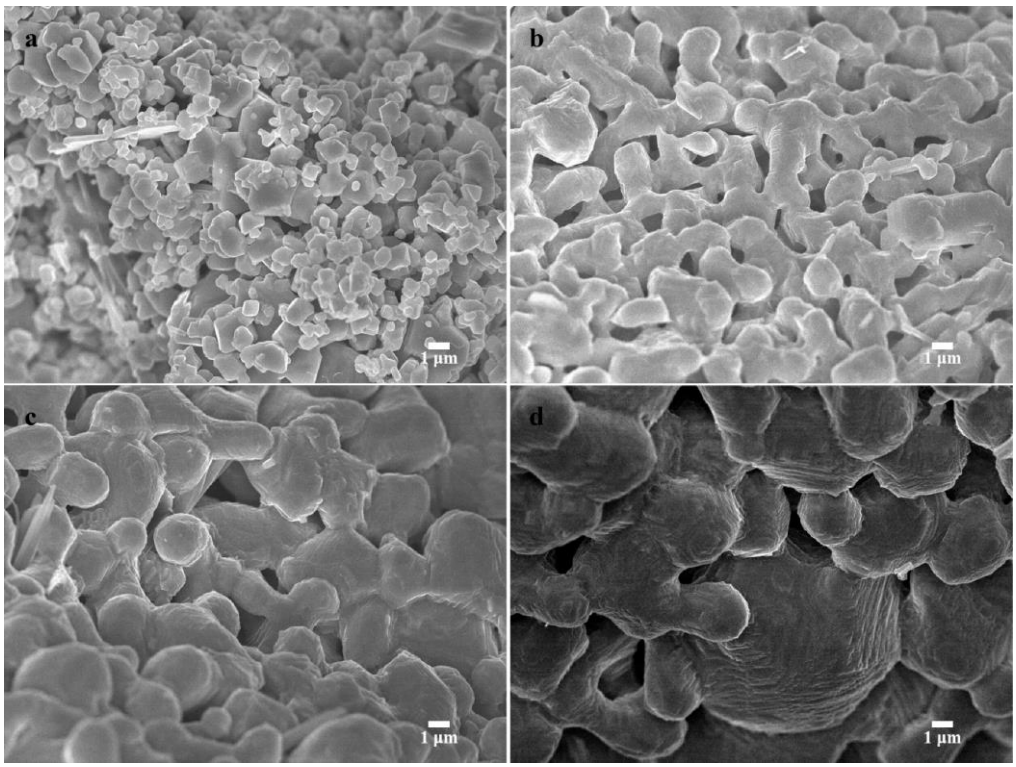

Figure 4-11. SEM images of cobalt oxide foams (using 20 ppi PU foams) fabricated using different sintering temperatures: (a) 800 °C, (b) 900 °C, (c) 1000 °C, and (d) 1100 °C.

As discussed in the previous chapters, the morphology of cobalt oxide highly affected the re-oxidation kineties. Accordingly, cobalt oxide foams fabricated with different sintering temperatures were cut into smaller dimensions for analysis using TGA to confirm the redox repeatability behaviors. As illustrated in Figure 4-12, the samples exhibited stable repeatability behaviors over 10 reduction-oxidation cycles when the sintering temperatures were 800 °C and 900 °C. Each cycle exhibited a weight change of 6.5 % (the stoichiometric value: 6.64%). The increased weights observed in the first heating step for the samples calcined at 1000 °C were attributed to the oxidation of CoO, which was produced by the reduction of Co_3O_4 in the sintering treatment and was not fully re-oxidized in the natural cooling. The subsequent reduction in the first heating step resulted in a weight loss of 6.0%, indicating that the initial oxidation was incomplete. However, a consistent weight loss of 6.5% was achieved in the subsequent cycles. In the case of the samples calcined at 1100 °C, the weight loss in the first heating step was lower than 6.5% for each sample and increased from cycle to cycle. Additionally, the sample fabricated using a PU foam with thinner struts exhibited a relatively low weight loss in the first heat step, which is consistent with the result shown in Figure 4-10. The relatively low weight loss may be attributed to the denser morphology within the sample, which could hinder the diffusion of oxygen, leading to a higher degree of incomplete oxidation in the natural cooling process.

Further, the impact of sintering duration on the preparation of cobalt oxide foams was also studied. Figure 4-13 shows the SEM images of cobalt oxide foams sintered at 900 °C for varying durations. When the samples sintered at 900 °C for a duration of 3 hours or less, individual cobalt oxide particles with distinct particle boundaries remained visible. When the sintering duration increased to 4 hours, typical sintering behaviors became evident, including the formation of necks between particles, smoothing of particle boundaries, and coarsening.

Overall, the results demonstrate the significance of sintering conditions for carefully controlling the sintering process of cobalt oxide particles to achieve a desired foam-like

structure and a stable redox repeatability performance for TCS applications. If the sintering temperature is too low, cobalt oxide particles may not bond adequately. This can result in a less compact and less interconnected structure. On the other hand, if the sintering temperature is too high, over-sintering can occur, leading to excessive densification which may hinder the oxygen diffusion during the oxidation of cobalt oxide. Additionally, the sintering duration should also be long enough to ensure a complete sintering process.

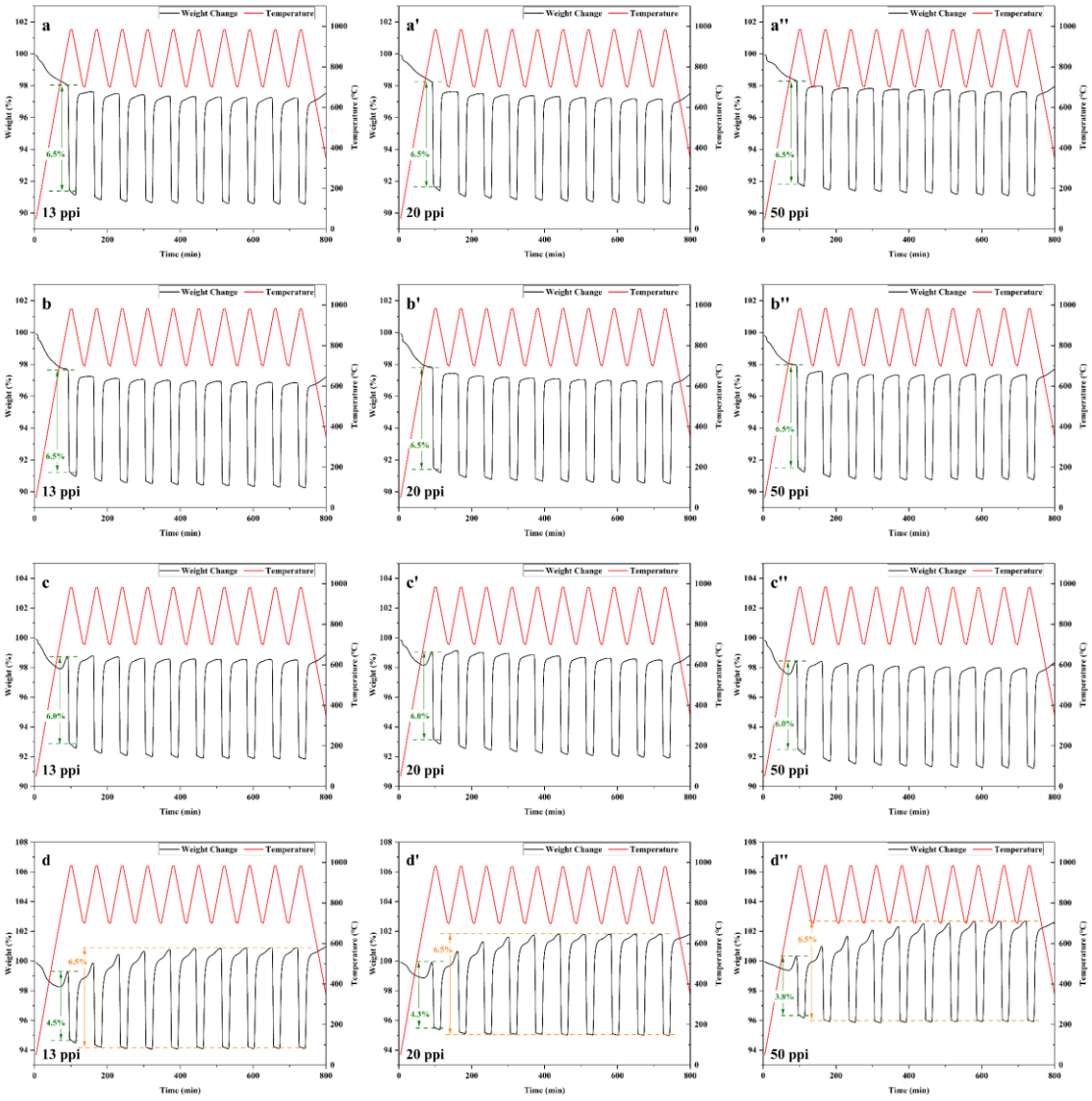

Figure 4-12. TGA curves of cobalt oxide foams fabricated with different sintering temperatures: (a), (a'), and (a'') sintered at 800 °C; (b), (b'), and (b'') sintered at 900 °C; (c), (c'), and (c'') sintered at 1000 °C; (d), (d'), and d'') sintered at 1100 °C.

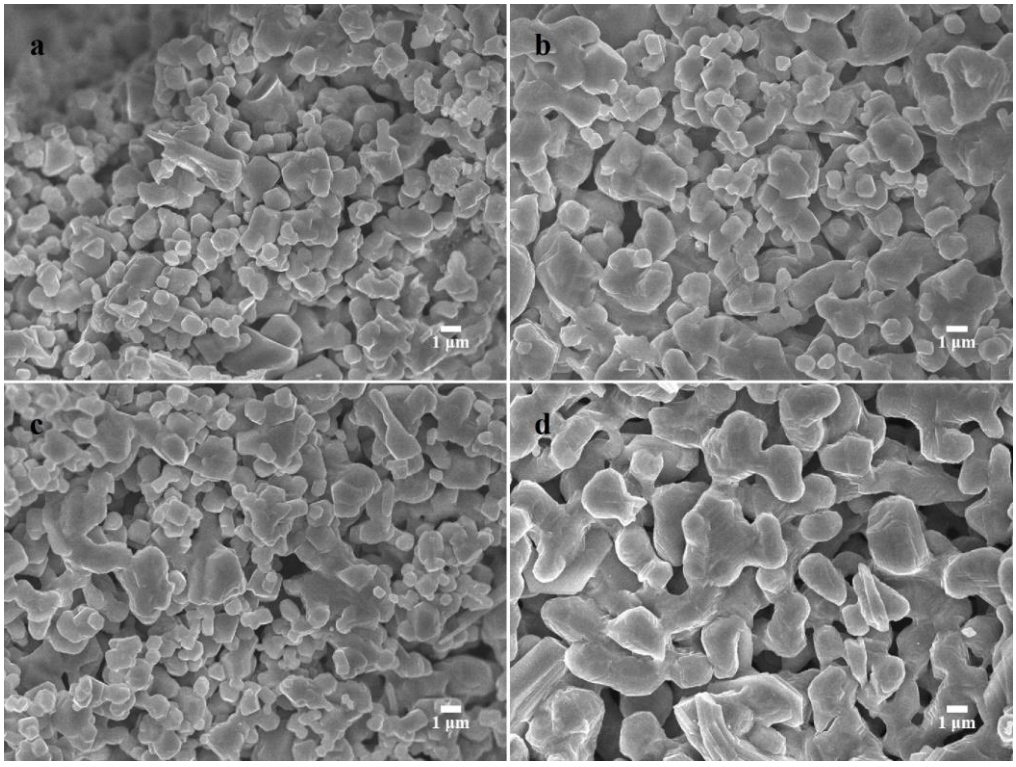

Figure 4-13. SEM images of cobalt oxide foams (using 20 ppi PU foams) sintered at 900 °C for varying durations: (a) 1 hour, (b) 2 hours, (c) 3 hours, and (d) 4 hours.

4.3.3 Structural evolutions of cobalt oxide foams during thermal cycling

As the stability and durability of cobalt oxide foams for TCS application are important, cobalt oxide foams prepared with the solid loadings of 60 wt.% and 70 wt.% were subjected to several heating-cooling cycles for observing their structural evolutions. The heating-cooling cycles were performed by an electric muffle furnace under an air atmosphere. Figure 4-14 and 4-15 display the morphologies of the cobalt oxide foams after several heating-cooling cycles. After one heating-cooling treatment, there were no significant changes observed in the morphologies of all the cobalt oxide foams (compared with Figure 4-6 and Figure 4-7). Meanwhile, the cracks formed during the preparation process remained visible. After 10 heating-cooling cycles, varying degrees of struts distortion were observed in the foams. In the case of the cobalt oxide foams fabricated with a solid loading of 60 wt.%, the distortion of the struts was evident for the foams fabricated using PU foams with 50 ppi and 20 ppi, even leading to the fracture of the struts for the foam fabricated using a 50 ppi PU foam. When it comes to the cobalt oxide

foams fabricated with a solid loading of 70 wt.%, as shown in Figure 4-15, similar phenomena presented in the foams fabricated using PU foams with 50 ppi and 20 ppi. Whereas, a relatively minor distortion of the struts was observed in the cobalt oxide foam fabricated with a 13 ppi PU foam. Figure 4-16 shows the SEM images of the cobalt oxide foam before and after several heating-cooling cycles. The voids among the cobalt oxide bulk became larger after 10 heating-cooling cycles, indicating that the cobalt oxide foam underwent continuous sintering during the heating-cooling cycles. This continuous sintering could lead to expansion and contraction of the struts, which could potentially affect the stability and durability of the cobalt oxide foams. Another possible factor that may have contributed to the distortion of the struts is the unbalanced thermal stress produced by a non-uniform temperature distribution [143]. In order to achieve a clear observation, larger-sized cobalt oxide foams were fabricated by cutting PU foams with pore densities of 50 ppi, 20 ppi and 13 ppi into blocks with dimensions of 100 mm × 80 mm × 10 mm. The green bodies were prepared with a solid loading of 70 wt.% and sintered at 900 °C for 5h. As shown in Figure 4-17, the cobalt oxide foams fabricated using PU foams with pore densities of 50 ppi and 20 ppi presented evident deformation in their structural geometry after the 10 cycles. In fact, the foam produced from a 50 ppi PU foam experienced significant cracking. Conversely, the cobalt oxide foam fabricated with a 13 ppi PU foam maintained relatively flat surfaces. It is worth noting that struts with a relatively large diameter appeared to be effective in resisting distortion. Furthermore, the presence of larger pores within the foam might be conducive to the flow of air, resulting in more effective heat transfer.

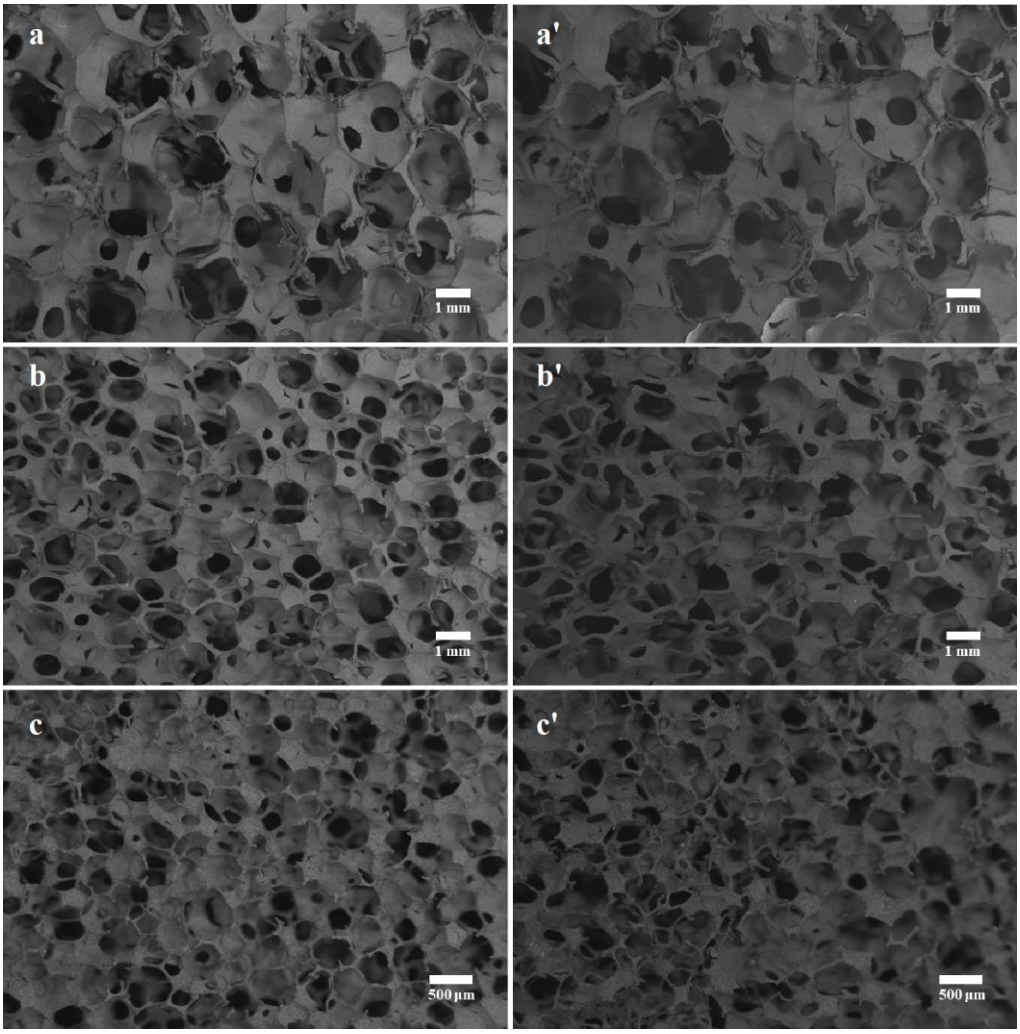

Figure 4-14. Images of cobalt oxide foams prepared with a solid loading of 60 wt.%: (a) using a 13 ppi PU foam and being subjected to one heating-cooling cycle, (a') using a 13 ppi PU foam and being subjected to 10 heating-cooling cycles, (b) using a 20 ppi PU foam and being subjected to one heating-cooling cycle, (b') using a 20 ppi PU foam and being subjected to 10 heating-cooling cycles, (c) using a 50 ppi PU foam and being subjected to one heating-cooling cycle, and (c') using a 50 ppi PU foam and being subjected to 10 heating-cooling cycles.

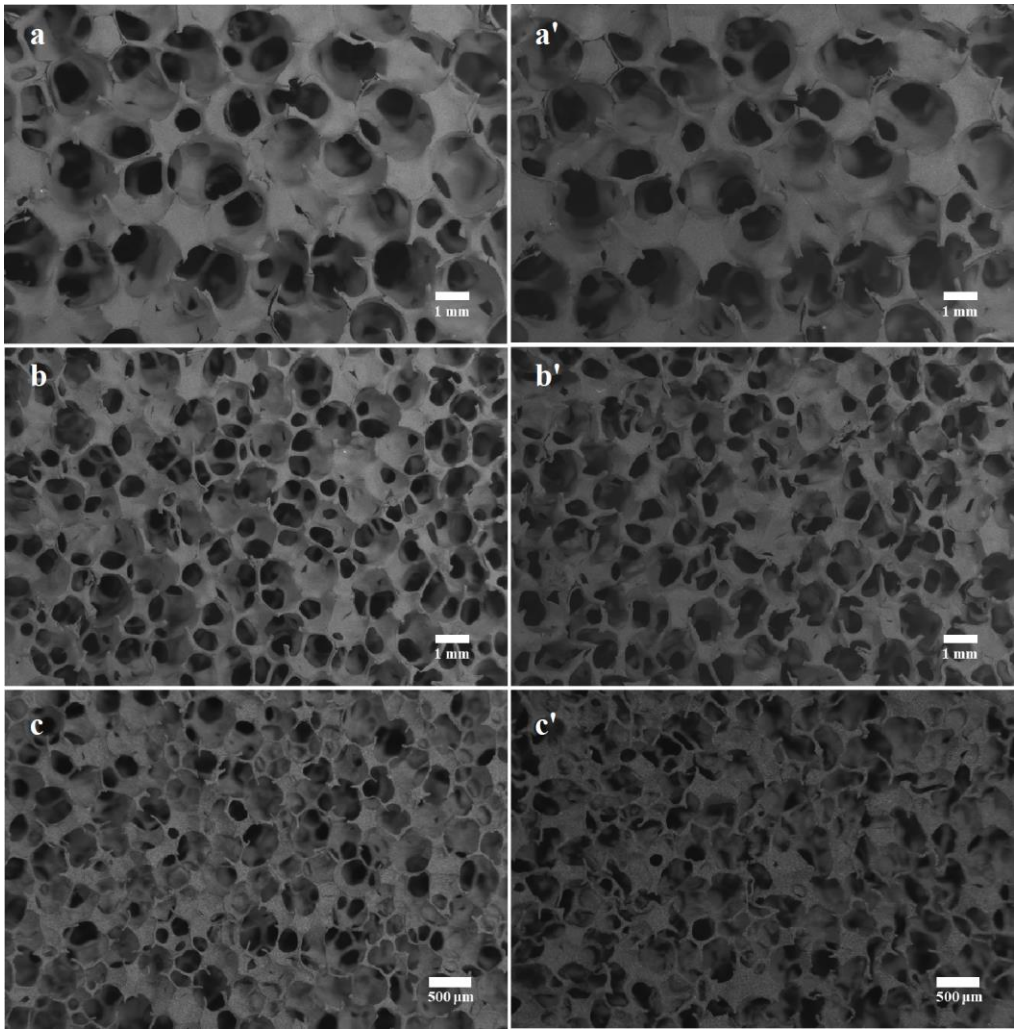

Figure 4-15. Images of cobalt oxide foams prepared with a solid loading of 70 wt.%: (a) using a 13 ppi PU foam and being subjected to one heating-cooling cycle, (a') using a 13 ppi PU foam and being subjected to 10 heating-cooling cycles, (b) using a 20 ppi PU foam and being subjected to one heating-cooling cycle, (b') using a 20 ppi PU foam and being subjected to 10 heating-cooling cycles, (c) using a 50 ppi PU foam and being subjected to one heating-cooling cycle, and (c') using a 50 ppi PU foam and being subjected to 10 heating-cooling cycles.

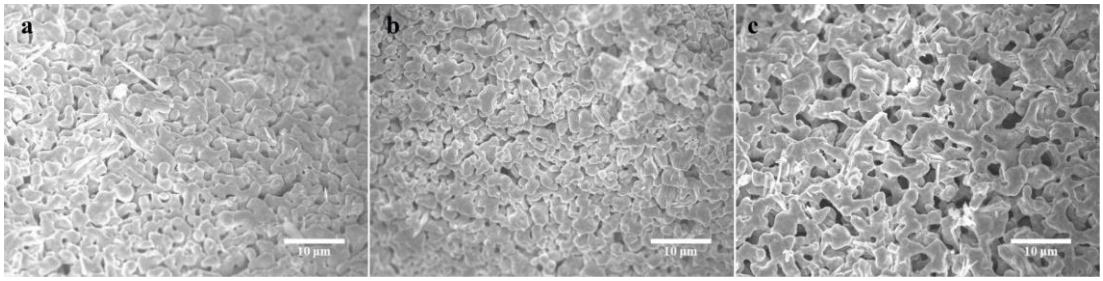

Figure 4-16. SEM images of a cobalt oxide foam fabricated with a solid loading of 70 wt.% using a 20 ppi PU foam: (a) as-prepared sample, (b) after one heating-cooling cycle, and (c) after 10 heating-cooling cycles.

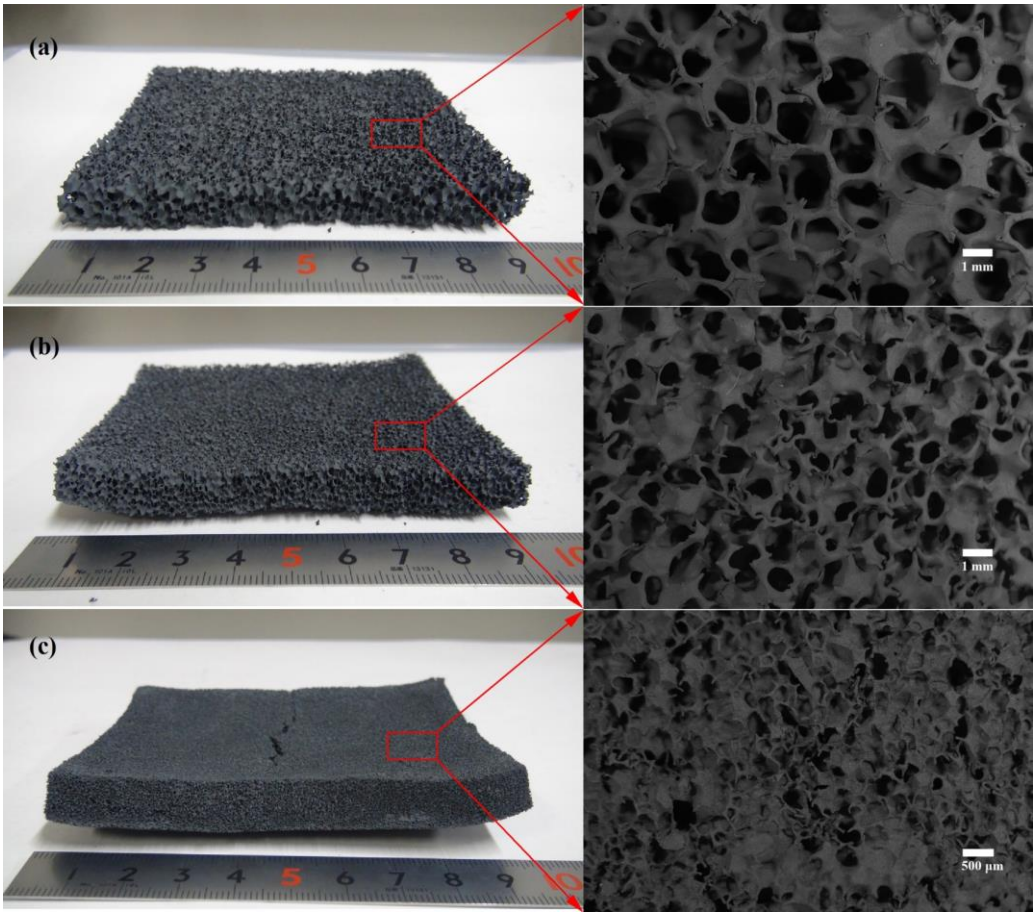

Figure 4-17. Images taken after 10 heating-cooling cycles for cobalt oxide foams fabricated with a solid loading of 70 wt.%: (a) using a 13 ppi PU foam, (b) using a 20 ppi PU foam, and (c) using a 50 ppi PU foam.

4.3.4 Fabrication of cobalt oxide foams with a consecutive immersion approach

The cobalt oxide foam fabricated using a 13 ppi PU foam demonstrated relatively stable

structural durability, making it suitable for long-term TCS applications. However, there were visible cracks observed in the foams, as described above. Herein, a consecutive immersion approach, which is an alternative method to increase the thickness of struts within ceramic foams [144], was employed to improve the solid coating of the cobalt oxide foam. In this case, a solid loading of 70 wt.% was used for the first immersion, and the dried green body was calcined at 800 °C for 3 hours. Afterwards, the obtained foam was re-immersed using a cobalt oxide slurry with a relatively low solid loading and then dried at 110 °C. This re-immersion process can be repeated several times. Finally, the foam was calcined at 900 °C for 5 hours. As shown in Figure 4-18, cracks were evident within the cobalt oxide foam fabricated with just one immersion. Similar morphology can be also observed in Figure 4-7 (a') that were calcined at 900 °C for 5 hours. However, after three additional consecutive immersions, it becomes apparent that the cracks were improved or eliminated due to the filling of cobalt oxide solid. Moreover, with the increasing number of re-immersions, the loading amount of cobalt oxide increased, as shown in Figure 4-19. The bulk density, calculated using eq. (4-2), increased from approximately 0.39 g/cm^3 for the cobalt oxide before the re-immersion approach to 0.78 g/cm^3 for the foam with three additional re-immersions. Theoretically, the thermal energy storage density for the cobalt oxide foam fabricated using a 13 ppi PU foam could be approximately 658.32 kJ/L, and the corresponding porosity was 87%.

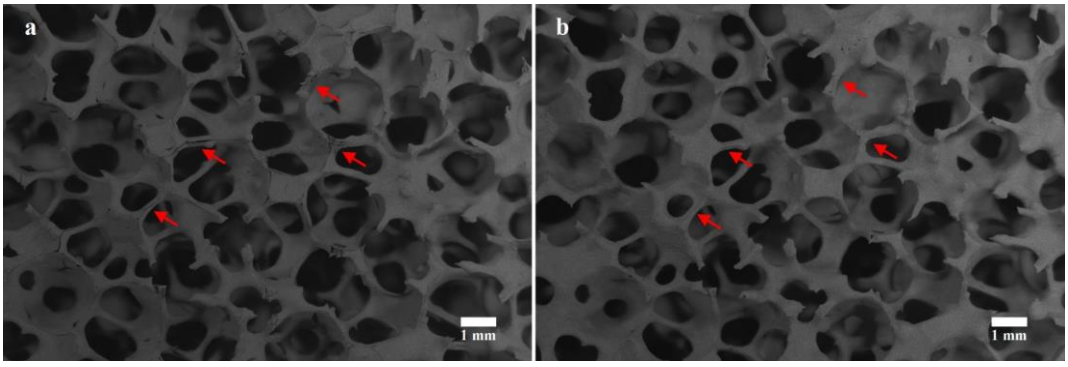

Figure 4-18. Images of a cobalt oxide foam using a 13 ppi PU foam: (a) fabricated before a consecutive immersion approach and (b) fabricated with three additional consecutive immersions.

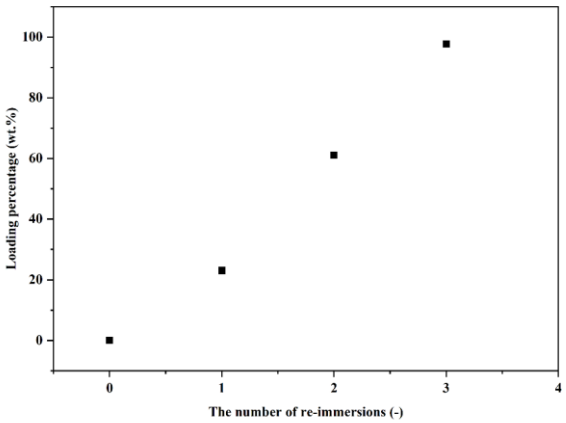

Figure 4-19. Loading percentage against the number of re-immersions.

4.4 Summary

In this study, cobalt oxide foams were prepared by means of a foam replica method which involves using inexpensive PU foams as the templates for use in TCS applications. Valuable information and a consecutive immersion approach for preparing cobalt oxide foams were provided. The major conclusions are summarized below.

(1) The solid loading of the cobalt oxide slurry could impact the structure of cobalt oxide foams by affecting the coating uniformity and thickness within the PU foams. Moreover, the pore density of employed PU foams should also be considered as a factor for selecting a suitable solid loading.

(2) Careful control of sintering conditions, including sintering temperature and sintering duration, was crucial in achieving the desired foam-like structure and stable redox repeatability performance for TCS applications. Relatively low sintering temperatures or short sintering durations could result in insufficient sintering, leading to a less compact and less interconnected structure. It should also be noted that excessively high sintering temperatures could cause over-sintering of cobalt oxide, resulting in a dense morphology with few voids that may impede oxygen diffusion.

(3) The cobalt oxide foams exhibited continuous structural evolutions during their reduction-oxidation cycles. The struts with a relatively large diameter within a PU foam appeared to be conducive to resisting the foam distortion.

(4) The utilization of a consecutive immersion approach in the preparation of cobalt

oxide foams could repair cracks within the foams and increase their thermal storage densities.

Chapter 5. Conclusions and future works

5.1 Conclusions

In this study, cobalt oxide-based redox systems for use in thermochemical energy storage (TCS) were experimentally investigated, including the development of efficient cobalt oxide-based materials and exploration of porous cobalt oxide for application in reactor concepts. The main conclusions are summarized below.

In chapter 2, to deeply understand the behavior of Cu-doped cobalt oxide-based redox system for TCS and improve its repeatability performance, CuO-doped cobalt oxide composites were proposed and investigated. The effects of CuO doping on the redox behavior and repeatability performance of cobalt oxide were explored. Doping with CuO significantly decreased the onset temperature of reduction by 60 °C compared to pure cobalt oxide. The result verifies that the onset temperature of re-oxidation could be tuned in the range from 825 °C to 890 °C by altering the doping amount of CuO. The results collected from in-situ XRD demonstrate that CuO was involved in the reduction/re-oxidation process of cobalt oxide. Cu species doped in the cobalt oxide structure during the reduction process and separated out during the re-oxidation process. Meanwhile, the repeatability performance of CuO-doped cobalt oxide composites was highly affected by the doping amount of CuO. Deterioration in the repeatability performance was observed with the increase of CuO doping amount. However, CuO with relatively small particle size exhibited a positive effect on improving the repeatability of CuO-doped cobalt oxide composites. Hence, doping CuO in cobalt oxide by a mechanical mixing process is a feasible approach to enhance the repeatability performance of Cu-doped cobalt oxide-based redox system. CuO-doped cobalt oxide composite is a promising candidate for storing thermal energy in a lower temperature range.

In chapter 3, to develop suitable materials and increase more applicability of cobalt oxide-based TCS systems, the potential of $LiCoO_2$-doped cobalt oxide composites for use in TCS applications was studied. Doping with $LiCoO_2$ diminished the onset temperature of reduction and re-oxidation by 50 °C and 65 °C, respectively. Doping with an appropriate amount of $LiCoO_2$ contributed to improving the re-oxidation rate of cobalt oxide-based system under a high cooling rate, resulting in a significant increase in the discharging heat

(423.8 kJ/kg) compared to pure cobalt oxide (289.8 kJ/kg) under a temperature cooling rate of 20 °C/min. Doping with $LiCoO_2$ was found to decrease the apparent activation energy of reduction and oxidation of cobalt oxide. Also, in-situ XRD results confirmed that $LiCoO_2$ was involved in the reduction/re-oxidation process of cobalt oxide. The insertion amount of Li species on cobalt oxide appeared to relate to the onset temperature of re-oxidation. Additionally, the excellent repeatability performance of this composite was attested in 50 cycles. Thus, $LiCoO_2$-doped cobalt oxide composite is a promising alternative for TCS applications operated in a relatively low temperature range.

In chapter 4, cobalt oxide foams were prepared by means of a foam replica method using inexpensive polyurethane (PU) foams as the templates. Valuable insights into the preparation and utilization of cobalt oxide foams for TCS applications were provided. It was found that the solid loading of the cobalt oxide slurry could impact the structure of cobalt oxide foams by affecting the coating uniformity and thickness within the PU foams. Moreover, careful control of sintering conditions, including sintering temperature and sintering duration, was crucial in achieving the desired foam-like structure and stable redox repeatability performance for TCS applications. Relatively low sintering temperatures or short sintering durations could result in insufficient sintering, leading to a less compact and less interconnected structure. Conversely, excessively high sintering temperatures could cause over-sintering of cobalt oxide, resulting in a dense morphology with few voids that impede oxygen diffusion. Moreover, it was found that the cobalt oxide foams exhibited continuous structural evolutions during their reduction-oxidation cycles. The struts with a relatively large diameter within the PU foam appeared to be conducive to resisting foam distortion. In addition, a consecutive immersion approach was introduced for preparing the cobalt oxide foam. The result verifies that the re-immersion approach could repair cracks within the foam and increase the thermal storage density.

5.2 Future works

Based on the results have been obtained in this study, following works and suggestions should be done in the future.

(1) In the present study, Cu-doing and Li-doping have been verified as feasible approaches for extending the possibility of cobalt oxide-based TCS systems in relatively low working temperatures. However, we assumed the insertion of Cu

and Li into cobalt oxide have positive effects on the reduction/re-oxidation process, further investigation concerning the micro-mechanisms of Cu and Li species in the corresponding systems should be done.

(2) Sintering effect is a common issue in metal oxide-based TCS systems. Investigation concerning the careful control of the sintering process for other metal oxide-based redox systems is of interest.

(3) Cu-doing and Li-doping cobalt oxide composites with porous structures can be fabricated. And the parameters of these porous materials should be assessed by using them in a reactor.

Reference

[1] BP Statistical review of world energy, BP Global, June 2022.

[2] J. Bernodusson, Combustion of fossil fuels, Research and Development Icelandic Transport Authority, 2018.

[3] A. Gil, M. Medrano, I. Martorell, A. Lázaro, P. Dolado, B. Zalba, L.F. Cabeza, State of the art on high temperature thermal energy storage for power generation. Part 1- concepts, materials and modellization, Renewable and Sustainable Energy Reviews, 14, 2010, 31-55.

[4] S. Kuravi, J. Trahan, D. Yogi Goswami, M. M. Rahman, E. K. Stefanakos, Thermal energy storage technologies and systems for concentrating solar power plants, Progress in Energy and Combustion Science, 39, 2013, 285-319.

[5] C. Suresh, R.P. Saini, Review on solar thermal energy storage technologies and their geometrical configurations, International Journal of Energy Research, 44, 2020, 4163-4195.

[6] B. Koçak, A.I. Fernandez, H. Paksoy. Review on sensible thermal energy storage for industrial solar applications and sustainability aspects, Solar Energy, 209, 2020, 135-169.

[7] S. Danehkar, H. Yousefi. A comprehensive overview on water-based energy storage systems for solar applications, Energy Reports, 8, 2022, 8777-8797.

[8] K.I. Alghamdi, C.K. Bach, J.D. Spitler, Water-based thermal energy storage for heating and air-conditioning applications in residential buildings: review and preliminary study, 19th International Refrigeration and Air Conditioning Conference at Purdue, July 10-14, 2022.

[9] D. Beretta, F.C. Loveless, W. Nudenberg, Use of synthetic hydrocarbon oils as heat transfer fluids, United State Patent, No. 4239638, 1980.

[10] D.N. Nkwetta, M. Smyth, A. Zacharopoulos, T. Hyde, Experimental performance analysis and optimisation of medium temperature solar thermal collectors with silicon oil as a heat transfer fluid, International Journal of Energy Research, 37, 2013, 570-581.

[11] A. Mawire, Performance of sunflower oil as a sensible heat storage medium for domestic applications, Journal of Energy Storage, 5, 2016, 1-9.

[12] O.P. Abedigamba, F.S. Mndeme, A. Mawire, I. Bahadur, Thermo-physical properties and thermal energy storage performance of two vegetable oils, Journal of Energy Storage, 61, 2023, 106774.

[13] T. Bauer, C. Odenthal, A. Bonk, Molten salt storage for power generation, Chemie Ingenieur Technik, 93, 2021, 534-546.

[14] W. Ding, T. Bauer, Progress in research and development of molten chloride salt technology for next generation concentrated solar power plants, Engineering, 7, 2021, 334-347.

[15] A. Caraballo, S. Galán-Casado, Á. Caballero, S. Serena, Molten salts for sensible thermal energy storage: A review and an energy performance analysis, Energies, 14, 2021, 1197.

[16] T. Wang, D. Mantha, R.G. Reddy, Thermal stability of the eutectic composition in LiNO3-NaNO3-KNO3 ternary system used for thermal energy storage, Solar Energy Materials and Solar Cells, 100, 2012, 162-168.

[17] R.W. Bradshaw, D.E. Meeker, High-temperature stability of ternary nitrate molten salts for solar thermal energy systems, Solar Energy Materials, 21, 1990, 51-60.

[18] Y. Li, X. Xu, X. Wang, P. Li, Q. Hao, B. Xiao, Survey and evaluation of equations for thermophysical properties of binary/ternary eutectic salts for NaCl, KCl, $MgCl_2$, $CaCl_2$, $ZnCl_2$ for heat transfer and thermal storage fluids in CSP, Solar Energy, 152, 2017, 57-79.

[19] P.D. Myers, Jr., D. Yogi Goswami, Thermal energy storage using chloride salts and their eutectics, Applied Thermal Engineering, 109, 2016, 889-900.

[20] T. Bauer, N. Pfleger, N. Breidenbach, M. Eck, D. Laing, S. Kaesche, Materials aspects of solar salt for sensible heat storage, Applied Energy, 111, 2013, 1114-1119.

[21] H.E. Reilly, G.J. Kolb, An evaluation of molten-salt power towers including results of the solar two project, Sandia National Laboratories, November 2001.

[22] R. Tiskatine, R. Oaddi, R. Ait El Cadi, A. Bazgaou, L. Bouirden, A. Aharoune, A. Ihlal. Suitability and characteristics of rocks for sensible heat storage in CSP plants, Solar Energy Materials and Solar Cells, 169, 2017, 245-257.

[23] D. Laing, D. Lehmann, M. Fib, C. Bahl, Test results of concrete thermal energy

storage for parabolic trough power plants, Journal of Solar Energy Engineering, 131, 2009, 041007.

[24] Concrete storage for solar thermal power plants and industrial process heat, IRES iiii 2008, 3rd International Renewable Energy Storage Conference, Nov. 24-25, 2008.

[25] D. Raut, A.K. Tiwari, V.R. Kalamkar, A comprehensive review of latent heat energy storage for various applications: an alternate to store solar thermal energy, Journal of the Brazilian Society fo Mechanical Sciences and Engineering, 44, 2022, 446.

[26] K.S. Reddy, V. Mudgal, T.K. Mallick, Review of latent heat thermal energy storage for improved material stability and effective load management, Journal of Energy Storage, 15, 2018, 205-227.

[27] S.Y. Kee, Y. Munusamy, K.S. Ong, Review of solar water heaters incorporating solid-liquid organic phase change materials as thermal storage, Applied Thermal Engineering, 131, 2018, 455-471.

[28] J.R. Patil, P.A. Mahanwar, E. Sundaramoorthy, G.S. Mundhe, A review of the thermal storage of phase change material, morphology, synthesis methods, characterization, and applications of microencapsulated phase change material, Journal of Polymer Engineering, 43, 2023, 354-375.

[29] M.M. Farid, A.M. Khudhair, S.A.K. Razack, S. Al-Hallaj, A review on phase change energy storage: materials and applications, Energy Conversion and Management, 45, 2004, 1597-1615.

[30] R.K. Sharma, P. Ganesan, V.V. Tyagi, H.S.C. Metselaar, S.C. Sandaran, Developments in organic solid-liquid phase change materials and their applications in thermal energy storage, Energy Conversion and Management, 95, 2015, 193-228.

[31] S.S. Magendran, F.S.A. Khan, N.M. Mubarak, M. Vaka, R. Walvekar, M. Khalid, E.C. Abdullah, S. Nizamuddi, R.R. Karri, Synthesis of organic phase change materials (PCM) for energy storage applications: A review, Nano-Structures and Nano-Objects, 20, 2019, 100399.

[32] L. Wang, D. Meng, Fatty acid eutectic/polymethyl methacrylate composite as form-stable phase change material for thermal energy storage, Applied Energy,

87, 2010, 266-2665.

[33] M.A. Orozco, K. Acurio, F. Vásquez-Aza, J. Martínez-Gómez, A. Chico-Proano, Thermal storage of nitrate salts as phase change materials (PCMs), Materials, 14, 2021, 7223.

[34] Q. Wang, J. Wang, Y. Chen, C.Y. Zhao, Experimental investigation of barium hydroxide octahydrate as latent heat storage materials, Solar Energy, 177, 2019, 99-107.

[35] N. Pfleger, T. Bauer, C. Martin, M. Eck, A. Wörner, Thermal energy storage – overview and specific insight into nitrate salts for sensible and latent heat storage, Beilstein Journal of Nanotechnology, 6, 2015, 1487-1497.

[36] S.-C. Costa, K. Mahkamov, M. Kenisarin, M. Ismail, K. Lynn, E. Halimic, D. Mullen, Solar salt latent heat thermal storage for a small solar organic Rankine cycle plant, Journal of Energy Resources Technology, 142, 2020, 031203.

[37] B.C. Zhao, R.Z. Wang, Perspectives for short-term thermal energy storage using salt hydrates for building heat, Energy, 189, 2019, 116139.

[38] N. Kumar, J. Hirschey, T.J. LaClair, K.R. Gluesenkamp, S. Graham, Review of stability and thermal conductivity enhancements for salt hydrates, Journal of Energy Storage, 24, 2019, 100794.

[39] H. Ge, H. Li, S. Mer, J. Liu, Low melting point liquid metal as a new class of phase change material: An emerging frontier in energy area, Renewable and Sustainable Energy Reviews, 21, 2013, 331-346.

[40] L. Zhao, Y. Xing, X. Liu, Experimental investigation on the thermal management performance of heat sink using low melting point alloy as phase change material, Renewable Energy, 146, 2020, 1578-1587.

[41] N. Nallusamy, S. Sampath, R. Velraj, Experimental investigation on a combined sensible and latent heat storage system integrated with constant/varying (solar) heat sources, Renewable Energy, 32, 2007, 126-1227.

[42] M.K. Rathod, J. Banerjee, Thermal stability of phase change materials used in latent heat energy storage systems: A review, Renewable and Sustainable Energy Reviews, 18, 2013, 246-258.

[43] H. Jarimi, D. Aydin, Z. Yanan, G. Ozankaya, X. Chen, S. Riffat, Review on the recent progress of thermochemical materials and processes for solar thermal

energy storage and industrial waste heat recovery, International Journal of Low-Carbon Technologies, 14, 2019, 44-69.

[44] G.A. Farulla, M. Cellura, F. Guarino, M. Ferraro, A review of thermochemical energy storage systems for power grid support, Applied Sciences, 10, 2020, 3142.

[45] A.J. Carrillo, J. González-Aguilar, M. Romero, J.M. Coronado, Solar energy on demand: A review on high temperature thermochemical heat storage systems and materials, Chemical Reviews, 119, 2019, 4777-4816.

[46] W.E. Wentworth, E. Chen, Simple thermal decomposition reactions for storage of solar thermal energy, Solar Energy, 18, 1976, 205-214.

[47] H.U. Rammelberg, T. Schmidt, W. Ruck, Hydration and dehydration of salt hydrates and hydroxides for thermal energy storage – kinetics and energy release, Energy Procedia, 30, 2012, 362-369.

[48] L. Garofalo, F.V. Vitiello, F. Montagnaro, H. Bürgmayr, F. Winter, Salt hydrates for thermochemical storage of solar energy: Modeling the case study of calcium oxalate monohydrate dehydration/rehydration under suspension reactor conditions, Industrial and Engineering Chemistry Research, 60, 2021, 11357-11372.

[49] M. Molenda, J. Stengler, M. Linder, A. Wörner, Reversible hydration behavior of $CaCl_2$ at high H_2O partial pressures for thermochemical energy storage, Thermochimica Acta, 560, 2013, 76-81.

[50] R.-J. Clark, A. Mehrabadi, M. Farid, State of the art on salt hydrate thermochemical energy storage systems for use in building applications, Journal of Energy Storage, 27, 2020, 101145.

[51] A. Ichinose, K. Kuwata, T. Esaki, T. Matsuda, N. Kobayashi, Chemical heat storage using an SiC honeycomb packed with $CaCl_2$ powder, Journal of Materials Science and Chemical Engineering, 8, 2020, 23.

[52] A. Ichinose, N. Kobayashi, T. Esaki, Dehydration reaction and its acceleration for $CaCl_2$ hydration for chemical heat storage, American Journal of Engineering, Science and Technology, 5. 2020, 1.

[53] S. Li, H. Huang, X. Yang, Y. Bai, J. Li, N. Kobayashi, M. Kubota, Hydrophilic substance assisted low temperature $LiOH \cdot H_2O$ based composite thermochemical materials for thermal energy storage, Applied Thermal Engineering, 128, 2018,

706-711.

[54] S. Li, H. Huang, J. Li, N. Kobayashi, Y. Osaka, Z. He, H. Yuan, The effect of 3D carbon nanoadditives on lithium hydroxide monohydrate based composite materials for highly efficient low temperature thermochemical heat storage, RSC Advances, 8, 2018, 8199-8208.

[55] K. Wang, T. Yan, R.K. Li, W.G. Pan, A review for $Ca(OH)_2$/CaO thermochemical energy storage systems, Journal of Energy Storage, 50, 2022, 104612.

[56] S. Lin, Y. Wang, Y. Suzuki, High-temperature CaO hydration/$Ca(OH)_2$ decomposition over a multitude of cycles, Energy and Fuels, 23, 2009.

[57] Y. Kato, J. Nakahata, Y. Yoshizawa, Durability characteristics of the hydration of magnesium oxide under repetitive reaction, Journal of Materials Science, 34, 1999, 475-480.

[58] Y. Kato, N. Yamashita, K. Kobayashi, Y. Yoshizawa, Kinetic study of the hydration of magnesium oxide for a chemical heat pump, Applied Thermal Engineering, 16, 1996, 853-862.

[59] K. Kyaw, H. Matsuda, M. Hasatani, Applicability of carbonation/decarbonation reactions to high-temperature thermal energy storage and temperature upgrading, Journal of Chemical Engineering of Japan, 29, 1996, 119-125.

[60] G. Gravogl, C. Knoll, W. Artner, J.M. Welch, E. Eitenberger, G. Friedbacher, M. Harasek, K. Hradil, A. Werner, P. Weinberger, D. Müller, R. Miletich, Pressure effects on the carbonation of MeO (Me = Co, Mn, Pb, Zn) for thermochemical energy storage, Applied Energy, 252, 2019, 113451.

[61] W.G. Oakeson, I.B. Cutler, Effect of CO2 pressure on the reaction with CaO, Journal of the American Ceramic Society, 62, 1979, 545-644.

[62] S.Z. Ghorbaei, H.A. Ebrahim, Comparison of kinetics and thermochemical energy storage capacities of strontium oxide, calcium oxide, and magnesium oxide during carbonation reaction, Renewable Energy, 184, 2022, 765-775.

[63] D. Mahon, G. Claudio, P. Eames, An experimental study of the decomposition and carbonation of magnesium carbonate for medium temperature thermochemical energy storage, Energies, 14, 2021, 1316.

[64] C. Ortiz, J.M. Valverde, R. Chacartegui, L.A. Perez-Maqueda, P. Giménez, The calcium-looping ($CaCO_3$/CaO) process for thermochemical energy storage in

concentrating solar power plants, Renewable and Sustainable Energy Reviews, 113, 2019, 109252.

[65] A. Muto, K. McCabe, D. Real, High-temperature calcium-based thermochemical energy storage system for use with CSP facilities, AIP Conference Proceedings 2023, 2018.

[66] K. Kyaw, M. Kubota, F. Watanabe, H. Matsuda, M. Hasatani, Study of carbonation of CaO for high temperature thermal energy storage, Journal of Chemical Engineering of Japan, 31, 1998, 281-284.

[67] E. Bagherisereshki, J. Tran, F. Lei, N. AuYeung, Investigation into SrO/$SrCO_3$ for high temperature thermochemical energy storage, Solar Energy, 160, 2018, 85-93.

[68] N.R. Rhodes, A. Barde, K. Randhir, L. Li, D.W. Hahn, R. Mei, J.F. Klausner, N. AuYeung, Solar thermochemical energy storage through carbonation cycles of $SrCO_3$/SrO supported on $SrZrO_3$, ChemSusChem, 8, 2015, 3793-3798.

[69] N. Amghar, C. Ortiz, A. Perejón, J.M. Valverde, L.P. Maqueda, P.E. Sánchez Jiménez, The $SrCO_3$/SrO system for thermochemical energy storage at ultra-high temperature, Solar Energy Materials and Solar Cells, 238, 2022, 111632.

[70] D.G. Ivey, R.I. Chittim, K.J. Chittim, D.O. Northwood, Metal hydrides for energy storage, Journal of Materials for Energy Systems, 3, 1981, 3-19.

[71] M. Felderhoff, B. Bogdanović, High temperature metal hydrides as heat storage materials for solar and related applications, International Journal of Molecular Sciences, 10, 2009, 325-344.

[72] O. Bernauer, C. Halene, Properties of metal hydrides for use in industrial applications, Journal of the Less-Common Metals, 131, 1987, 213-224.

[73] X. Qu, Y. Li, P. Li, Q. Wan, F. Zhai, The development of metal hydrides using as concentrating solar thermal storage materials, Frontiers of Materials Science, 9, 2015, 317-331.

[74] C. Corgnale, B. Hardy, T. Motyka, R. Zidan, J. Teprovich, B. Peters, Screening analysis of metal hydride based thermal energy storage systems for concentrating solar power plants, Renewable and Sustainable Energy Reviews, 38, 2014, 821-833.

[75] S. Tescari, C. Agrafiotis, S. Breuer, L. de Oliveira, M. Neises-von Puttkamer, M.

Roeb, C. Sattler, Thermochemical solar energy storage via redox oxides: materials and reactor/heat exchanger concepts, Energy Procedia, 49, 2014, 1034-1043.

[76] B. Wong, Thermochemical heat storage for concentrated solar power, Final Report for the U.S. Department of Energy, United States, 2011, pp. 10-31.

[77] A.J. Carrillo, D. Sastre, D.P. Serrano, P. Pizarro, J.M. Coronado, Revisiting the BaO_2/BaO redox cycle for solar thermochemical energy storage, Physical Chemistry Chemical Physics, 18, 2016, 8039-8048.

[78] F. Lei, A. Dyall, N. AuYeung, An in-depth investigation of BaO_2/BaO redox oxides for reversible solar thermochemical energy storage, Solar Energy Materials and Solar Cells, 223, 2021, 110957.

[79] A.J. Carrillo, D.P. Serrano, P. Pizarro, J.M. Coronado, Thermochemical heat storage based on the Mn_2O_3/Mn_3O_4 redox couple: influence of the initial particle size on the morphological evolution and cyclability, Journal of Materials Chemistry A, 2, 2014, 19435-19443.

[80] C. Agrafiotis, M. Roeb, M. Schmucker, C. Sattler, Exploitation of thermochemical cycles based on solid oxide redox systems for thermochemical storage of solar heat. Part 1: Testing of cobalt oxide-based powders, Solar Energy, 102, 2014, 189-211.

[81] E. Alonso, C. Perez-Pabago, J. Licurgo, E. Fuentealba, C.A. Estrada, First experimental studies of solar redox reactions of copper oxides for the thermochemical energy storage, Solar Energy, 115, 2015, 297-305.

[82] K.J. Albrecht, G.S. Jackson, R.J. Braun, Thermodynamically consistent modeling of redox-stable perovskite oxides for thermochemical energy conversion and storage, Applied Energy, 165, 2016, 285-296.

[83] Z. Zhang, L. Andre, S. Abanades, Experimental assessment of oxygen exchange capacity and thermochemical redox cycle behavior of Ba and Sr series perovskites for solar energy storage, Solar Energy, 134, 2016, 494-502.

[84] N. Gokon, T. Yawata, S. Bellan, T. Kodama, H.S. Cho, Thermochemical behavior of perovskite oxides based on $La_xSr_{1-x}(Mn, Fe, Co)O_{3-\delta}$ and $Ba_ySr_{1-y}CoO_{3-\delta}$ redox system for thermochemical energy storage at high temperature, Energy, 171, 2019, 971-980.

[85] A.J. Carrillo, D.P. Serrano, P. Pizarro, J.M. Coronado, Understanding redox

kinetics of iron-doped manganese oxides for high temperature thermochemical energy storage, Journal of Physical Chemistry, 120, 2016, 27800-27812.

[86] F. Varsano, C. Alvani, A.L. Barbera, A. Masi, F. Padella, Lithium manganese oxides as high-temperature thermal energy storage system, Thermochimica Acta, 640, 2016, 26-35.

[87] N.W. Hlongwa, D. Sastre, E. Iwuoha, A.J. Carrillo, C. Ikpo, D.P. Serrano, P. Pizarro, J.M. Coronado, Exploring the thermochemical heat storage capacity of AMn_2O_4 (A = Li or Cu) Spinels, Solid State Ionics, 320, 2018, 316-324.

[88] P.O. Carden, Energy corradiation using the reversible ammonia reaction, Solar Energy, 19, 1977, 365-378.

[89] K. Lovegrove, Thermodynamic limits on the performance of a solar thermochemical energy storage system, International Journal of Energy Research, 17, 1993, 817-829.

[90] P. Pardo, A. Deydier, Z. Anxionnaz-Minvielle, S. Rougé, M. Cabassud, P. Cognet, A review on high temperature thermochemical heat energy storage, Renewable and Sustainable Energy Reviews, 32, 2014, 591-610.

[91] X. Peng, T.W. Root, C.T. Maravelias, Storing solar energy with chemistry: the role of thermochemical storage in concentrating solar power, Green Chemistry, 19, 2017, 2427-2438.

[92] M. Neises, S. Tescari, L. de Oliveira, M. Roeb, C. Sattler, B. Wong, Solar-heated rotary kiln for thermochemical energy storage, Solar Energy, 86, 2012, 3040-3048.

[93] M. Wokon, A. Kohzer, M. Linder, Investigations on thermochemical energy storage based on technical grade manganese-iron oxide in a lab-scale packed bed reactor, Solar Energy, 153, 2017, 200-214.

[94] S. Tescari, A. Singh, C. Agrafiotis, L. de Oliveira, S. Breuer, B. Schlögl-Knothe, M. Roeb, C. Sattler, Experimental evaluation of a pilot-scale thermochemical storage system for a concentrated solar power plant, Applied Energy, 189, 2017, 66-75.

[95] S. Álvarez de Miguel, J. Gonzalez-Aguilar, M. Romero, 100-Wh multi-purpose particle reactor for thermochemical heat storage in concentrating solar power plants, Energy Procedia, 49, 2014, 676-683.

[96] K.N. Hutchings, M. Wilson, P.A. Larsen, R.A. Cutler, Kinetic and

thermodynamic considerations for oxygen absorption/desorption using cobalt oxide, Solid State Ionics, 177, 2006, 45-51.

[97] 未利用熱エネルギー革新的活用技術研究組合, 産業分野の排熱実態調査, 2019. Available online: http://www.thermat.jp/HainetsuChousa/HainetsuReport.pdf

[98] T. Block, N. Knoblauch, M. Schmucker, The cobalt-oxide/iron-oxide binary system for use as high temperature thermochemical energy storage materials, Thermochimica Acta, 577, 2014, 25-32.

[99] A.J. Carrillo, J. Moya, A. Bayon, P. Jana, V.A. de la Pena O'Shea, M. Romero, J. Gonzalez-Aguilar, D.P. Serrano, P. Pizarro, J.M. Coronado, Thermochemical energy storage at high temperature via redox cycles of Mn and Co oxides: Pure oxides versus mixed ones, Solar Energy Materials and Solar Cells, 123, 2014, 47-57.

[100] T. Block, M. Schmucker, Metal oxides for thermochemical energy storage: A comparison of several metal oxide systems, Solar Energy, 126, 2016, 195-207.

[101] L. Andre, S. Abanades, L. Cassayre, High-temperature thermochemical energy storage based on redox reactions using Co-Fe and Mn-Fe mixed metal oxides, Journal of Solid State Chemistry, 253, 2017, 6-14.

[102] Y. Portilla-Nieto, A. Zaki, K. Vidal, M. Hernaiz, E. Aranzabe, S. Doppiu, A. Faik, Development of $Co_{3-x}Ni_xO_4$ materials for thermochemical energy storage at lower red-ox temperature, Solar Energy Materials and Solar Cells, 230, 2021, 111194.

[103] J.A. Moulijn, A.E. van Diepen, F. Kapteijn, Catalyst deactivation: is it predictable? What to do?, Applied Catalysis A: General, 212, 2001, 3–16.

[104] D. Bielsa, M. Oregui, P.L. Arias, New insights into Mn_2O_3 based metal oxide granulation technique with enhanced chemical and mechanical stability for thermochemical energy storage in packed bed reactors. Solar Energy, 241, 2022, 248-261.

[105] C. Agrafiotis, M. Roeb, M. Schmucker, C. Sattler, Exploitation of thermochemical cycles based on solid oxide redox systems for thermochemical storage of solar heat. Part 2: Redox oxide-coated porous ceramic structures as integrated thermochemical reactors/heat exchangers, Solar Energy, 114, 2015,

440-458.

[106] C. Agrafiotis, S. Tescari, M. Roeb, M. Schmucker, C. Sattler, Exploitation of thermochemical cycles based on solid oxide redox systems for thermochemical storage of solar heat. Part 3: Cobalt oxide monolithic porous structures as integrated thermochemical reactors/heat exchangers, Solar Energy, 114, 2015, 459-475.

[107] D. Lin, K.W. Kwok, H.L.W. Chan, Microstructure, dielectric and piezoelectric properties of $(K_{0.5}Na_{0.5})NbO_3$-$Ba(Ti_{0.95}Zr_{0.05})O_3$ lead-free ceramics with CuO sintering aid, Applied Physics A, 88, 2007, 359-363.

[108] E.M. Alkoy, M. Papila, Microstructural features and electrical properties of copper oxide added potassium sodium niobite ceramic, Ceramics International, 36, 2010, 1921-1927.

[109] W. Stichert, F. Schüth, Influence of crystallite size on the properties of zirconia, Chemistry of Materials, 10, 1998, 2020-2026.

[110] K. Phiwdang, S. Suphankij, W. Mekprasart, W. Pecharapa, Synthesis of CuO nanoparticles by precipitation method using different precursors, Energy Procedia, 34, 2013, 740-745.

[111] X. Shi, H. Zheng, A.M. Kannan, K. Pérez-Salcedo, B. Escobar, Effect of thermally induced oxygen vacancy of α-MnO_2 nanorods toward oxygen reduction reaction, Inorganic Chemistry, 58, 2019, 5335-5344.

[112] G. Zhuang, Y. Chen, Z. Zhuang, Y. Yu, J. Yu, Oxygen vacancies in metal oxides: recent progress towards advanced catalyst design, Science China Materials, 63, 2020, 2089-2118.

[113] M.W. Hussain, M.Y.H. Ansari, Significance and importance of thermal expansion, IOSR Journal of Applied Physics, 9, 2017, 68-73.

[114] F.C.M. Driessens, G.D. Rieck, H.N. Coenen, Phase equilibria in the system cobalt oxide/copper oxide in air, Journal of Inorganic and Nuclear Chemistry, 1968, 30, 747-753.

[115] Z.Z. Fang, H. Wang, V. Kumar, Coarsening, densification, and grain growth during sintering of nano-sized powders – A perspective, Int. Journal of Refractory Metals and Hard Materials, 62, 2017, 110-117.

[116] X. Wang, A. Atkinson, Combining densification and coarsening in a Cellular

Automata-Monte-Carlo simulation of sintering: Methodology and calibration, Computational Materials Science, 143, 2018, 338-349.

[117] R.M. German, Coarsening in sintering: grain shape distribution, grain size distribution, and grain growth kinetics in solid-pore systems, Critical Reviews in Solid State and Materials Sciences, 35, 2010, 263-305.

[118] P.E. Marín, Y. Milian, S. Ushak, L.F. Cabeza, M. Grágeda, G.S.F. Shire, Lithium compounds for thermochemical energy storage: A state-of-the-art review and future trends, Renewable and Sustainable Energy Reviews, 149, 2021, 111381.

[119] J. Yan, C.Y. Zhao, First-principle study of $CaO/Ca(OH)_2$ thermochemical energy storage system by Li or Mg cation doping, Chemical Engineering Science, 117, 2014, 293-300.

[120] J. Ryu, N. Hirao, R. Takahashi, Y. Kato, Dehydration behavior of metal-salt-added magnesium hydroxide as chemical heat storage media, Chemistry Letters, 37, 2008, 1140.

[121] H. Ishitobi, N. Hirao, J. Ryu, Y. Kato, Evaluation of heat output densities of lithium chloride-modified magnesium hydroxide for thermochemical energy storage, Industrial & Engineering Chemistry Research, 52, 2013, 5321-5325.

[122] O. Myagmarjav, J. Ryu, Y. Kato, Lithium bromide-mediated reaction performance enhancement of a chemical heat-storage material for magnesium oxide/water chemical heat pumps, Applied Thermal Engineering, 63, 2014, 170-176.

[123] A. Shkatulov, Y. Aristov, Modification of magnesium and calcium hydroxides with salts: An efficient way to advanced materials for storage of middle-temperature heat, Energy, 85, 2015, 667-676.

[124] A.I. Shkatulov, Y. Aristov, Thermochemical energy storage using $LiNO_3$-doped $Mg(OH)_2$: A dehydration study, Energy Technology, 6, 2018, 1844-1851.

[125] A. Shkatulov, H. Takasu, Y. Kato, Y. Aristov, Thermochemical energy storage by $LiNO_3$-doped $Mg(OH)_2$: Rehydration study, Journal of Energy Storage, 22, 2019, 302-310.

[126] S. Li, J. Liu, T. Tan, J. Nie, H. Zhang, Optimization of $LiNO_3$-$Mg(OH)_2$ composites as thermo-chemical energy storage materials, Journal of Environmental Management, 262, 2020, 110258.

[127] A. Maruyama, R. Kurosawa, J. Ryu, Effect of lithium compound addition on the dehydration and hydration of calcium hydroxide as a chemical heat storage material, ACS Omega, 5, 2020, 9820-9829.

[128] A.I. Shkatulov, S.T. Kim, H. Miura, Y. Kato, Y.I. Aristov, Adapting the MgO-CO_2 working pair for thermochemical energy storage by doping with salts, Energy Conversion and Management, 185, 2019, 473-481.

[129] T. Ohzuku, A. Ueda, Solid-state redox reactions of $LiCoO_2$ (R3m) for 4 volt secondary lithium cells, Journal of The Electrochemical Society, 141, 1994, 2972.

[130] H. Wang, S. Xu, C. Tsai, Y. Li, C. Liu, J. Zhao, Y. Liu, H. Yuan, F. Abild-Pedersen, F.B. Prinz, J.K. Nørskov, Y. Cui Y, Direct and continuous strain control of catalysts with tunable battery electrode materials, Science, 354, 2016, 1031-1036.

[131] S. Vyazovkin, A.K. Burnham, J.M. Criado, L.A. Perez-Maqueda, ICTAC kinetics committee recommendations for performing kinetic computations on thermal analysis data, Thermochimica Acta, 520, 2011, 1-19.

[132] H.L. Friedman, Kinetics of thermal degradation of char-forming plastics from thermogravimetry. Application to a phenolic plastic, Journal of Polymer Science: Part C, 6, 1964, 183-195.

[133] X. Xie, Y. Li, Z.Q. Liu, M. Haruta, W. Shen, Low-temperature oxidation of CO catalysed by Co3O4 nanorods, Nature, 458, 2009, 746.

[134] Y. Zhang, F. Ding, C. Deng, S. Zhen, X. Li, Y. Xue, Y.M. Yan, K. Sun, Crystal plane-dependent electrocatalytic activity of Co_3O_4 toward oxygen evolution reaction, Catalysis Communications, 67, 2015, 78-82.

[135] M. Gigantino, S.S. Brunser, A. Steinfeld, High-temperature thermochemical heat storage via the CuO/Cu_2O redox cycle: From material synthesis to packed-bed reactor engineering and cyclic operation, Energy and Fuels, 34, 2020, 16772-16782.

[136] N.C. Preisner, M. Linder, A moving bed reactor for thermochemical energy storage based on metal oxides, Energies, 13, 2020, 1232.

[137] J. Yu, C. Li, F. Guo, S. Gao, Z. Zhang, K. Matsuoka, G. Xu, The pilot demonstration of a honeycomb catalyst for the $DeNO_x$ of low-temperature flue gas from an industrial coking plant, Fuel, 219, 2018, 37-49.

[138] P. Furler, J. Scheffe, D. Marxer, M. Gorbar, A. Bonk, U. Vogt, A. Steinfeld, Thermochemical CO_2 splitting via redox cycling of ceria reticulated foam structures with dual-scale porosities, Physical Chemistry Chemical Physics, 16, 2014, 10503-10511.

[139] C. Pagkoura, G. Karagiannakis, E. Halevas, A.G. Konstandopoulos, Co_3O_4-based honeycombs as compact redox reactors/heat exchangers for thermochemical storage in the next generation CSP plants, AIP Conference Proceedings, 1734, 2016, 050037.

[140] A.R. Studart, U.T. Gonzenbach, E. Tervoort, L.J. Gauckler, Processing routes to macroporous ceramics: A review, Journal of the American Ceramic Society, 89, 2006, 1771-1789.

[141] Information of Data: https://cica-web.kanto.co.jp/CicaWeb/msds/E_07411.pdf

[142] N. Mangesana, R.S. Chikuku, A.N. Mainza, I. Govender, A.P. van der Westhuizen, M. Narashima, The effect of particle sizes and solids concentration on the rheology of silica sand based suspensions, The Journal of The Southern African Institute of Mining and Metallurgy, 108, 2008, 237.

[143] B. Dorri, V. Kadambi, F.W. Staub, Thermal stress analysis of sintering using a moving grid, International Journal for Numerical Methods in Engineering, 24, 1987, 47-57.

[144] X. Zhu, D. Jiang, S. Tan, Z. Zhang, Improvement in the strut thickness of reticulated porous ceramics, Journal of the American Ceramic Society, 84, 2001, 1654-1656.

Acknowledgement

To begin, I would like to express my sincere gratitude to Assoc. Prof. Noriyuki Kobayashi, my supervisor, for his valuable time, patience, and understanding in supporting me in my studies. I am deeply grateful to him for providing me with the opportunity to pursue my doctoral studies and introducing me to the field of energy storage. He provides me with ample trust and space to explore and grow in my studies. His attitude and perspectives towards scientific research have deeply influenced me as well.

I am also immensely grateful to Prof. Katsutoshi Nagaoka, Graduate School of Engineering Department of Chemical Systems Engineering in Nagoya University, Prof. Makoto Kobashi, Graduate School of Engineering Department of Materials Process Engineering in Nagoya University, Assoc. Prof. Ryo Yoshiie, Graduate School of Engineering Department of Mechanical Systems Engineering in Nagoya University for their constructive criticism and expertise in reviewing this thesis.

I would like to express my deepest gratitude to Prof. Hongyu Huang, Guangzhou Institute of Energy Conversion, Chinese Academy of Sciences in China, for his encouragement and support throughout this journey. And I am truly grateful to Asst. Prof. Mitsuhiro Kubota for generously giving his time and providing the necessary resources for my research.

Furthermore, I appreciate my colleagues and co-researches for their generous help and cooperation. Among them, I would like to name Atsuhiro Ichinose, Yasuhiro Aiba, Bohan Jia, Natsuki Chihara, Atsuki Ogawa in Kobayashi Laboratory, and Lisheng Deng, Lin Liu in Guangzhou Institute of Energy Conversion, Chinese Academy of Sciences.

Lastly, I would like to express my gratitude to my family and my friends for their unwavering support, love, and encouragement. Their belief in me has been a constant source of motivation and inspiration.

List of publications

	Title	Publication method and time	Authors
	I. Published papers		
1	Exploration of $LiCoO_2$-doped cobalt oxide composite for thermochemical energy storage at high temperature	Journal of Energy Storage, Vol. 55, 105774 (2022)	Rongjun Wu, Lisheng Deng, Hongyu Huang, Mitsuhiro Kubota, Noriyuki Kobayashi
2	Experimental and theoretical study on water vapor isothermal adsorption-desorption characteristics of desiccant coated adsorber	International Journal of Heat and Mass Transfer, Vol. 187, 122529 (2022)	Lin Liu, Rongjun Wu, Jun Li, Mitsuhiro Kubota, Yu Bai, Hongyu Huang, Noriyuki Kobayashi
3	Influence of CuO doping on cobalt oxide for thermochemical energy storage	Solar Energy Materials and Solar Cells, Vol. 253, 112211 (2023)	Rongjun Wu, Hongyu Huang, Lisheng Deng, Mitsuhiro Kubota, Noriyuki Kobayashi
	II. Conference presentations		
1	Redox Behaviors of $Ce_{(1-x)}Mn_xO_2$ Solid-Solution for Thermochemical Heat Storage	SCEJ 52nd Autumn Meeting, September, 22nd-24th, Okayama, Japan (2021)	Rongjun Wu, Noriyuki Kobayashi, Mitsuhiro Kubota
2	Effects of CuO Doping on Cobalt Oxide for Thermochemical Heat Storage	SCEJ 53rd Autumn Meeting, September, 14th-16th, Nagano, Japan (2022)	Rongjun Wu, Noriyuki Kobayashi, Mitsuhiro Kubota